PSFC/RR-97-5 DOE/ET-51013-323

Reflectometry Measurements on Alcator C-Mod

Paul C. Stek

March 1997

This work was supported by the U. S. Department of Energy Contract No. DE-AC02-78ET51013. Reproduction, translation, publication, use and disposal, in whole or in part by or for the United States government is permitted.

Reflectometry Measurements on Alcator C-Mod

by

Paul Cornelis Stek

Submitted to the Department of Physics
in partial fulfillment of the requirements for the degree of

Doctor of Philosophy

at the

MASSACHUSETTS INSTITUTE OF TECHNOLOGY

March 1997

Author .....
Department of Physics
March 11, 1997

Certified by .....
Dr. Jim Irby
Research Scientist, Experimental and Group Leader
Thesis Supervisor

Certified by .....
Professor Miklos Porkolab
Director of the Plasma Science & Fusion Center
Thesis Supervisor

Accepted by .....
Professor George Koster
Chairman, Physics Department Committee on Graduate Students

Reflectometry Measurements on Alcator C-Mod

by

Paul Cornelis Stek

Submitted to the Department of Physics
on March 11, 1997, in partial fulfillment of the
requirements for the degree of
Doctor of Philosophy

Abstract

This thesis presents the development of a novel millimeter wave reflectometer for the study of electron density profile evolution in the Alcator C-Mod tokamak.

The rate at which energy is transported from the center to the edge of a tokamak plasma is one of the main issues dictating the size and cost of future fusion reactors. A factor of two improvement in energy confinement time over basic operation or L-mode can be attained by operating in high or H-mode. The H-mode is characterized by a transport barrier at the plasma edge.

To study the density profile and its evolution during H-mode a novel 5 channel millimeter wave reflectometer was developed. With this diagnostic, electron density gradients of $2 \times 10^{20}\mathrm{m}^{-4}$ have been observed during ELM-free plasmas within 0.5 ms of the transition from L to H-mode. The width of the transport barrier was measured to be less than 2 cm during the initial H-mode period.

Thesis Supervisor: Dr. Jim Irby
Title: Research Scientist, Experimental and Group Leader

Thesis Supervisor: Professor Miklos Porkolab
Title: Director of the Plasma Science & Fusion Center

Acknowledgments

I am certain to omit many people here, and I apologize to those that I do omit.

I want to start by thanking my advisor, Dr. Jim Irby, for his support over the years and for his willingness to give me the freedom to make my own mistakes along the way. I would also like to thank Professors Miklos Porkolab and Ian Hutchinson for their teaching and efforts as readers of this thesis. The quality of this document has benefitted greatly from their efforts.

Thanks to all of the Alcatorians. There is hardly a student or member of the engineering, technical, scientific, or support staff that has not taught me something along the way. I will miss the free flow of ideas that characterize this group. A special thanks to all of those who had to endure a conversation beginning with "Can I ask you a dumb question...".

To all my friends on the MIT Cycling Team: John"Voice of Reason" and Kjirste "PowerBat" Morrell, Tom "the Sniveler" Moyer, "Smelly" Rich Pawlowicz,
Jim "Tango" Preisig, "Joe Bob" Armstrong, Karon "Ronbo" MacLean, " nickname-less" Jill Shirwood, and everyone else, I'll never forget the fun we had racing together nor the joy of beating UMess at Easterns. Go MITTT!

Thanks to my mother, father and, sisters who encouraged me through this expe-rience.

And thanks to Molly to have put up with me all these years. I don't know how I will ever repay you, but I'll try.

Contacts

The author welcomes any questions regarding this research. I can be contacted at:

Jet Propulsion Laboratory
Microwave Lidar, and Interferometer Technology Section
Observational Systems Division
4800 Oak Grove Drive
M/S 168-214
Pasadena, CA 91109-8099
1-818-354-7749
My E-mail address is currently unknown but will be available via the finger utility using "paul.stek@jpl.nasa.gov".

The C-Mod reflectometer is left in the very capable hands of Yijun Lin (ylin@pfc.mit.edu) under the guidance of Jim Irby (irby@pfc.mit.edu).
Earl Marmar (Marmar@pfc.mit.edu) is head of Alcator diagnostics.
Ian Hutchinson (hutch@pfc.mit.edu) is head of the Alcator research group.
The general number for the PFC is (617) 253-8100.

Typesetting and Figures

This thesis was written using Latex version 2e by blindly following the path laid out by Dr. Darren Garnier Ph.D. M.o.L.[a]. Data figures were generated using IDL Version 4 or MDS+. Hardware figures were generated with Claris-Cad and Auto-Cad.

[a]Master of Latex

Contents

List of Figures

List of Tables

Chapter 1

Thesis Outline and Goals

1.1 Plasma Transport

One of the key issues in the development of plasma fusion as an energy source is learning how to predict and control the transport of particles and energy within the plasma. Energy transport in a plasma is much faster than the diffusion predicted by random collisions between plasma constituents. Collective effects driven, presumably, by density and temperature gradients speed the transport of energy from the center to the edge of the plasma. This has had a disastrous effect on the development of commercial reactors as the faster energy is transported, the larger and more expensive a reactor must become.

Kaye and Goldston [1] identified a baseline level of confinement named the Low Mode or L-mode that virtually all tokamaks conform to provided no special efforts are made. Several enhanced confinement modes of operation have also been observed (see review by Stambaugh et. al. [2]). In all such modes the turbulence that presumably drives transport is suppressed in some portion of the plasma. The most common of these enhanced confinement modes is the High Mode or H-mode first observed on the ASDEX tokamak [3]. In this mode of operation, very large gradients in temperature and density are observed at the outer edge of the plasma, indicating some form of a transport barrier has formed there. Energy confinement in H-mode is two to four times that during L-mode. Most reactor proposals plan on taking advantage of this

confinement enhancement.

1.2 Alcator C-Mod

Alcator C-Mod is a shaped and diverted follow-on to the very successful Alcator A and C tokamaks. It is a compact tokamak capable of operating at nine tesla, 1.5 mega-amps of plasma current. With a main plasma volume of one cubic meter and a combined ohmic and ICRF heating power of five megawatts, C-Mod has a power density and divertor heat flux comparable to that expected on future reactors. As one of only two large tokamaks commissioned in the last decade, C-Mod is a testing ground for many new concepts in plasma science, particularly divertor operation and high power density ICRF heating. With its high field and high current and power density, C-Mod is well positioned to study plasma confinement in regimes complimentary to those studied elsewhere.

1.3 Plasma Diagnosis

In order to study transport phenomena, accurate measurements of the local temperature and density of electrons and ions and their gradients are needed. Despite extensive effort devoted to plasma diagnosis, the electron temperature, via electron cyclotron emission, is the only quantity that is routinely measured with high precision and localization.

1.3.1 Reflectometry

Reflectometry is a diagnostic particularly well suited for studying the electron density profile and fluctuations during H-modes. Based on the same concept as ionospheric sounding, reflectometry involves launching microwaves into the plasma and measuring the propagation time to some reflecting layer. For the polarization and frequencies

used in the C-Mod reflectometer, the index of refraction is given by:

$$N^2 = \frac{c^2k^2}{\omega^2} = 1 - \left(\frac{\omega_{pe}}{\omega^2}\right)^2 \qquad \text{where,} \quad \omega_{pe}^2 = \frac{n_e e^2}{\epsilon_0 m_e} \tag{1.1}$$

where ω_{pe} is the electron plasma frequency. Figure 1-1 shows the basic concept of reflectometry. A given frequency, f, is launched from the right towards the plasma. At the position $R_c(f)$ where $n = n_c(f)$ the wave is reflected. By using multiple frequencies and measuring the time a pulse takes to propagate to the reflecting layer and back, the density profile can be determined [a]. A new diagnostic technique called differential phase or amplitude modulated reflectometry is employed in this thesis. This technique involves upconverting a fixed frequency and launching both sidebands. The phase difference between the two returned signals gives the group delay with very high time response. Figure 1-2 shows an example of the data obtained from the reflectometer before and after an L-mode to H-mode transition.

1.4 Thesis Goals

The first goal of this thesis is the development of a diagnostic to measure the electron density profile in the plasma edge in C-Mod. A five channel microwave reflectometer with an innovative modulation scheme was developed for this. The second goal is to study the time evolution of H-mode profiles in C-Mod. And, the third goal is to distinguish between the varieties of H-modes seen on C-Mod.

1.5 Thesis Outline

The approach to studying Alcator C-Mod plasmas using reflectometry is outlined below.

- Chapter two will introduce some of the basic concepts in tokamak physics including energy and particle confinement.

[a] Dispersion is a major factor here and will be discussed in Chapter 4.

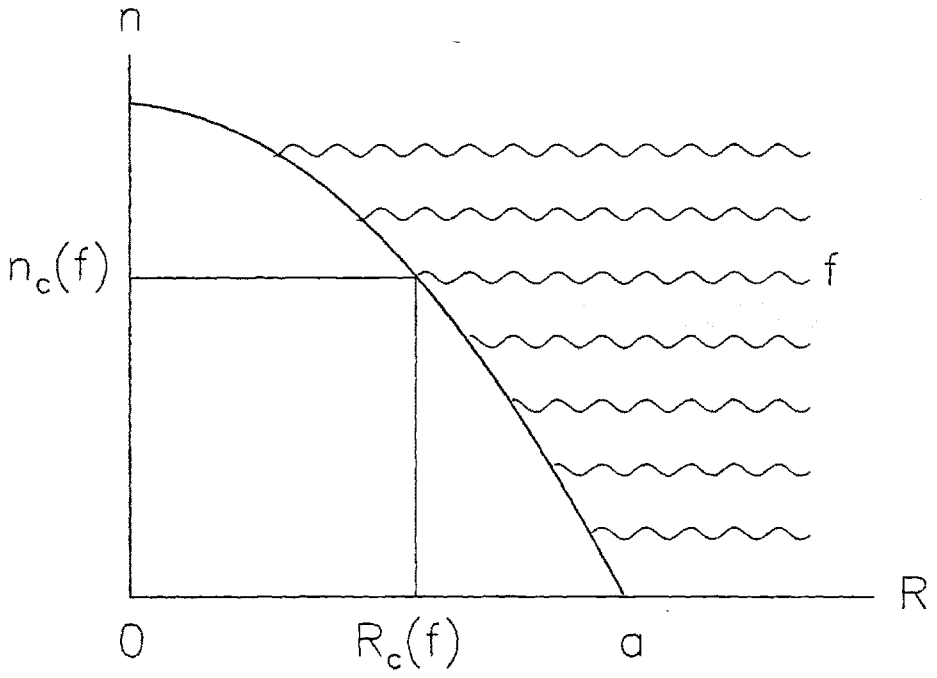

Figure 1-1: Reflectometry Concept Multiple frequencies are launched from the right, and the group delay to the cutoff layer and back is monitored.

- Chapter three will cover the Alcator C-Mod tokamak, some of the diagnostic tools available, and the main research goals of C-Mod.
- Chapter four introduces the basic theories behind reflectometry.
- Chapter five presents the reflectometer diagnostic developed for C-Mod including an innovative modulation scheme.
- Profile inversion, calibration, and comparison with other diagnostics is presented in chapter six.
- Chapter seven discusses the electron density profile evolution during H-modes in C-Mod. Fluctuations and ELM's during the various types of H-modes seen on C-Mod will also be presented.
- In Chapter eight, conclusions and recommendations for future work are presented.

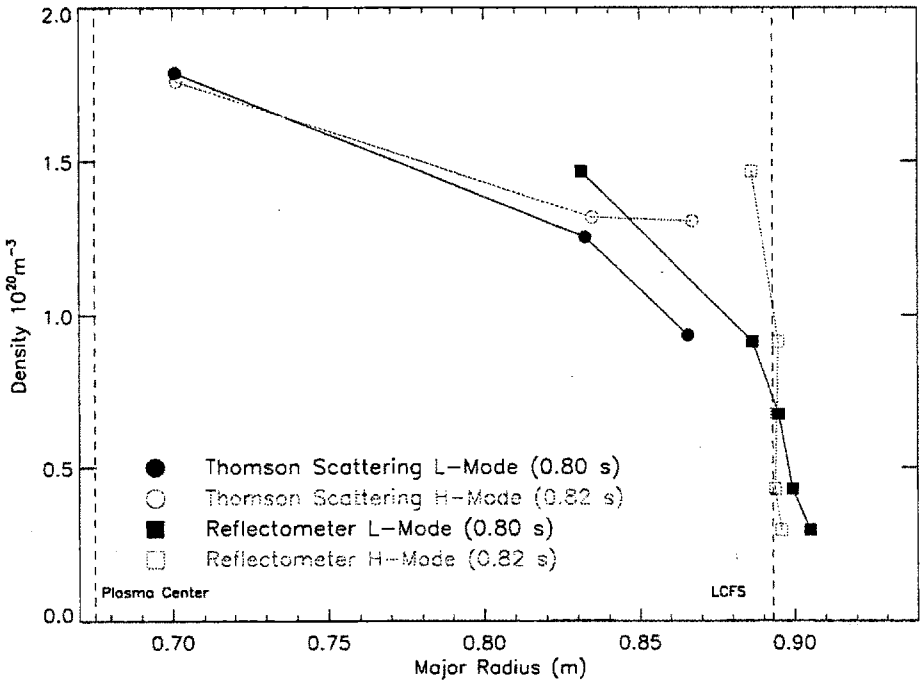

Figure 1-2: Example H-mode Profile Shot 950602028. During an H-mode, the profile steepens greatly near the last closed flux surface (LCFS). The high gradient can form in less than 1 ms. (The absolute calibration of the Thomson scattering is suspect for reasons to be discussed.)

- In Appendix A the group delay measured for a linear profile is presented along with a matrix technique for inverting a piecewise linear profile.
- Appendix B is a table of some of the many acronyms used in this thesis with references to the first usage.

Chapter 2

Plasmas and Plasma Fusion

In this chapter, plasmas, plasma fusion, and tokamaks will be presented. The intention is that a reader with little prior knowledge of fusion[a] will understand the motivation for the research presented in later chapters. A more detailed introduction to plasma physics can be found in Chen [4]. Wesson [5] is an excellent, though quite expensive, reference on tokamaks.

2.1 Plasma

A plasma is gas in which at least a fraction of the atoms present are ionized. They are typically characterized by high electrical conductivity. Some common plasmas are welding arcs, lightning, and the discharges in fluorescent light bulbs. While in these plasmas only a small fraction of the constituent gas is ionized, their conductivity is dominated by this small ionized fraction. Plasma is often referred to as the fourth state of matter[b], and in fact only 0.5 percent of the known universe is in the first three states: gas, liquid, and solid. Most of the rest is plasma.

Despite the cosmological disposition of matter to be ionized, plasmas are relatively

[a]Like the wife of the author who is proofreading this.

[b]It should be noted that the other three states, under most conditions, will have a well defined phase transition and phase boundary. There is no such boundary or transition between a gas and a plasma. The naming of an object as either a gas or a plasma in many cases reflects more on the analysis being performed. In addition, designating plasmas the fourth state of matter opens the door to a host of other conditions that could lay claim to being a state of matter such a neutron star or a black hole.

remote from the average human's existence.[c] And while fluorescent lights and arc welders are useful appliances, their understanding hardly warrants the $ 1 billion annual worldwide budget for plasma research. In fact, most of the study of plasmas, the subject of this thesis included, is directed towards the development of nuclear fusion as a "cleaner" energy source for the future.

2.2 Fusion

Nuclear fusion is the combining of two nuclei to form a larger nucleus and usually a free neutron or proton. The source of the energy given off by most stars is the fusing of hydrogen into helium[d] (a fact only recognized early this century). While there is a very long list of possible fusion reactions, the most promising ones for terrestial power production are[e]:

$$D^2 + T^3 \rightarrow He^4 + n^1 + 17.6MeV \tag{2.1}$$

$$D^2 + D^2 \rightarrow He^3 + n^1 + 3.27MeV \tag{2.2}$$

$$D^2 + D^2 \rightarrow T^3 + H^1 + 4.03MeV \tag{2.3}$$

$$D^2 + He^3 \rightarrow He^4 + H^1 + 18.3MeV \text{ [5]} \tag{2.4}$$

There is a direct analogy between fusion reactions and the chemical reactions that may be more familiar such as burning methane:

$$CH_4 + 2O_2 \rightarrow CO_2 + 2H_2O + \text{Heat} \tag{2.5}$$

First, this reaction will proceed provided the activation energy is provided. However, if one wants to ignite the reactants, one must transfer some of the resulting heat to the other reactants to provide their activation energy. To maintain ignition, one

[c] Enterprise and Voyager crew members excepted.

[d] For stars fainter than the sun, this fusion is accomplished by direct proton-proton reactions. For stars brighter than the sun, the conversion of of hydrogen to helium is catalyzed by carbon [6].

[e] 1 MeV = 10^6 electron volts = 1.6×10^{-13} joules. The electron volt is also used as a unit of temperature in plasma physics where 1 eV = 1.1605×10^4 K.

needs to keep the reactants hot enough, long enough, and with sufficient density to make the reaction self-sustaining.

The same principles apply to fusion. While a fusion reaction liberates a million times more energy than a typical chemical reaction, the Coulomb repulsion of the nuclei makes the activation energy higher by the same factor. For two nuclei to fuse they need to get close enough for their wavefunctions to overlap significantly. The cross-section for deuterium-tritium (DT) fusion, the most likely initial fusion fuel, has a maximum at over 100 keV.

2.3 Lawson Criteria

Lawson [7] set a lower limit for the performance of a fusion reactor. A self-sustaining reactor would need to heat some quantity of fuel and confine the hot fuel long enough and at sufficient density to produce enough fusion energy to provide the electricity needed for the heating of the original quantity of fuel. Lawson found that at 20 keV the product of the density, n, and energy confinement time, τ_E, must be:

$$n\tau_E > 6 \times 10^{19} \mathrm{m}^{-3} s. \tag{2.6}$$

This is now known as the Lawson Criterion or " break even". Achieving this criteria has been a goal of the fusion community for the last 40 years, but only recently have experiments come close to achieving the required temperature, density, and confinement time simultaneously (Q = 1 in Fig. 2-1).

Most practical fusion schemes, however, require far better parameters than those set out by Lawson's Criteria. "Ignition" (Q = ∞ in Fig. 2-1) requires that enough energy from the fusion products be confined within the plasma to maintain its temperature[f]. Producing a tokamak capable of producing igniting plasmas is arguably the next step after the current set of tokamak experiments. The International Tokamak Experimental Reactor or ITER is the current embodiment of this goal. Much of the work

[f] Note that for DT fusion, 80% of the fusion energy is carried by the neutron which does not interact with the plasma. This greatly adds to the fusion challenge.

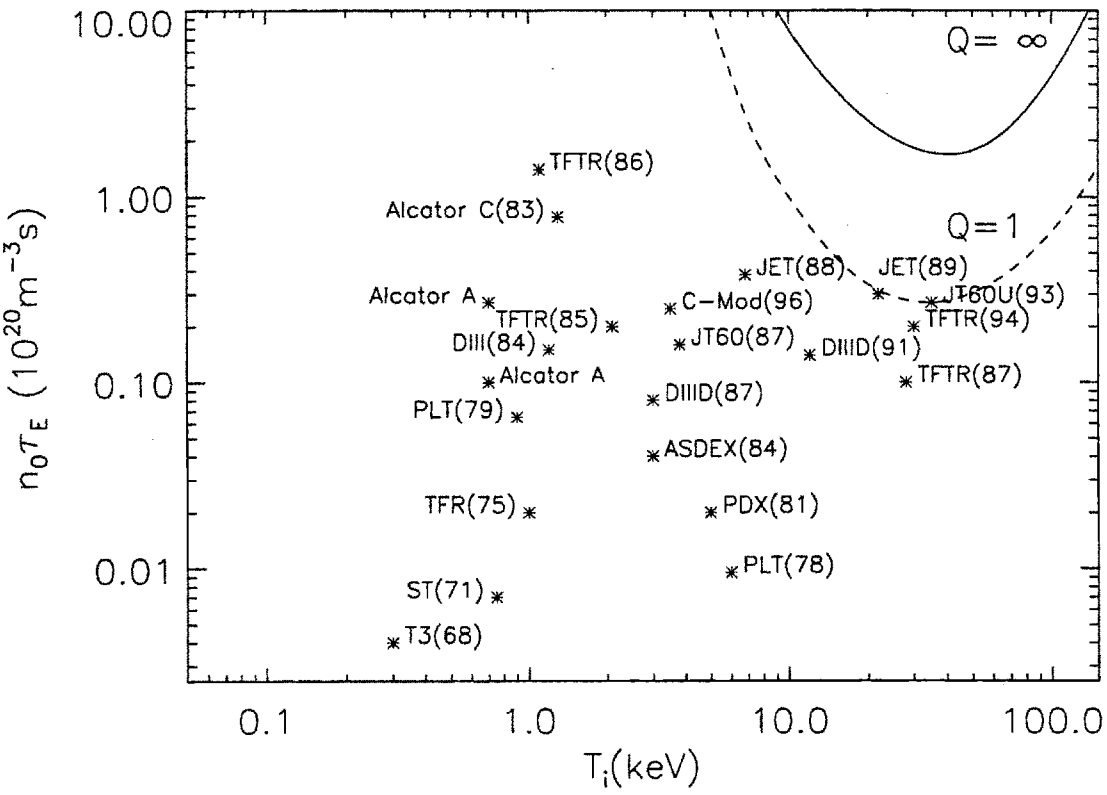

Figure 2-1: Progress Toward Plasma Fusion [8] Fusion boosters point out that over the last 25 years the percentage increase in the fusion triple product $n\tau T$ compares favorably with the growth in the number of devices per unit area on a microprocessor chip. Note that C-Mod has performance parameters comparable to machines such as JET that have 100 times C-Mod's plasma volume at 10 times C-Mod's cost.

on smaller machines such as Alcator C-Mod is conducted with the design and development of ITER, or some device like it, in mind.

2.4 Magnetic Confinement

Now that the desirability of creating extremely hot plasmas that stay hot for a significant period of time has been established, how does one do this on earth in a controlled manner? The obvious problem is heat transfer from the plasma to the vessel confining it. While many approaches to confining the hot plasma have been suggested, the

most developed technique is through magnetic confinement.

A plasma may be confined using a strong magnetic field. A particle with charge q moving in a magnetic field $\mathbf{B}$ feels a force perpendicular to both the magnetic field and its velocity: $\mathbf{F} = q(\mathbf{v} \times \mathbf{B})$. As a consequence, in a uniform magnetic field with no electric field present, charged particles stream freely along the field lines but gyrate about the field lines with a gyro (Larmor) radius and frequency given by:

$$r_L = \frac{mv_\perp}{qB} \qquad \omega_c = \frac{qB}{m} \; . \tag{2.7}$$

In the presence of an electric field, the kinematics become more complicated. The particle is free to accelerate due to the component of $\mathbf{E}$ parallel to $\mathbf{B}$; however, the component of $\mathbf{E}$ perpendicular to $\mathbf{B}$ produces a drift[g] perpendicular to both $\mathbf{E}$ and $\mathbf{B}$:

$$\mathbf{V}_{E \times B} = \mathbf{E} \times \mathbf{B}/B^2. \tag{2.8}$$

If the field lines are curved, the drift[h] relative to the B field lines due to the centrifugal force and the radial variation in the field (dictated by $\nabla \cdot \mathbf{B} = 0$) is given by:

$$\mathbf{v}_R + \mathbf{v}_{\nabla \mathbf{B}} = \frac{m}{q} \frac{\mathbf{R}_c \times \mathbf{B}}{R_c^2 B^2} \left(v_\parallel^2 + \frac{1}{2} v_\perp^2 \right) \; . \tag{2.9}$$

Any confinement scheme must at least provide $\mathbf{E}$ and $\mathbf{B}$ fields such that ionized particles are confined subject to these drifts.

An engineering principle is that breaks in symmetry lead to stress concentrations that limit the strength of a structure. Presumably the higher the magnetic field the better the plasma will be confined, so a symmetric shape for magnetic confinement is probably desirable. The current shortage of magnetic monopoles dictates that $\nabla \cdot B = 0$, precluding the possibility of a spherically symmetric magnetic confinement device. Cylindrical symmetry with $\mathbf{B}$ along the axis of symmetry ($\mathbf{z}$) fails because

[g] Logically known as the "E x B" drift.
[h] Called the curvature drift.

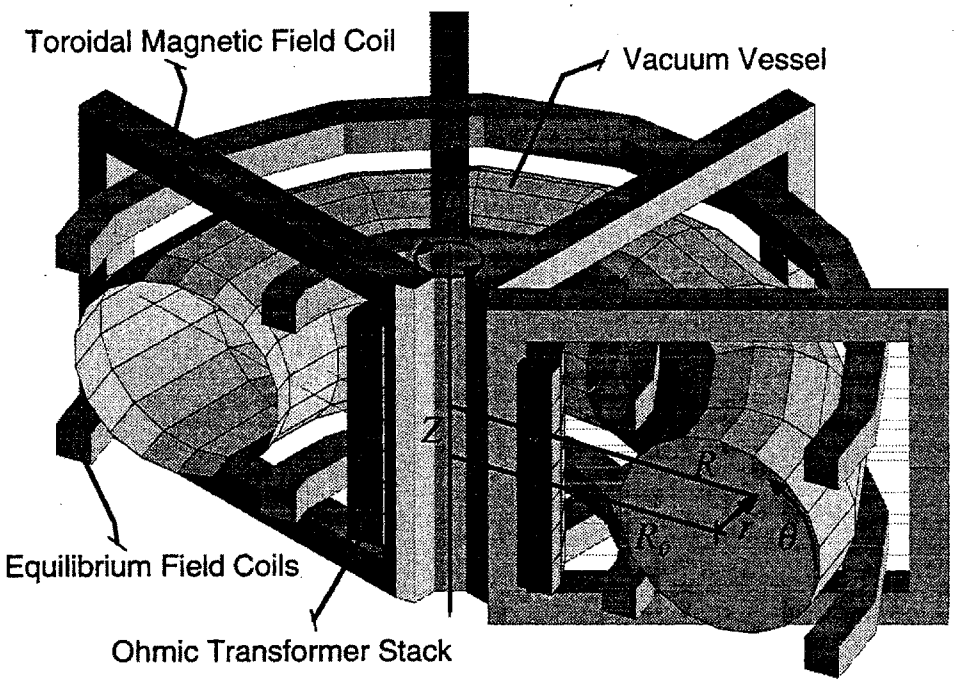

Figure 2-2: Schematic of a tokamak, indicating both cylindrical and toroidal coordinate conventions [9]

particles can stream out of the containment vessel along **z**. A cylinder with especially high fields on the ends can confine particles and was the basis of the now defunct mirror concept. Cylindrical symmetry with **B** in the ϕ direction also fails as the curvature drift forces oppositely charged particles to drift in opposite directions. This charge separation results in an electric field along **z** which in turn drives an outward radial $\mathbf{E} \times \mathbf{B}$ drift. Toroidal[3] symmetry, however does allow for particle confinement as will be discussed in the next section.

2.5 Tokamaks

Currently the tokamak[j] is the most promising concept for producing the first fusion reactor. A strong toroidal field is provided by the large toroidal field coils shown in Fig. 2-2. To avoid the vertical charge separation and resultant radial $\mathbf{E} \times \mathbf{B}$ drift discussed in the previous section, a poloidal field is introduced which allows particles streaming along a field line to short out any vertical $\mathbf{E}$ field. This poloidal field can only be provided by a toroidal current running in the plasma. The plasma current is driven by induction. Current is ramped through a coil passing through the center of the torus. This produces a change in magnetic flux through the torus, inducing a toroidal voltage and current in the plasma. External field coils provide the vertical field needed for radial force balance and allow for shaping of the plasma[k].

2.5.1 Flux Surfaces

Many problems in tokamak physics can be studied as a one dimensional system by using "flux coordinates". A tokamak plasma is sketched in Fig. 2-3. First note that there is toroidal symmetry. The magnetic flux passing through the disk drawn through point A is equal to some value ψ. Now, beginning at point A and following the poloidal B field around the center of the plasma back to A marks out a contour in the R-Z plane and a three dimensional surface, S, if it is rotated about the central axis of the tokamak. By Gaus's Law, any disk with a boundary lying wholly on the surface described by S will measure the same flux ψ. Starting from the point of highest ψ in the center of the plasma, the values of ψ describe a series of concentric "flux surfaces". This mapping is valuable because many plasma parameters are constant on a flux surface. For example, pressure balance in magnetic confinement is provided

[i]Physicists get most of their inspiration from food: The tandem mirror looks a lot like a Tootsie Roll. A tokamak is shaped like a bagel or donut. A competitor of the tokamak that forsakes all symmetry, the stellerator is also shaped like a donut but the coils spiral around the donut making it look like a cruller.

[j]The term "tokamak" is derived from the Russian words "toroidalnaya kamera magnitnya", crudely translated as toroidal magnetic chamber.

[k]While the complexity of this arrangement may remind some of the work of Rube Goldberg, it should be reiterated that this is the most symmetrical, hence least complicated, arrangement of magnetic fields for a magnetic plasma confinement device.

by $\mathbf{J} \times \mathbf{B} = \nabla$p. In addition, since ψ is constant on a flux surface, $\mathbf{B} \cdot \nabla\psi = 0$. By symmetry, both $\nabla\psi$ and ∇p lie in the R-Z plane. Since both are perpendicular to $\mathbf{B}$, $\nabla\psi$ and ∇p are everywhere parallel, hence p can be described as a function of ψ.

Another flux surface quantity is the safety factor, q. Again in Fig. 2-3, if one begins at point A and follows a field line as it travels along the surface S until one is again at the same poloidal location as A, the number of times one has traversed the tokamak toroidally is q. When q is a rational number, a perturbation on a flux surface can be resonant. Often, q = 1 near the center of the plasma. This can result in a relaxation oscillation called a sawtooth that limits the current density at the center of the plasma.[l] The current profile in most tokamak plasmas is peaked on axis, so q increases as one moves out from the center. Higher q increases plasma stability. A higher toroidal current improves confinement, but lowers q. By elongating the plasma, q at the edge can be kept high while raising the current. The left hand figure in Fig. 2-4 shows an elongated plasma. The ratio b/a is the elongation, κ.

2.5.2 Impurities

Preventing plasma contamination by impurities is a major hurdle along the road to building a fusion reactor. The first problem posed by impurities is dilution of the reactants. At reactor temperatures ($\sim$ 20 keV), light elements such as carbon and oxygen will be fully stripped of their electrons. For every percent of ions that are oxygen, an eight percent increase in the electron density and the Lawson criteria is required. In addition, alpha particles produced in a burning plasma will also dilute reactants. Once the alphas have deposited their energy in the plasma, they need to be swept out in some way. To make matters worse, in many regimes, impurities accumulate in the center, diluting the plasma where it is most reactive.

The other and generally more critical issue is radiative energy loss due to impurities. Because light elements such as carbon and oxygen are fully stripped in a hot plasma, Bremsstrahlung is the dominant radiation mechanism. The heavier elements such as iron, tungsten and molybdenum are not fully stripped in a reactor temper-

[l] In fact, almost all plasmas on Alcator C-Mod have sawtooth oscillations.

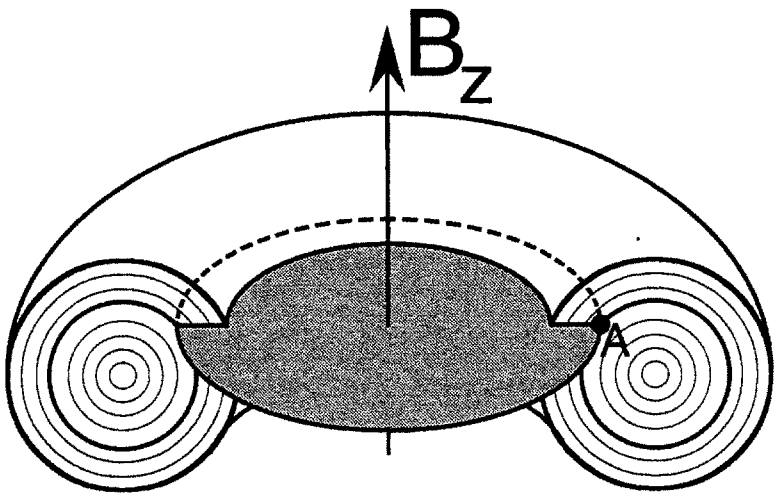

Figure 2-3: Flux Surfaces All the points on the torus passing through the point A have the same value of ψ and to first order the same values of pressure, temperature, and density.

ature plasma. So not only are they more effective radiators of Bremsstrahlung, but they emit line radiation also. An ion fraction of less than .05% molybdenum is enough to radiate half of the alpha particle heating in a 10 keV plasma, effectively doubling the performance needed to reach ignition.

While high Z materials such as molybdenum pose serious problems if they get into the main plasma, they do have some advantages over low Z materials such as carbon as a plasma facing material. The first advantage is that the sputtering yield[m] of molybdenum by impacting deuterium ions is lower by two orders of magnitude than the sputtering yield of carbon at temperatures below 100 eV. Thus, far fewer molybdenum atoms will get into the plasma. The second issue is desorption of adsorbed gas from the plasma facing surfaces. Carbon can adsorb 0.4 hydrogen atoms for every carbon atom. The impact of ions and neutrals from the plasma on carbon surfaces can release these atoms. In addition, hydrogen is quite mobile in a graphite lattice,

[m]The sputtering yield is the number of atoms liberated from a surface for every impacting atom.

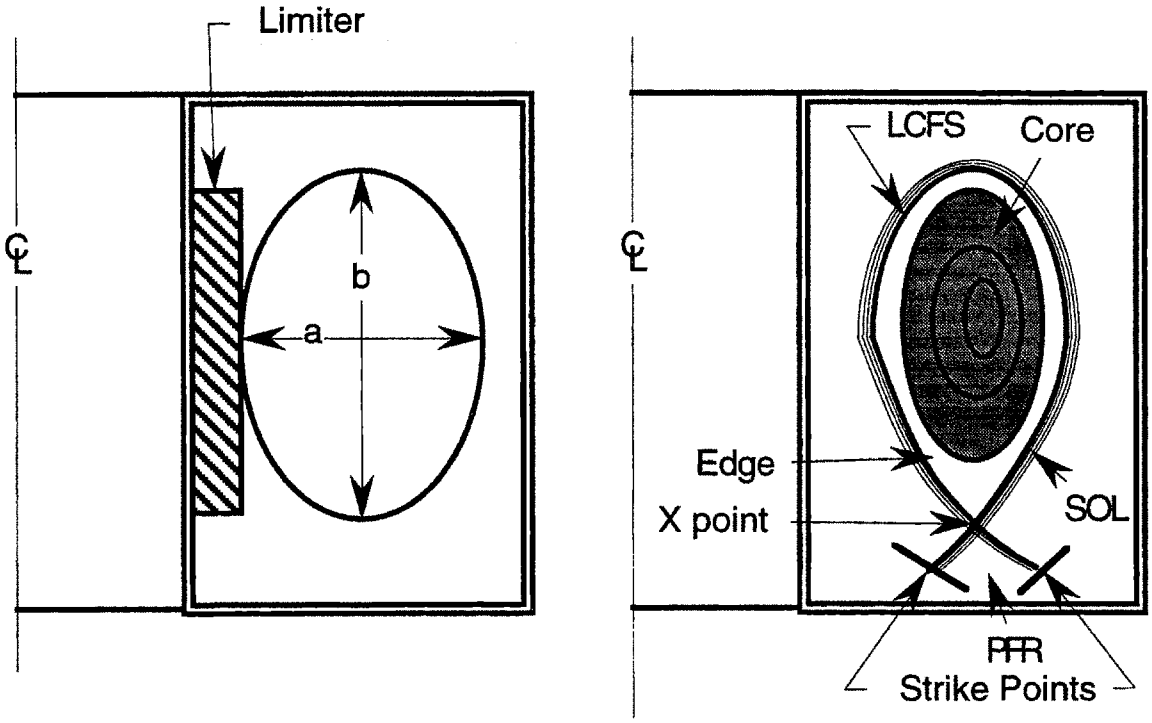

Figure 2-4: Limited and Diverted Plasmas The figure on the left is a cross section of a limited plasma with an elongation of $\kappa = b/a$. Impurities generated at the plasma/wall interface (limiter) are free to enter the main plasma. On the right is a diverted plasma. Note that the plasma/wall interface (strike points) are well removed from the main plasma.

so a hydrogen inventory tens or hundreds of times the plasma inventory is available in the walls of a carbon tiled machine. As a result, neutral and plasma density can be difficult to control in a carbon tiled machine.

2.5.3 Limiters and Divertors

The plasma must at some point contact a material surface. At this interface, energetic ions can sputter atoms off the surface. These atoms can then enter the main plasma. In addition, atoms adsorbed on the surface can be liberated by incident ions. Typically there is a dynamic equilibrium between the rate of incidence and of desorption, so a material surface can act like either a pump or a source. Also, as a surface is heated, adsorbed atoms are liberated. And of course the material can melt,

sublimate, or fracture if the constant or temporary heat load on the surface is too high.

The simplest technique for providing a plasma/solid interface is a limiter, shown on the left in Fig. 2-4. Here, the edge of the plasma is defined by a piece of material designed to withstand the heat load from the plasma. The main problem with this arrangement is that atoms liberated from the limiter surface by impacting ions are free to enter the main plasma. This problem can be avoided in principle by using a magnetic divertor, shown on the right in Fig. 2-4. Particles that exit the main plasma stream along the magnetic field lines to contact material walls well removed from the main plasma.

The "last closed flux surface" (LCFS) or "separatrix" is the outermost flux surface that encircles the plasma without contacting a material surface. The "X-point" is the point on the LCFS where the magnetic field is exactly toroidal. From this point, particles on a flux surface can either circle the plasma or go to the divertor. The points where the LCFS intersect the divertor plates are the inner and outer strike points. The "'core" plasma is the central portion of the plasma. Its boundary is not precisely defined, but can be taken as the region where the temperature is at least 30% of the central temperature. The "edge" plasma is the plasma outside of the core plasma. The "scrape-off layer" (SOL) is the plasma outside of the LCFS, a subsection of the edge. The "private flux region" (PFR) is the region below the separatrix in the divertor region.

The divertor has four functions. First, it provides a boundary for the plasma that is not a material surface. Second, neutrals and neutral impurities entering the scrape-off layer are ionized and pumped to the divertor, away from the main plasma. Third, along the path to the strike point, the plasma can be cooled through collisions to reduce sputtering at the strike point. And fourth, the heat destined for the strike points can be dissipated by intentionally introducing impurities to cool the plasma through radiation. This is called a "dissipative divertor".

2.6 Energy Transport and H-Modes

The transport of energy deposited in the center of a tokamak plasma is poorly understood. Simple models of gyrating and drifting particles colliding with each other, thus transporting energy in a diffusive manner, greatly underestimate the rate at which energy is carried across field lines. This anomalous cross field transport is probably due to turbulence driven by temperature and density gradients in the plasma. An accurate picture of this turbulence is beyond the capabilities of current plasma diagnostics. As a result, predictive models of confinement in a future machine based on the details of energy transport are not available. However, by mapping out energy confinement as a function of the various parameters that can be controlled, a scaling of the energy confinement with respect to the plasma density, temperature, current, major radius, etc. can be developed which can empirically predict the performance of future machines. Kaye and Goldston [1] studied confinement in several machines and identified a mode of operation for auxiliary heated plasmas where $\tau_E \propto I_p P^{-\gamma}$, where $1/3 \leq \gamma \leq 1/2$, I_p is the plasma current, and P is the input power. This scaling was later named Low or L-Mode[n], and has been modified somewhat over time giving the ITER89-P [10]scaling law:

$$\tau_{ITER89-P} = .048 I_p^{0.85} R^{1.2} a^{0.3} \kappa^{0.5} n_e^{0.1} B_t^{0.2} amu^{0.5} P^{-0.5}, \tag{2.10}$$

where R is the major radius, a is the minor radius, κ is the plasma elongation, n_e is the central electron density, B_t is the toroidal magnetic field, and amu is the average atomic mass unit of the ions (all units are MKS). The ITER89-P scaling has proven very robust in predicting confinement in the basic mode of operation for virtually all large tokamaks.

The rather poor confinement observed in L-mode points to very large and ex-

[n]This rather unfortunate name refers to a 'mode' of operation. The nomenclature is unfortunate because 'mode' is also used throughout plasma physics to discuss eigenmodes of some equation. These eigenmodes typically are the cause of some degradation in confinement. PEP, super, and H describe good confinement modes of operation while ITG, ubiquitous, ballooning, tearing, and kink describe particular transport driving (bad) plasma instabilities.

pensive fusion reactors. This unfortunate result has encouraged extensive research into operating regimes with better than L-Mode confinement. Stambaugh et al. [2] reviewed research in "Enhanced Confinement Modes" of operation. They distinguish between two groups: those characterized by peaked density profiles, and those with flat density profiles. The first group includes PEP (Pellet Enhanced Performance), Super, and IOC (Improved Ohmic Confinement) modes. The improved confinement of all of these modes is assumed by many to be due to suppression of the ion temperature gradient (ITG) mode[o]. Plasmas having density profiles that are more peaked than the ion temperature profile are believed to be stable to this mode. The second group of enhanced confinement modes consists of the many variations of "High" or "H-Mode" which will be discussed below.

2.6.1 H-Mode Characteristics

Groebner [11] provides a recent review of H-mode experimental observations. The US-Japan Workshop on H-Mode Physics [12] is a comprehensive and up to date (1995) presentation of the current status of H-mode experiments and theory worldwide. The H-mode was first seen on ASDEX [3] in 1982 and has since been observed on virtually all high performance tokamaks. Above some threshold edge temperature or applied heating power, a transport barrier can form in the plasma edge resulting in greatly improved global particle confinement and typically a factor of two improvement in global energy confinement over L-mode levels. Typically, H-modes are observed during divertor operation, though they have been observed on some limiter machines[p]. H-modes have also been induced in low input power tokamaks by biasing the plasma relative to the vacuum chamber.

In diverted plasmas, several phenomena characterize the transition from L-mode to H-mode (L-H transition). The two most apparent phenomena are a dramatic

[o]Originally known as the η_i mode.

[p]Rather than reference individual machines, the interested reader is referred to the papers by Groebner and Stambaugh cited above.

rise in the plasma density and a drop in D-alpha emission[q]. The rise in density appears to be the result of improved particle confinement, while the drop in the D-alpha emission is a signature of a decrease in the recycling of deuterium in the SOL. It is important to note that while the drop in D-alpha emission does indicate an increase in the confinement time of the whole plasma (SOL and PFR included!), it does not directly translate to a change in the core plasma particle confinement. As the H-mode progresses, the recycling light may return to or even exceed the original emission levels.

Other key phenomena observed at the L-H transition are an increase in the electron density inside the LCFS and a drop in the density outside the LCFS. In the steep gradient region (SGR) near the LCFS, density fluctuations appear to be suppressed in H-mode. The electron temperature typically increases at the transition. Other characteristics observed with the proper diagnostic set include a dramatic increase in impurity confinement and a large sheared poloidal rotation in the SGR. Typically, the core density and temperature profiles during H-mode are flatter than during L-mode operation. Edge Localized Modes (ELMs) appear in most long duration H-modes and can be identified as bursts of D-alpha emission and magnetohydrodynamic (MHD) fluctuations. ELMs come in many varieties and are a temporary relaxation of the high pressure gradient at the edge. In some machines as much as 5% of the plasma's stored energy can be released in a single 1 ms ELM, making ELMs the source of the highest peak heat loads in these machines. While ELMs do degrade energy confinement, they also appear to control the buildup of impurities and control the rise in plasma density. An ELM-free H-mode with low recycling is always a transient phemonena as impurity radiation and uncontrolled density rise eventually lead to a cooling of the SGR and a return to L-mode.

Operationally, four other factors affect access to and maintenance of H-modes. The first is wall cleanliness and conditioning. Presumably, low neutral pressure and

[q]These phenomena can occur for reasons other than an L-H transition. For example, impurity injections, MARFEs, and changes in divertor operation can greatly change the plasma density and D-alpha emission. Distinguishing periods of H-mode operation from these other phenomena during early C-Mod operation was something of a challenge.

low impurity levels aid in achieving the high edge temperatures required for H-mode operation. Second, the size of the gap between the LCFS and any walls or limiters needs to be as large as practical with the particular heating scheme being used. This also is probably related to reducing sputtering or desorption of impurity and majority atoms. Third, the direction of the ion $\mathbf{B} \times \nabla \mathbf{B}$ drift should be towards the divertor. Directing the ion $\mathbf{B} \times \nabla \mathbf{B}$ drift away from the divertor typically requires twice the input power to achieve H-mode. Fourth, the density must be within some range for a given input power. A low density limit has been seen on most machines. While the cause of the low density limit is not clear, higher impurity fractions, locked modes, and smaller sawteeth are possible reasons. The upper density limit is related to the energy density achievable for a given input power and the temperature needed to achieve H-mode.

Energy confinement during H-mode is typically twice the value expected with ITER89-P scaling and is generally believed to be largely due to a suppression in transport at the edge. Both JET and DIII-D have achieved H factors approaching four during "Hot Ion H-modes" on JET and during "VH-modes" on DIII-D. In the VH-modes, poloidal rotation and suppressed fluctuations extend inward over most of the plasma radius, apparently combining the good qualities of both central and edge enhanced confinement regimes.

2.6.2 Model for Transport Barrier

All machines that attain H-modes and have the capability to measure significant plasma rotation observe a sheared poloidal plasma rotation during H-mode. This shear is most likely caused by an $\mathbf{E} \times \mathbf{B}$ drift, driven by a radial electric field, E_r[r]. The interested reader is referred to the review article by Ward [13]. A sheared flow perpendicular to a density gradient decorrelates the convective eddies that drive the transport. The skewed eddies are thus more heavily damped by the increased relative speed between eddies. In addition, the skewed eddies break up into smaller eddies,

[r]The source of this electric field, is the cause of much speculation and is beyond the scope of this thesis.

reducing the step size for a volume of plasma moving across the pressure gradient. Together, these effects enable a sheared flow to produce a transport barrier.

2.6.3 Issues for H-Modes in a Reactor

Current plans for test reactors such as ITER count on obtaining a factor of two improvement in energy confinement by running in H-mode rather than L-mode. However, operating in H-mode presents five major challenges, three of which, ironically, are a result of overly good particle confinement. The first problem is the accumulation of impurities and helium. Some mechanism needs to be developed to sweep out impurities and ash without significantly reducing energy confinement. The second issue is controlling the density in H-mode. As the plasma density rises, the heating power needed to reach ignition temperatures also goes up. Third, the low SOL density seen in H-modes reduces the coupling of ICRF and lower-hybrid waves to the plasma, reducing the power launched per unit area of antenna. Fourth, the high peak heat loads due to type one ELMs complicate divertor designs. And fifth, the high edge temperatures required for H-mode operation are difficult to incorporate in dissipative divertor concepts.

Chapter 3

Alcator C-Mod

The Alcator C-Mod[a] (hereinafter "C-Mod") tokamak is the third of the Alcator line of tokamaks built at the Massachusetts Institute of Technology. Alcator A and Alcator C[b] were both compact, high magnetic field, high electron density tokamaks with circular poloidal cross-sections. C-Mod was built to test shaped and diverted plasmas in a compact, high magnetic field tokamak. As the only large tokamak to be commissioned in the United States in the last decade, C-Mod benefits from and tests some of the latest concepts in plasma physics and fusion technology.

[a]C-Mod was originally proposed as a modification of the Alcator C tokamak, hence the name "C-Mod". However, as the design work progressed it became clear that very little of the original machine could be used. In fact, rather than being modified for use in C-Mod, the Alcator C vacuum chamber, power supplies, and magnets were shipped to Lawrence Livermore National Lab where they became the MTX experiment.

[b]Commissioned in 1973 and 1979, respectively.

Parameter	Symbol	Typical	Maximum
Major Radius	R	0.67 m	-
Minor Radius	a	0.22 m	-
Elongation	κ	1.7	1.85
Toroidal Field	B_T	5.3 tesla	7.9 tesla
Density	n_e	1.5×10^{20} m^{-3}	1.2×10^{21} m^{-3}
Plasma Current	I_p	.8 MA	1.5 MA
ICRF Power	P_{ICRF}	2 MW	3.5 MW

Table 3.1: Alcator C-Mod Parameters (as of August 1996) The plasma current and auxiliary power is expected to increase in the coming years.

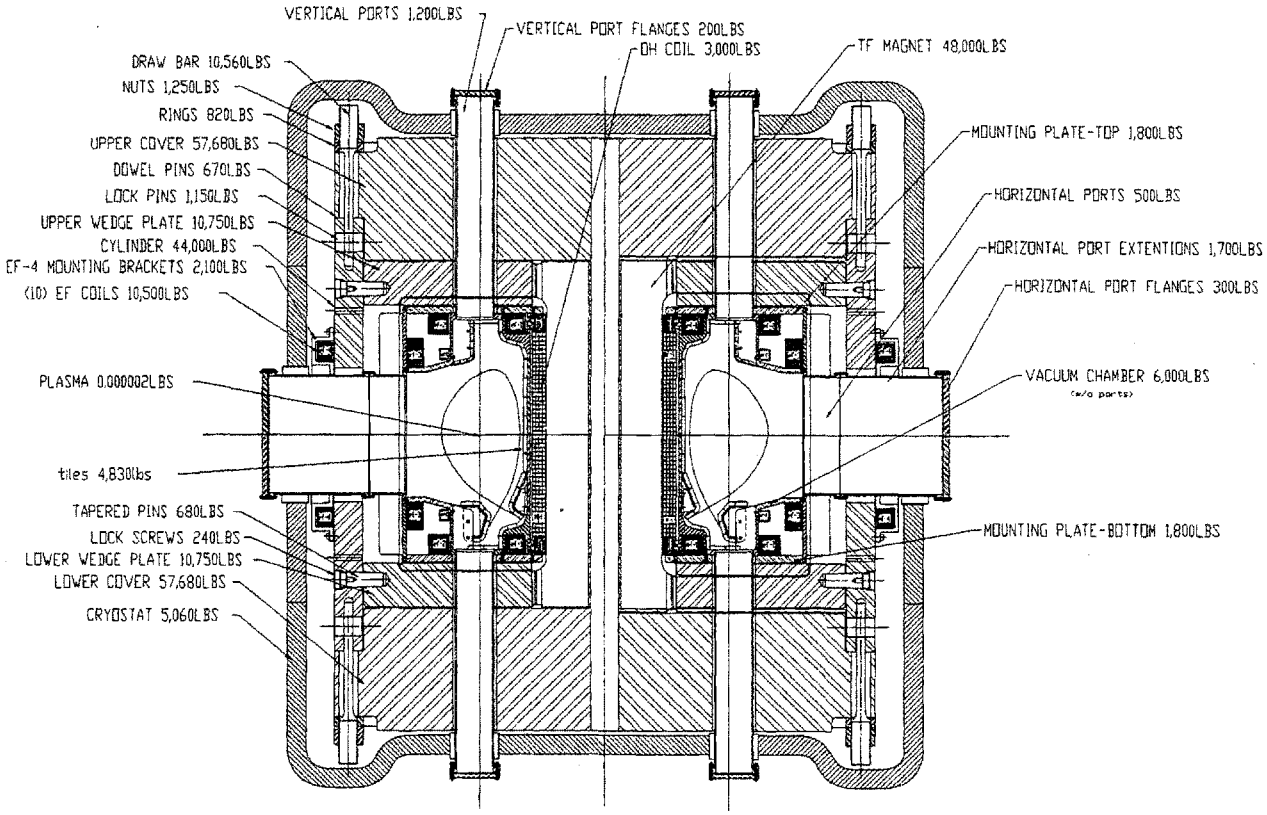

Figure 3-1: Alcator C-Mod Cross Section [14] The machine sits atop three six foot pillars in the center of a 50 x 50 x 40 foot experimental cell. Surrounding the shown structure is a two foot thick "igloo" constructed of boronized concrete for radiation attenuatation.

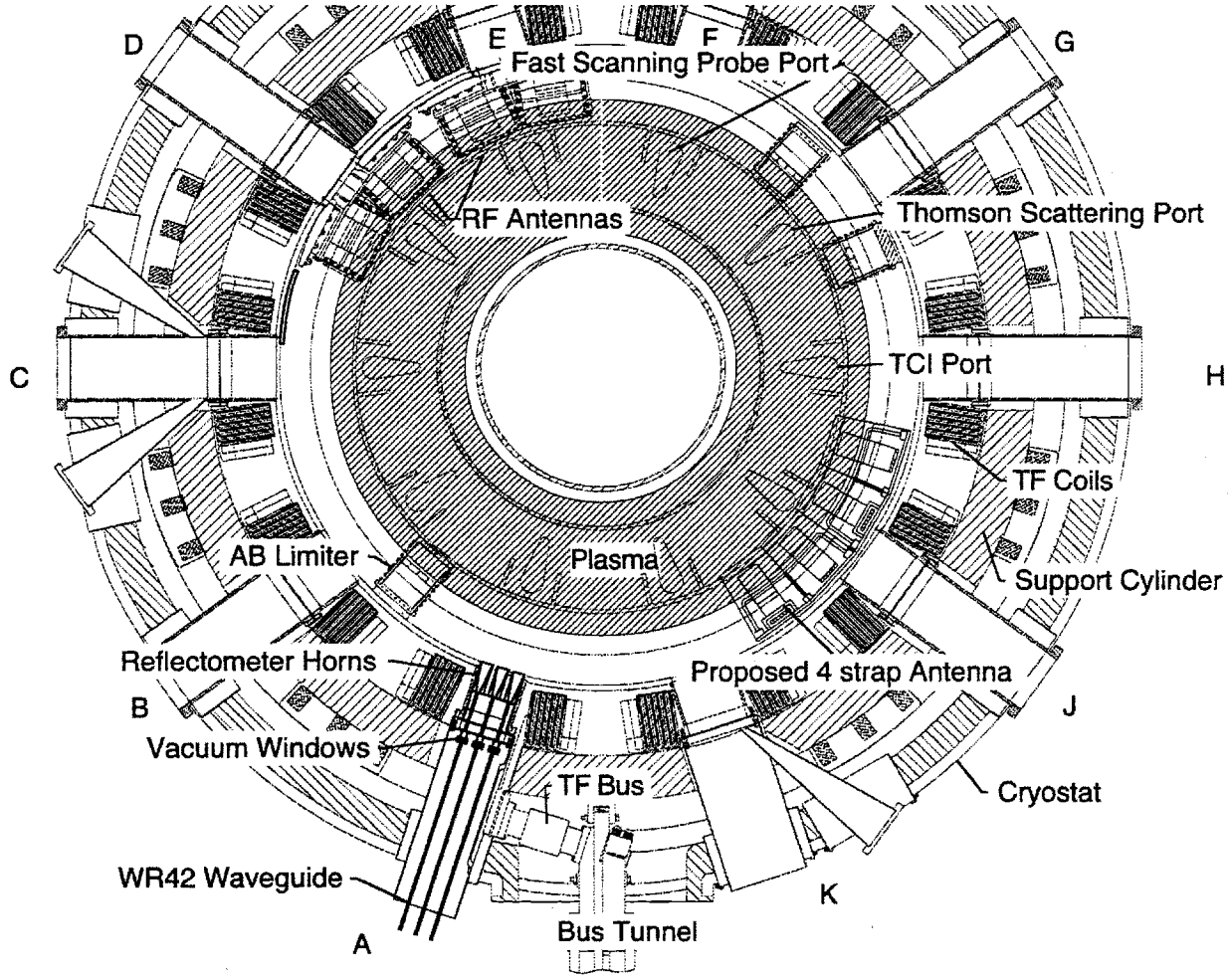

Figure 3-2: Top View of Machine The diameter of the cryostat is approximately four meters. The major density diagnostics are labeled.

3.1 Major Components

C-Mod developed from the collaboration of scientists and engineers from many disciplines. No physics thesis is complete without at least pointing out a few of the major engineering efforts involved in building and running this machine.

Vacuum Chamber: The stainless steel C-Mod vacuum chamber is unique in several ways. First, it is a torus without a poloidal insulating break. This allows the chamber to be strong enough to support the poloidal field coils. This is key to producing a shaped, compact, high field tokamak because there is no space for an independent support structure for the poloidal field coils. Second, the walls of the

vacuum chamber are 0.75 inch thick in order to support these coils.

These features create a few problems. Because the chamber can not be separated during maintenance periods, the only access to the machine is through one of the nine eight-inch-wide horizontal ports[c]. Only two people are able to work inside the chamber simultaneously during maintenance periods and all objects installed in the chamber must be small enough to be moved manually. Another problem is that without an electrical break, large toroidal currents are driven in the chamber walls during plasma initiation. In addition, the fields created by the poloidal field coils take on the order of a millisecond to penetrate the vacuum vessel. Nonetheless, future reactors are also expected to have thick conducting vacuum chambers and will thus face the same problems.

TF Coils: The toroidal field (TF) coils on C-Mod are capable of producing a 9 tesla field on the major axis of the machine. Because the vacuum chamber does not come apart, the coils must have a break in them. Each of the twenty coils contains six turns and are constructed of four sections: a top, a bottom, an outer leg, and a section of the central column which passes through the center of the donut shaped vacuum chamber. Because copper is not strong enough to support the stresses to which the C-Mod magnets are subjected, the sections of the coils are constructed of a laminate composed of high conductivity copper and Inconel. The coils are supported by a thick, stainless steel superstructure. The individual sections of each coil are allowed to move so that they may press against the support structure. This required the development of sliding, conducting joints for coils carrying 250 kiloamperes in each turn. The TF coils have worked without problem and provide a field ripple of less than one percent everywhere inside the limiter radius.

Support Structure: The TF magnets are supported by a thick, stainless steel superstructure comprised of the upper cover, the lower cover, and the cylinder, as shown in figure 3-1. These three pieces weigh 80 tons and are held together by 96 Inconel bolts, each of which is preloaded to 500,000 lbs. Operationally, this structure

[c]The tenth horizontal port, A-port, is six inches wide to accommodate the toroidal field coil bus. There are twenty vertically viewing ports, each is teardrop shaped, seven inches long and two inches wide at the widest.

carries significant eddy currents adding to the challenge of obtaining a field null at plasma initiation.

Poloidal Field Coils: The plasma current, position, and shape are provided by a set of three ohmic heating coils wrapped around the central TF column and five pairs of poloidal field (PF) coils. They are also called equilibrium field (EF) coils. This coil set, despite being rather removed from the plasma boundary, allows for a wide variety of plasma shapes and divertor geometries. The joints between these coils and the buswork were replaced in 1993 by electroforming new joints on the ends of the coils, a unique application of a technology usually reserved for precision microwave components.

Cryogenics: The coils and the superstructure of C-Mod all operate at liquid nitrogen temperatures. This increases the conductivity of the copper by a factor of five to six. Cooling of the magnets is accomplished by boiling off liquid nitrogen[d]. The vacuum vessel temperature must be controlled independently of the the coils to ensure vacuum integrity. Typically, the vacuum vessel operates near room temperature. The tokamak takes approximately one week to cool down after a maintenance period or to warm up at the beginning of a maintenance period. Warming up the machine too fast will create thermal gradients that can deform or crack the superstructure. Also, during a run, nitrogen escaping from the cryostat displaces some of the oxygen in the experimental cell which reduces the oxygen level below OSHA designated standards, and thus prevents access to the experimental cell between shots[e]. Typically, the cooling time of the magnets is the rate determining step in the experimental shot cycle.

Power Systems: Twelve power supplies transfer as much as 500 MJ into the C-Mod coils during a 1.5 second shot. The power to run these supplies is extracted from an alternator and flywheel located adjacent to the C-Mod experimental cell. The flywheel is spun up during the fifteen to twenty minute period between shots.

[d] LN_2 is a significant portion of the C-Mod operating budget, accounting for approximately $1 million per year.

[e] Improvements in the cooling system and the cryostat have greatly reduced the amount of nitrogen escaping into the cell. Cell access between shots is now somewhat more common, though still frowned upon.

The 72 ton flywheel is the world's largest single stainless steel forging.

Computer Controls: Most of the power supplies and other machine controls such as gas valves, are controlled with a custom built, digitally programmable analog computer. This hybrid computer can take up to 96 analog input signals which typically include most of the magnetics, along with a channel of the interferometer, bolometer, and visible bremsstrahlung array. The input vector is multiplied by a matrix to determine a vector of outputs that represent the quantities to be controlled such as plasma position, plasma current, strike point location, and plasma density. These outputs are then compared to the desired values and the difference, the time derivative of the difference, or the integral of the difference is produced. The resulting vector is then multiplied by a second matrix to give the voltages to be sent to the power supplies and gas valves to control the plasma. The hybrid computer has a 1 ms response time.

3.2 Diagnosing C-Mod Plasmas

Alcator C-Mod has an extensive diagnostic set, too large to discuss here. A thorough discussion of the various diagnostics can be found in the C-Mod Five Year Research Program [14] and in the article by Marmar [15]. Some of the main diagnostics other than the reflectometer are described below.

3.2.1 Two Color Interferometer

The primary electron density diagnostic on C-Mod is the Two Color Interferometer [19] or TCI. It consists of coaxial carbon-dioxide (CO_2) and helium-neon (He:Ne) laser beams in a Michelson configuration. The view of the interferometer is shown in Fig. 3-3. Both beams are expanded to ellipses to fill a vertical port. Ten detectors evenly spaced across the CO_2 beam measure the phase shift across the face of the beam while four detectors measure the phase shift of He:Ne beam. The CO_2 beam is sensitive to the line integral of the plasma density and to the motions of the interferometer optics. The He:Ne beam is much more sensitive to the motion of the optics

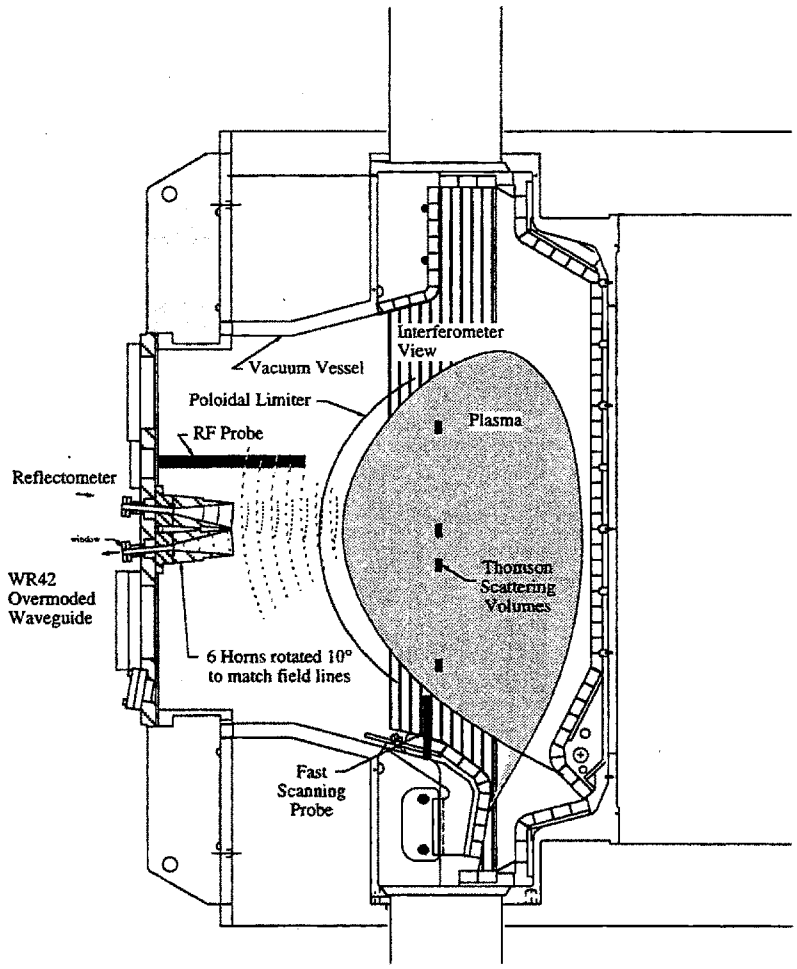

Figure 3-3: Alcator C-Mod Density Diagnostics Cross section of the Alcator C-Mod device with all major density diagnostics mapped to the same toroidal position. The RF probe shown here is being replaced with a fast scanning probe [16]. Also, an edge Thomson scattering diagnostic is under development in order to view the plasma near the X-point [17] along with a toroidally viewing interferometer [18].

and less sensitive to the plasma density than the CO_2 beam. Together these can be used to separate the phase shift caused by vibrations and plasma. The line integrated density measurements are typically good to 5×10^{18} m^{-3}. Data from one channel is available in real time for density feedback using the hybrid computer discussed in § 3.1.

The TCI has two limitations. First, the beam passes through a large portion of the vacuum chamber above and below the main plasma. There can be a large inventory of cold (> 10 ev), relatively dense (10^{19} to 10^{21} m^{-3}) plasma in these regions. These SOL plasmas are currently not measured or modeled sufficiently to separate edge and main plasma contributions to the path integrated density measurements.

The second problem is the limited view port size. The small port size results in all the TCI chords passing through both the edge and the core of the plasma. Fig. 3-4 shows the expected measurements for several different profiles which give identical phase shift measurements on channel 4. Distinguishing between all but the most extreme cases is not possible given the limited radial view. These limitations make density gradient measurements unreliable, however the central density measured by the TCI should be good to twenty percent in all but pellet fueled plasmas.

3.2.2 Core Nd:YAG Thomson Scattering

Another key density diagnostic is the Thomson Scattering System (TS). This is based on a multipulse (50 Hz) Nd:YAG laser shining through a vertical port and viewed at up to nineteen vertical positions[f] through a horizontal port. Temperature measurements are made by observing the doppler broadening of the laser light due to motion of the electrons. Density measurements are made by observing the amplitude of the scattered light. Properly calibrated, this diagnostic has the ability to make local (2 cm resolution) measurements of the free electron density and temperature with, usually, a five percent random error due to photon statistics. The challenges of this diagnostic are maintaining alignment, reducing the stray light, and absolutely

[f] For the period during which the data for this thesis were taken, three or four channels were operating.

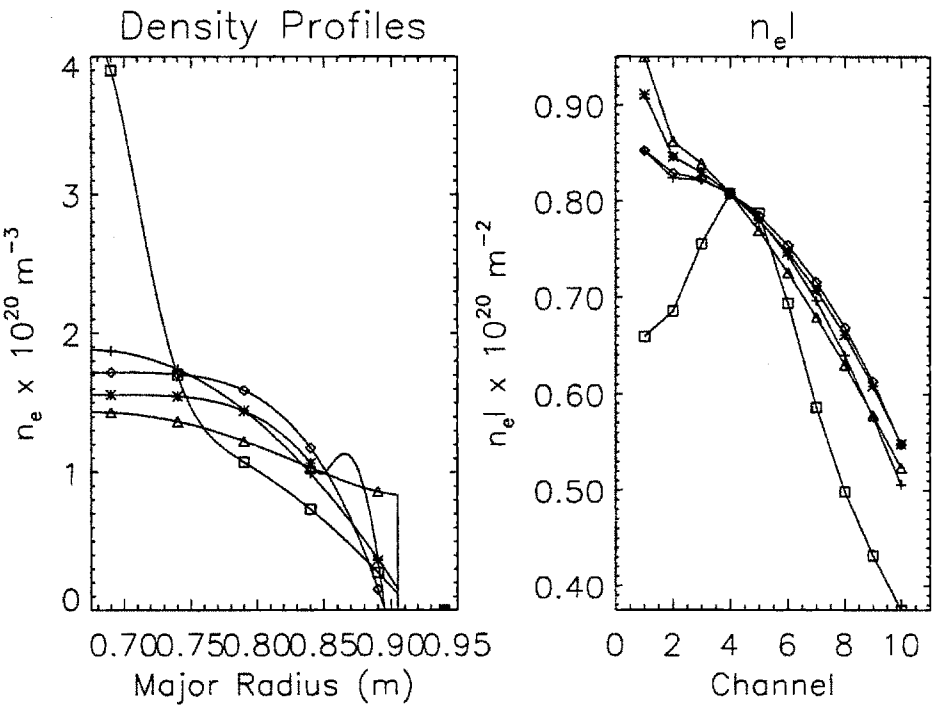

Figure 3-4: Modeled TCI Measurements for several density profiles. Note that the quite different profile shapes shown on the left result in nearly identical path length measurements on the right, making profile inversion difficult.

calibrating the device. While the signal to noise of the temperature measurement depends on the absolute power and alignment of the beam, the Thomson scattering temperature measurement is in general believed to be reliable. However the density measurement depends directly on the amplitude of the light collected and is very sensitive to alignment, changes in the collection optics, and efficiency of the detectors. Calibration of the Thomson Scattering using the reflectometer will be discussed in § 6.4.4.

3.2.3 Probes

Lagmuir probes are used to measure edge plasma parameters at several locations within the machine [20]. In the divertor, there are sixteen sets of three probes each on the inner and outer divertor surfaces (see Fig. 3-5). In addition, there are probes on the front faces of the limiters and a movable rf probe at A-port (the same port used by

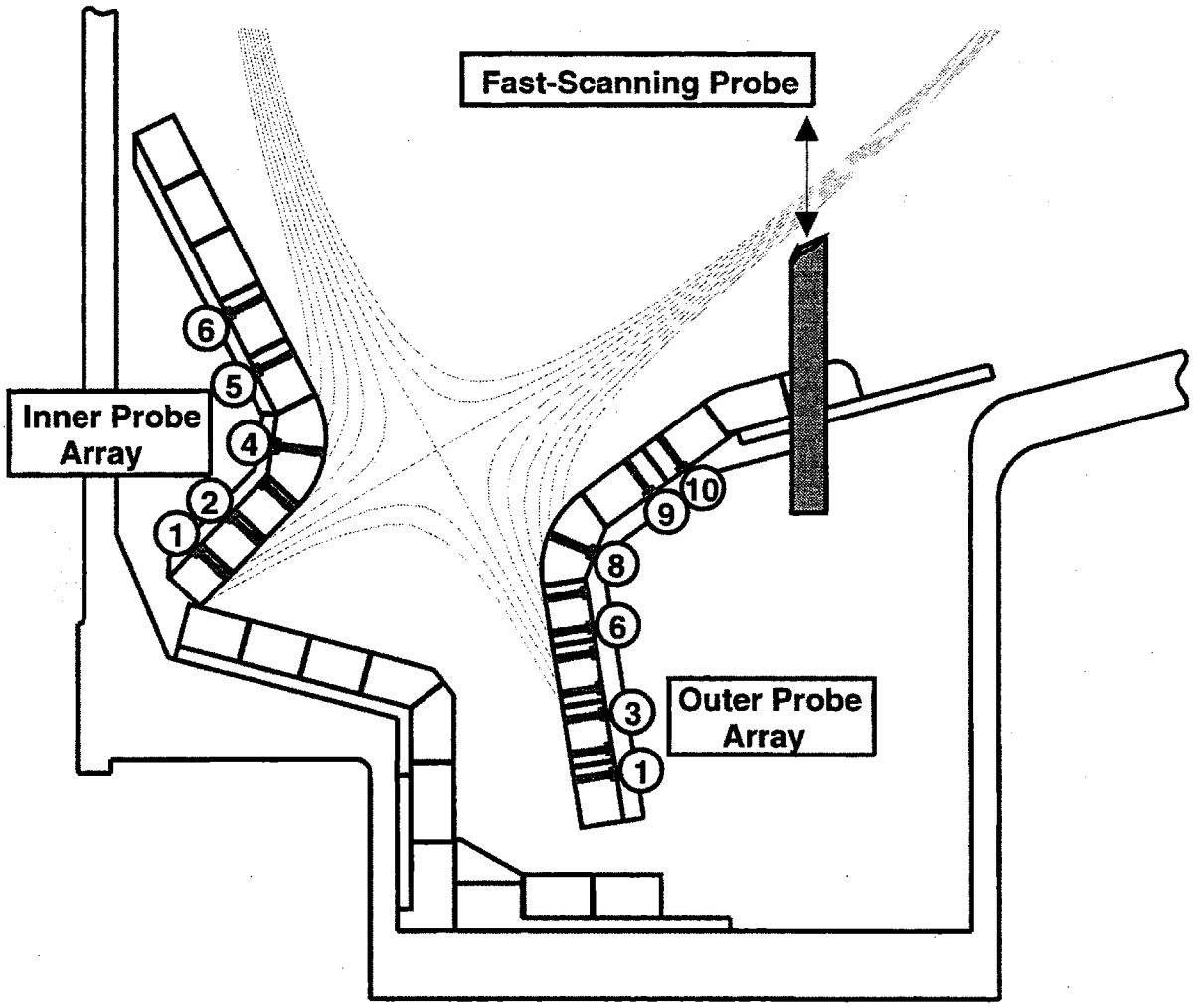

Figure 3-5: C-Mod Divertor Including Fast Scanning and Langmuir Probes [20]

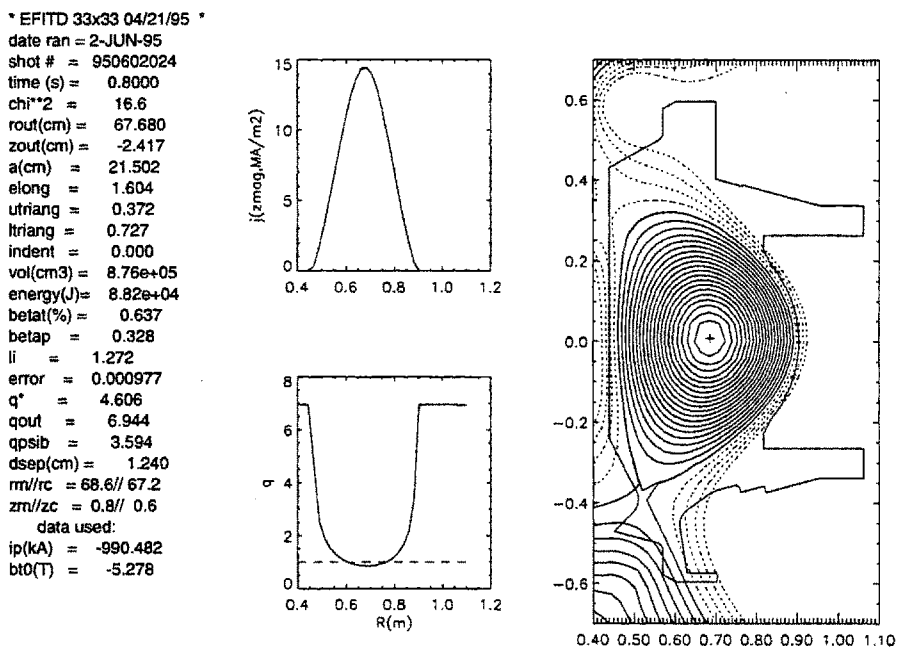

Figure 3-6: Example EFIT Reconstruction

the reflectometer). Finally, a fast scanning probe can be fired vertically to the LCFS. This probe generates edge temperature and density profiles with excellent spacial resolution up to three times per shot. Currently it is limited to ohmic operation.

3.2.4 Magnetics and EFIT

The equilibrium fitting code EFIT [21] numerically solves the Grad-Shafranov equation based on inputs from the magnetics diagnostics [22]. Fig. 3-6 shows the curves of constant flux as reconstructed by EFIT. Currently the only internal magnetic field measurement is the tilt angle of the ablation cloud from injected lithium pellets [9]. Such measurements are extremely perturbative and are not a part of normal operation. In addition no data from kinetic measurements are included. As a result, the current profile determined by EFIT is parabolic. Comparison of the LCFS location measured during L-mode by the divertor probes, the fast scanning probe, and EFIT indicate that EFIT predicts the LCFS location to within 3 mm. The accuracy of EFIT is less certain during H-modes and PEP modes as the current profile during

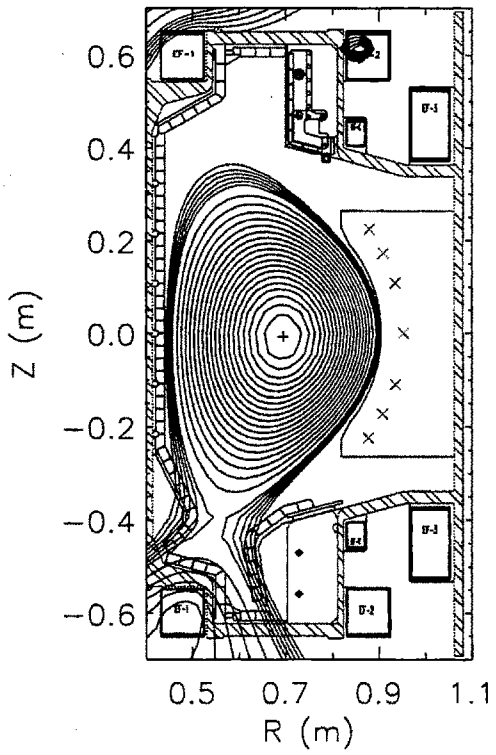

Figure 3-7: B-Dot Coils The crosses mark the poloidal location of the fast magnetic coils mounted on the 3 poloidal limiters. There is also an array of fast coils under the tiles on the inner wall.

these modes is not expected to be parabolic. A diagnostic neutral beam is currently being modified for use on C-Mod to address this issue. In addition to the magnetics used for magnetic profile reconstruction, arrays of fast magnetic pickup coils with a 500 kHz frequency response are attached to the limiters as shown in Fig. 3-7 at four toroidal locations to measure m and n numbers for magnetic fluctuations.

3.2.5 Electron Cyclotron Emission

Two Electron Cyclotron Emission (ECE) diagnostics have been installed on C-Mod for measuring electron temperatures. The Michelson Interferometer [23, 24] uses a scanning mirror arrangement to measure a temperature profile every 30 milliseconds. It is connected to the machine via a long quasioptical beam line equipped with a liquid nitrogen temperature calibration source. The beam views radially across the

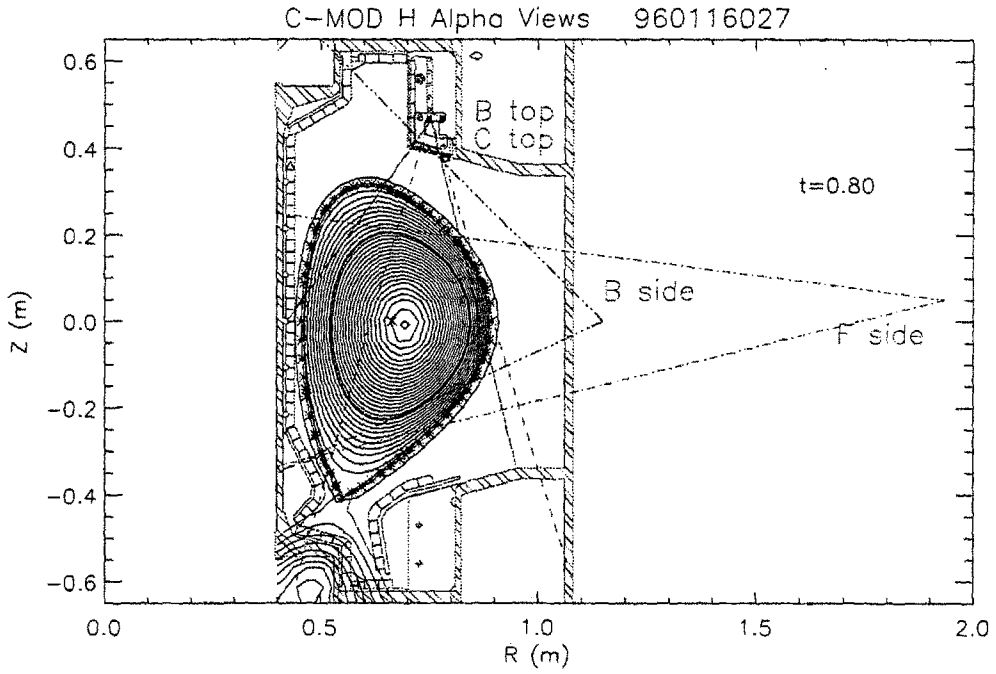

Figure 3-8: Visible Diode Array Views [25] The views have been mapped to the same toroidal location.

midplane with a spot size of ~ 3 cm in the poloidal direction. Attached to the same beamline is a nine channel grating polychromator (GPC) which is cross calibrated relative to the Michelson. The GPC has up to a 500 KHz frequency response and a 1.5 cm spacial and 9 eV thermal resolution. A third ECE diagnostic, a heterodyne radiometer, is under development for diagnosing temperature fluctuations.

3.2.6 Spectroscopic Measurements

C-Mod has a host of spectrometers to study the line emission from the visible to the X-ray. In addition, five imaging diode arrays [25] (shown in Fig. 3-8) image the D-α emission and typically a carbon line. Four of the five arrays use Reticon linear diode arrays and have 1 KHz frequency response. Top Array 1 has up to 1 MHz response for viewing ELMs and hydrogen pellet ablation. Kurz [26] has combined the information from all these arrays to perform tomographic reconstruction of the emission.

3.3 Major Areas of Physics Research

3.3.1 Transport Scaling

As discussed in §2.6, one of the most daunting problems facing plasma physics is understanding energy transport in a tokamak sufficiently to be able to predict the performance of a reactor. With its high magnetic field, high current density, and high electron density, Alcator can explore a range of parameters that are complimentary to what the rest of the fusion community can observe. For example, one important result is the testing of neo-Alcator scaling in shaped plasmas. Studies on the circular Alcator C tokamak produced the neo-Alcator scaling law [27] for the energy confinement time:

$$\tau_{neo-Alcator} = .166 n_e R^{2.04} a^{1.04} \kappa^{0.5} \tag{3.1}$$

This strong dependence on n_e and the lack of a dependence on I_p disagrees with the ITER89-P scaling observed elsewhere:

$$\tau_{ITER89-P} = .048 I_p^{0.85} R^{1.2} a^{0.3} \kappa^{0.5} n_e^{0.1} B_t^{0.2} amu^{0.5} P^{-0.5} \tag{3.2}$$

On C-Mod, the ITER89-P scaling appears to be holding for significantly shaped plasmas [28] adding confidence to its predictive qualities.

3.3.2 ICRF Heating

For many experiments on C-Mod, the 1 to 1.5 megawatts provided by ohmic heating is sufficient. However, auxiliary heating is normally required in order to study plasmas with temperatures greater than 1 keV. Most large tokamaks use neutral beams as their primary auxiliary heating scheme. However, the small ports and the long port extensions on C-Mod allows only perpendicular launch of neutral beams. In addition, the high plasma densities run on C-Mod make such beams impractical for most current experiments. For Electron Cyclotron Resonance Heating (ECRH), C-Mod would require sources above 140 GHz, but sources are not readily available.

Thus, Ion Cyclotron Resonance Heating (ICRH) is C-Mod's only auxiliary heating source[g]. ICRH has the advantage of rugged and efficient sources and transmission systems. The biggest challenge for ICRF heating is the limited surface power density at the antenna and the generation of impurities due to RF sheaths formed between the plasma and the antenna or between the wall and the antenna. Directly in front of the antenna the launched waves are evanescent. A thicker evanescent region will require larger fields at the antenna to couple a given power. The cutoff is located where:

$$N_{\|}^2 = 1 + \frac{\omega_{pe}^2}{\omega\omega_{ce}} - \frac{\omega_{pi}^2}{\omega(\omega + \omega_{ci})} \tag{3.3}$$

where $n_{\|} = \frac{ck_{\|}}{\omega}$. $k_{\|}$ is dictated by the geometry and phasing of the antennas. Substituting $\frac{\omega_{pi}^2}{\omega_{ci}} = \frac{\omega_{pe}^2}{\omega_{ce}}$ and solving for ω_{pi} gives:

$$\omega_{pi}^2 = (N_{\|}^2 - 1)(\omega_{ci} + \omega)\omega_{ci} \tag{3.4}$$

On C-Mod, $N_{\|} \approx 7$, $f = 80$ MHz, and $f_{ci} \approx 29$ MHz at the edge for a 5.3 tesla on axis plasma. So the cut-off density is at $n_e \approx 7 \times 10^{18}$ m^3. This lies on the outer edge of the SOL and is well below the lowest density monitored by the C-Mod reflectometer. During L-H transitions, the location of this layer can move enough to halve the loading on the antennas. Initially this posed a significant limitation on heating during H-mode operation. ICRF heating puts several other restrictions on plasma operation, in particular the choice of toroidal field, plasma shape, and plasma composition.

Figure 3-9 shows the four straps of the two ICRF antennas currently in the machine. Each antenna is capable of launching two megawatts at 80 MHz[h]. To date, the most successful heating results have been achieved at 5.3 tesla using a hydrogen minority in a deuterium plasma. Up to 3.5 MW have been coupled in with an antenna surface power density of 10 MW/m^2. Successful ion heating has also been achieved

[g]Lower hybrid heating and current drive are to be installed in 1997 or 1998.
[h]Sources tunable from 40 to 80 MHz are currently being installed.

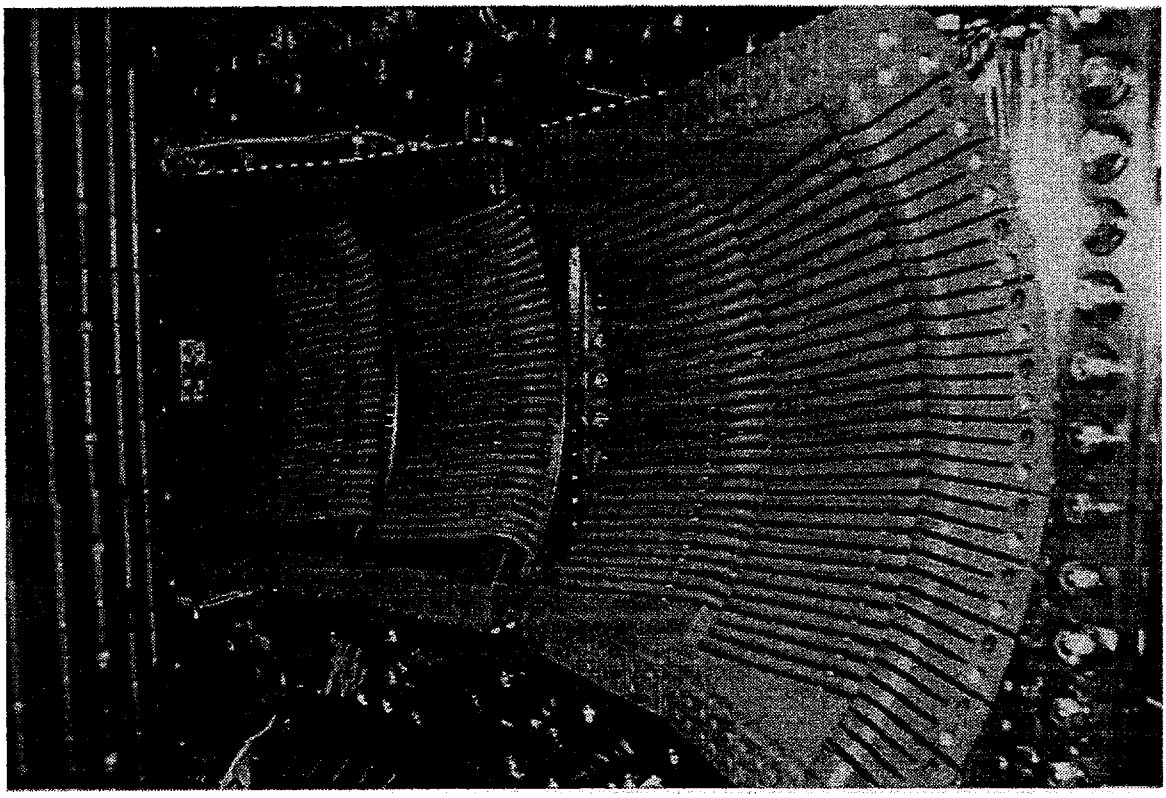

Figure 3-9: The Two ICRF Two Strap Antennas The tiles around the edge are for protection from the plasma. The bars rotated at 10° form a "Faraday Shield" that shorts out the electric field in front of the antennas. The curved shape of the antennas is intended to match the shape of the plasma to improve coupling.

at 7.9 tesla using a He^3 minority in a deuterium plasma. More will be said on the issues of coupling the ICRF to the plasma in § 7.2.1.

3.3.3 Divertor Operation

Alcator C-Mod has an advanced, "closed" divertor and usually operates with a single null at the bottom of the plasma, as shown in figures 3-5 and 3-6. Upper X-point and double null configurations are also possible for low input power shots. In the lower X-point configuration, the outer (right hand in Fig. 3-5) strike point can be positioned anywhere from the bottom of the divertor (slot configuration) to above probe 10 (flat plate configuration).

C-Mod is unique in that it uses a high Z metal, molybdenum, on all plasma facing

surfaces[i]. Most tokamaks use carbon. More than 8000 molybdenum tiles cover much of the inside of the C-Mod vacuum chamber. The small rectangles shown in Fig. 3-3 along the bottom, inner cylinder, and top of the vacuum vessel indicate the surfaces covered by tiles. The limiter between ports A and B and the two limiters on either side of port G are also covered by molybdenum tiles.

During L-mode operation, the density can be controlled well via gas puffing, unlike a carbon walled machine. After major disruptions, the next plasma attempt usually succeeds though a "fizzle" or short low current plasma may result instead. One fizzle usually conditions the walls sufficiently to obtain a plasma on the second attempt[j]. Both of these results are attributed to the molybdenum walls. Unfortunately, the radiated power in C-Mod prior to wall conditioning with boron is very high, often over 50%.

The C-Mod divertor has three modes of operation [20, 29]: sheath limited, high recycling, and detached. In the sheath limited regime, the electron temperature and pressure is conserved along a field line. In the high recycling regime, pressure is conserved on a field line, but temperature is not. And in the detached regime, both electron pressure and temperature are not conserved. Detachment has only been observed with electron temperatures of 6 eV or less.

3.3.4 Improved Confinement Modes

Both PEP and H-modes have been achieved in C-Mod. The PEP modes provided very peaked density profiles with central densities greater than 1.2×10^{21} m^{-3}. The thesis by Garnier [9] reviews the PEP results.

An excellent review of H-mode studies on C-Mod can be found in Greenwald [30, 31]. H-modes have been achieved on C-Mod in ohmic and ICRF heated plasmas but only in diverted operation[k]. Alcator C-Mod is normally run with the ion $\mathbf{B} \times \nabla \mathbf{B}$ drift

[i] A plasma facing surface is any spot on the machine that can be touched by hot plasma either during normal operation or during a disruption.

[j] The vacuum vessel walls can be further conditioned by electron cyclotron discharge cleaning, glow discharge cleaning, lithiumization via pellet injection, and boronization.

[k] Very little run time has been devoted to high power limited plasmas, so the ability to obtain limited H-modes is not precluded.

directed towards the divertor (down). This is the favorable direction for obtaining H-modes. A small number of H-modes has been achieved with the $\mathbf{B} \times \nabla \mathbf{B}$ drift in the opposite direction and required twice the power needed for obtaining H-mode with the favorably directed drift. This increased power threshold may be due to the reduced power delivered to the outer strike point in reversed field operation. This reduced power makes the outer strike point significantly colder and often detached. As a result the pumping effectiveness of the divertor is reduced. Typically, the compression ratio is half that achieved with the $\mathbf{B} \times \nabla \mathbf{B}$ drift down. However, main chamber pressures are within the range for which H-modes would be expected in normal operation.

The characteristics of the various manifestations of the H-mode in C-Mod and the variation with respect to surface conditions will be discussed further in § 7.

Chapter 4

Reflectometry Theory

In this chapter, a rather basic discussion of the theory of reflectometry will be presented. It should be noted that the understanding of the effect of fluctuations on the returned signal from a reflectometer is an area of continued research and is beyond the scope of this thesis. The interested reader is referred to the occasional IAEA meeting on reflectometry [32, 33] for the latest theories.

4.1 Dispersion Relations

Krall and Trivelpiece [34] derive the dispersion relations for an electromagnetic wave propagating in a cold, stationary, collisionless, homogeneous plasma. The derivation will be briefly outlined here using their notation. The magnetic field is chosen to be in the **z** direction and the wave is assumed to be traveling in the y-z plane at some angle θ relative to **B** (see Fig. 4-1). The perturbed quantities of the wave, $\mathbf{E_1}, \mathbf{B_1}, \mathbf{v_{i1}}$, and n_{i1}, are assumed to have a spatial and temporal form of:

$$\mathbf{E}_1(\mathbf{r},t) = \hat{\mathbf{E}}_1(\mathbf{k},\omega)\exp[i(\mathbf{k}\cdot\mathbf{r}-\omega t)]. \tag{4.1}$$

By applying Maxwell's equations, along with continuity and $m\frac{d\mathbf{v}}{dt} = q(\mathbf{E}+\mathbf{v}\times\mathbf{B})$, a matrix relation for the electric fields is derived. In the limit of frequencies far above

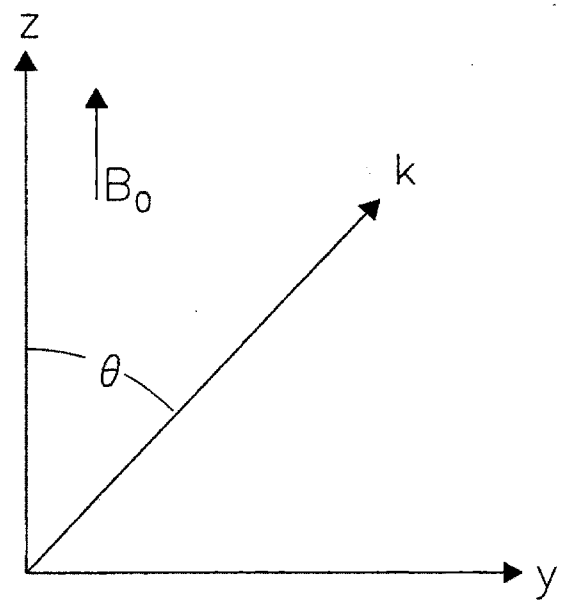

Figure 4-1: Coordinate System for Wave Propagation Derivation.

the ion cyclotron and ion plasma frequency, this matrix relation becomes:

$$\begin{bmatrix} 1-\frac{\epsilon_1}{N^2} & -\frac{i\epsilon_2}{N^2} & 0 \\ \frac{i\epsilon_2}{N^2} & \left(\cos^2\theta - \frac{\epsilon_1}{N^2}\right) & -\sin\theta\cos\theta \\ 0 & -\sin\theta\cos\theta & \sin^2\theta - \frac{\epsilon_3}{N^2} \end{bmatrix} \cdot \begin{bmatrix} \hat{E}_{1x} \\ \hat{E}_{1y} \\ \hat{E}_{1z} \end{bmatrix} = 0 \tag{4.2}$$

where

$$\epsilon_1 = 1 + \frac{\omega_{pe}^2}{\omega_{ce}^2 - \omega^2} \tag{4.3}$$

$$\epsilon_2 = \frac{\omega_{ce}}{\omega}\frac{\omega_{pe}^2}{\omega_{ce}^2 - \omega^2} \tag{4.4}$$

$$\epsilon_3 = 1 - \frac{\omega_{pe}^2}{\omega^2} \tag{4.5}$$

and $\omega_{pe} = \left(\frac{n_e e^2}{\epsilon_0 m_e}\right)^{\frac{1}{2}}$ = the electron plasma frequency, (4.6)

$\omega_{ce} = \frac{eB}{m}$ = the electron cyclotron frequency, (4.7)

and $N^2 = \frac{c^2k^2}{\omega^2}$ = the square of the index of refraction. (4.8)

For propagation perpendicular to the magnetic field, $\theta = 90°$, Eq. 4.2 reduces to:

$$\begin{bmatrix} 1-\frac{\epsilon_1}{N^2} & -\frac{i\epsilon_2}{N^2} & 0 \\ \frac{i\epsilon_2}{N^2} & -\frac{\epsilon_1}{N^2} & 0 \\ 0 & 0 & 1-\frac{\epsilon_3}{N^2} \end{bmatrix} \cdot \begin{bmatrix} \hat{E}_{1x} \\ \hat{E}_{1y} \\ \hat{E}_{1z} \end{bmatrix} = 0, \tag{4.9}$$

which has two roots corresponding to $\hat{\mathbf{E}}_1$ polarized perpendicular to or parallel to $\mathbf{B}_0$.

$$\text{For } \mathbf{E}_1 \parallel \mathbf{B}_0 \qquad N^2 = \frac{c^2k^2}{\omega^2} = 1 - \frac{\omega_{pe}^2}{\omega^2} \qquad \text{O-mode} \tag{4.10}$$

$$\text{and for } \mathbf{E}_1 \perp \mathbf{B}_0 \qquad N^2 = \frac{c^2k^2}{\omega^2} = 1 - \frac{\omega_{pe}^2}{\omega^2}\frac{\omega^2 - \omega_{pe}^2}{\omega^2 - \omega_h^2} \qquad \text{X-mode} \tag{4.11}$$

where $\omega_h = \left(\omega_{pe}^2 + \omega_{ce}^2\right)^{\frac{1}{2}}$ is the upper hybrid frequency[a]. These functions are plotted in Fig. 4-2. A wave can propagate where N^2 is positive and is evanescent where N^2 is negative. N^2 becomes infinite at a resonance and equals zero at a cutoff. The cutoffs are of particular interest for reflectometry. For waves propagating perpendicular to $\mathbf{B}_0$, N^2 equals zero when:

$$\omega = \omega_{pe} \qquad \text{for O-mode,} \tag{4.12}$$

$$\omega = \frac{\omega_{ce}}{2} + \left(\frac{\omega_{ce}^2}{4} + \omega_{pe}^2\right)^{\frac{1}{2}} = \omega_{RHC} \qquad \text{for X-mode,} \tag{4.13}$$

$$\text{or} \quad \omega = -\frac{\omega_{ce}}{2} + \left(\frac{\omega_{ce}^2}{4} + \omega_{pe}^2\right)^{\frac{1}{2}} = \omega_{LHC} \qquad \text{for X-mode.} \tag{4.14}$$

ω_{RHC} is the "Right Hand Cutoff" (RHC) and ω_{LHC} is the "Left Hand Cutoff" (LHC)[b]. The right and left moniker originates from solving Eq. 4.2 for $\mathbf{k} \parallel \mathbf{B}$ where the solutions are two circularly polarized waves with the same cutoff frequencies: ω_{RHC} and ω_{LHC}. For a generic C-Mod plasma, the cutoff frequencies are plotted in Fig. 4-3.

[a] X-mode is also known as E-mode.

[b] They are also referred to as the "Upper" and "Lower" cutoffs in some publications, ex. Hubbard [24].

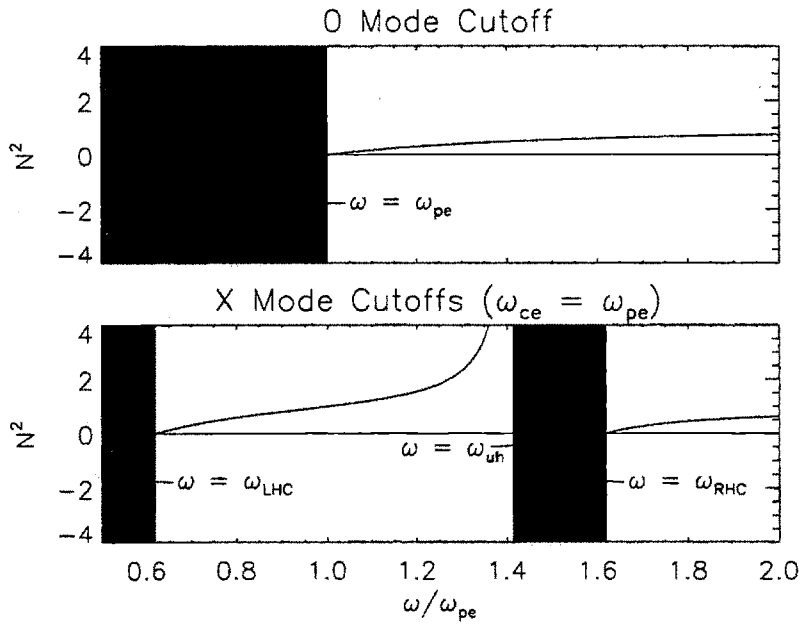

Figure 4-2: O and X Mode Reflection Above are plotted the dispersion relations for perpendicular propagation for the O and X mode for a cold plasma assuming stationary ions. In the shaded regions the waves are evanescent.

4.2 Accessibility in Toroidal Geometry

The first requirement for the application of the cutoffs discussed in § 4.1 to tokamak plasma diagnosis is determining where the plasma can be probed with a given frequency. To aid in this, the mapping of the cutoffs to major radius-density space will be presented. For the O-mode, this mapping is quite simple and is shown in Fig. 4-4. The cutoff frequency, f_{pe}, is proportional to the square root of the electron density and independent of B. The first intersection from the right of the density profile with each of the horizontal curves is where that particular frequency will reflect. For moderately hot plasmas, absorption at the first harmonic can prevent access to the cutoff. The total magnetic field in a tokamak falls off approximately as 1/r for low β plasmas giving the hyperbolic curve where $f_{ce} = f_{pe}$. Low field launched O-mode waves can not pass this curve. For example, 125 GHz launched from the low field side would not reach the cutoff for the density profile shown, as the resonance at 0.8 meters will absorb the launched wave. Frequencies below 105 GHz should be unaffected, as the

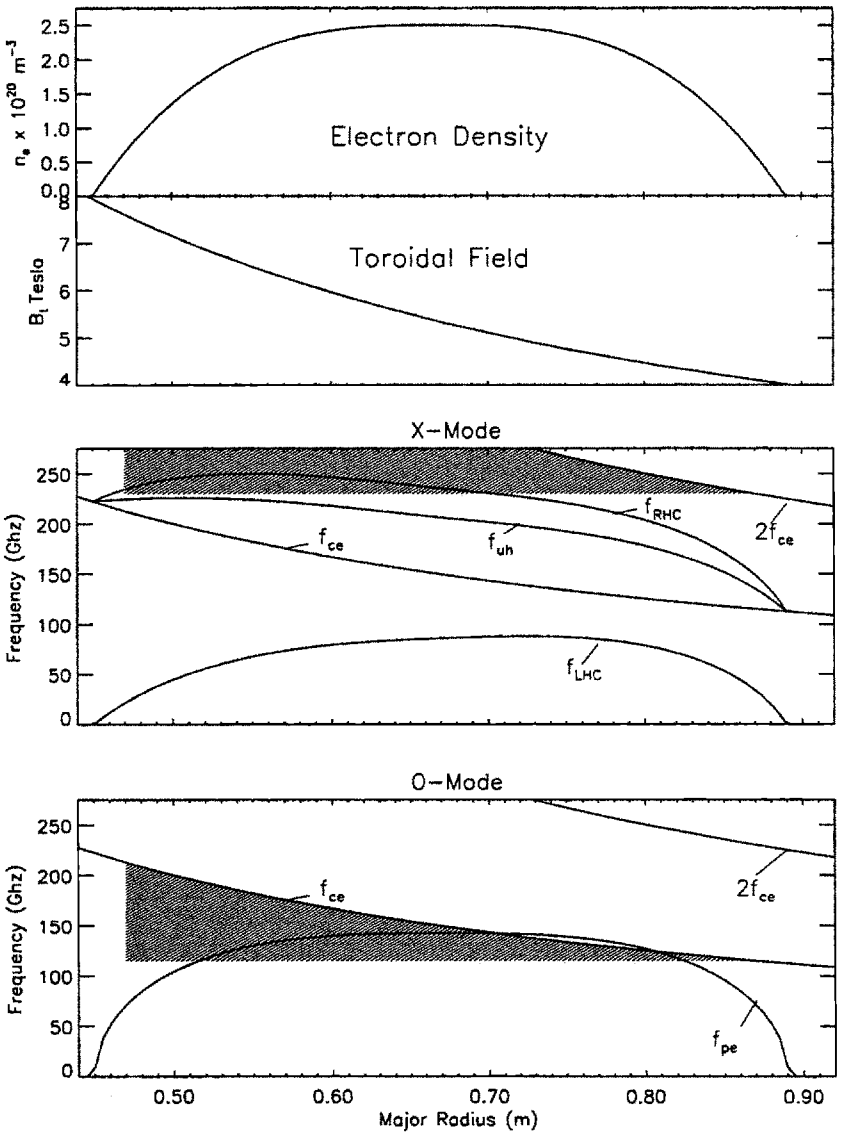

Figure 4-3: Cutoff Frequencies for a 5.3 Tesla Plasma The shaded regions are inaccessible to low field launch due to electron cyclotron absorption. The second harmonic for O-mode and the first harmonic for X-mode are generally not optically thick.

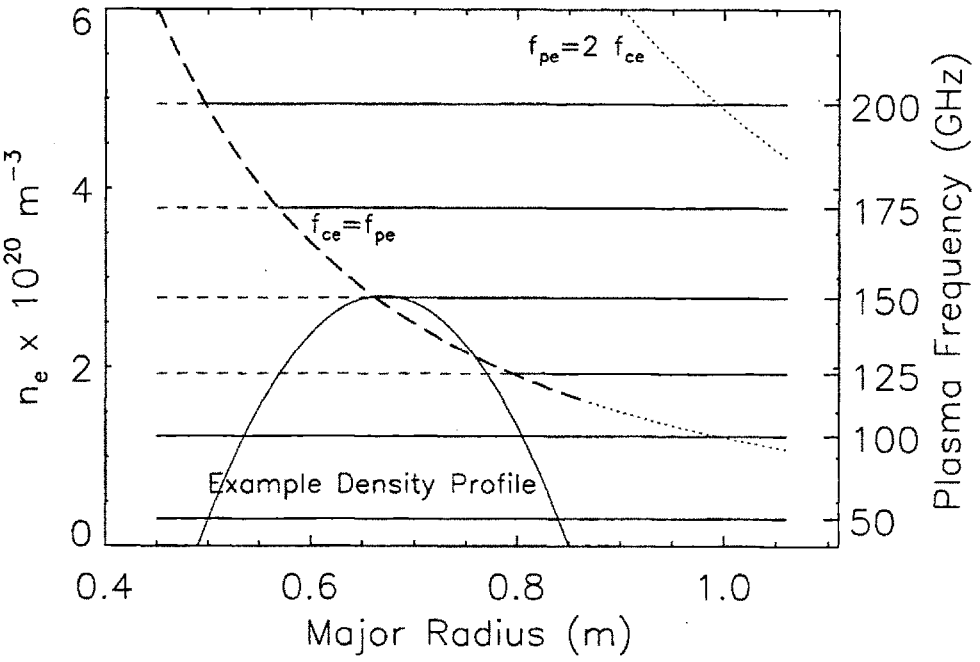

Figure 4-4: O-Mode Accessibility Plot for 5.3 Tesla An example density profile is included. On C-Mod the inner wall is at 0.44 meters and the limiters are at .905 meters. Typically the LCFS is at .89 meters and the plasma magnetic axis is at .68 meters.

edge plasma is too cold and tenuous at the location of their cyclotron resonance to have a significant optical depth.

The O-mode case is simple compared with the X-mode case shown in Fig. 4-5. Here the curve $f_{ce} = f_{pe}$ is included along with the right hand axis from Fig. 4-4, so O and X mode access can be compared. Equation 4.13 can be solved for $f_{pe,crit}$ as a function of launched frequency, f, and radius, r:

$$f^2_{pe,crit}(f,r) = \left(f - \frac{f_{ce}(r)}{2}\right)^2 - \frac{f^2_{ce}(r)}{4} \tag{4.15}$$

Then, using $B(r) = B_0\frac{r_0}{r}$ and Eq. 4.6, n_{crit} as a function of r can be specified. The curves labeled on the right of Fig. 4-5 correspond to the critical densities for the RHC from 120 to 300 GHz. Above about 210 MHz, absorption at $f = 2f_{ce}$ becomes important. Substituting this condition into Eq. 4.15 gives the curve $f_{pe} = \sqrt{2}f_{ce}$ on which the access curves from 240 to 300 terminate. The ECE diagnostics observe

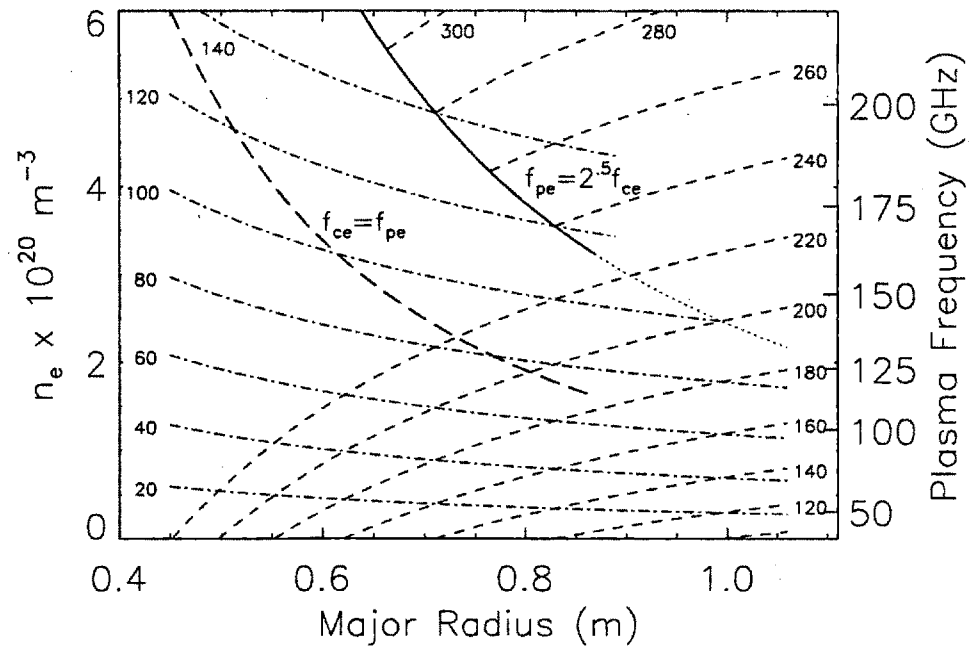

Figure 4-5: Accessibility Plot for 5.3 Tesla The values 20 to 140 on the left correspond to the curves demarking the critical densities for 20 to 140 GHz for the LHC. The numbers 120 to 300 on the right do the same for frequencies 120 to 140 GHz for the RHC.

emission in this range of frequencies. A density profile that cuts through these curves will cut off the ECE emission, giving a potentially very accurate density measurement at the expense of a temperature measurement.

The curves labeled at the left of Fig. 4-5 correspond to the LHC. Using the same analysis in Eq. 4.14 results in:

$$f^2_{pe,crit}(r) = \left(f + \frac{f_{ce}(r)}{2}\right)^2 + \frac{f^2_{ce}(r)}{4}. \tag{4.16}$$

In order to be launched from the low field side of the tokamak and reach the LHC, the launched wave must at some point pass through the RHC/upper hybrid resonance pair. This can be seen in Fig. 4-2. In a tokamak diagnostic, the plasma density near the horns is low and gets higher as the launched waves approach the plasma center. On Fig. 4-2 this corresponds to moving from right to left. If the density is zero where $f = f_{ce}$, then the resonance and the cutoff are in the same place and the launched

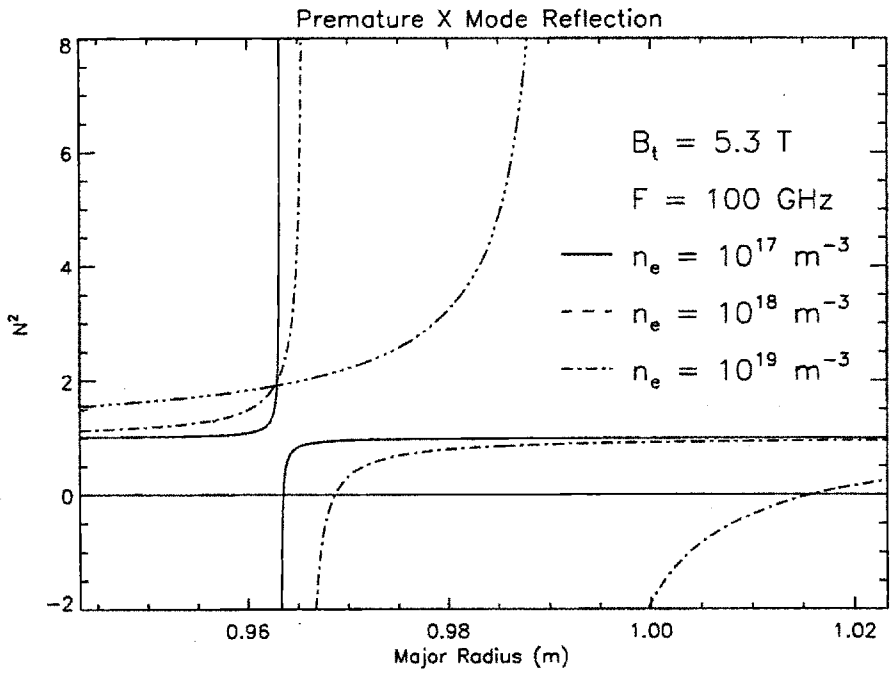

Figure 4-6: Right Hand Cutoff and Upper Hybrid Resonance for 100 GHz. Note that once the separation between he cutoff and the resonance is greater than a few free space wavelengths, virtually no signal passes through.

wave will pass through unimpeded. If the density is increased, the separation of the resonance and the cutoff will grow. If the separation distance becomes on the order of a wavelength, little power will be coupled through. For C-Mod at 5.3 tesla, 90 GHz and below should be unaffected, however frequencies above 90 GHz may reflect off the RHC well outside of the main plasma. Figure 4-6 shows the separation between the upper hybrid resonance and RHC for 100 GHz[c]. The toroidal field ripple reduces B_t by 10% relative to a $1/R$ scaling at the radius of the launching horns, further increasing this problem[d]. If high field launch were feasible on C-Mod, frequencies above 110 GHz would encounter the cyclotron frequency at $f_{pe} = \sqrt{2} f_{ce}$. However, for a thermal electron distribution, the optical depth for the first harmonic in X-mode is small, so significant absorption should not be expected. Two important features to note from Fig. 4-5 are that for low field launch, only the RHC allows one to

[c]Currently the plasma behind the radius of the antennas is poorly diagnosed. Whether the plasma density is 10^{16} or 10^{18} m^{-3} in this region is completely unknown.

[d]The ripple at the LCFS, however, is less than 1%.

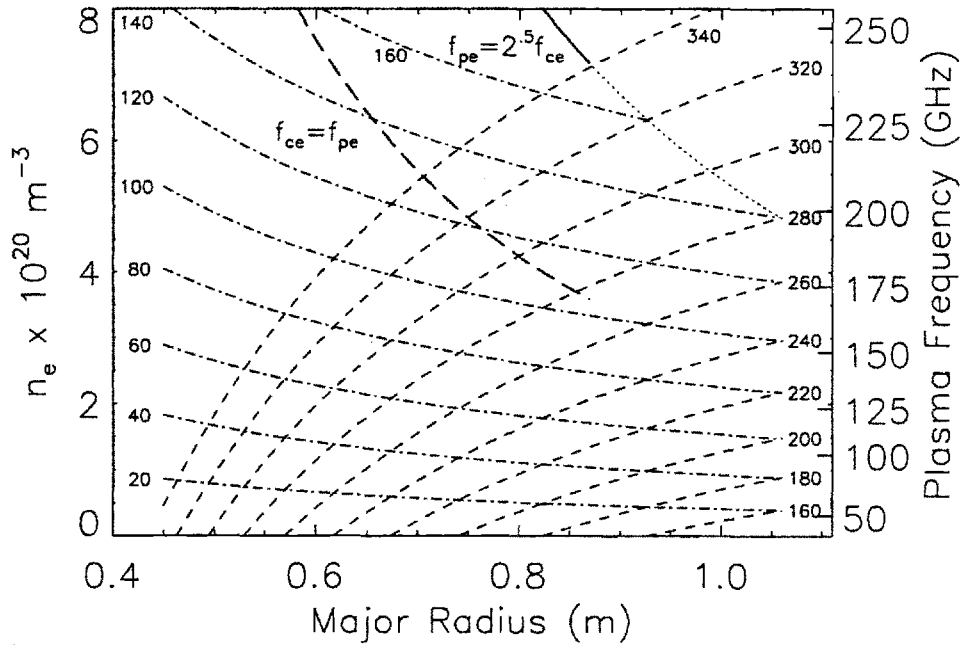

Figure 4-7: Accessibility Plot for 7.9 Tesla (see Fig. 4-5 for labeling scheme.

study hollow profiles, while the LHC allows one to study a given density with a lower frequency using generally less expensive sources and detectors. Figure 4-7 shows the same accessibility plot for 7.9 tesla. At this field, frequencies above 140 GHz will suffer the same access problems in reaching the LHC as was discussed for frequencies above 90 GHz at 5.3 tesla.

4.3 Wave Propagation in a Stratified Medium

In this section the propagation of O-mode waves through an inhomogeneous medium will be discussed. Much of the material, including the notation, is extracted from Ginzberg [35] chapter 4. The particular condition to be discussed is $\mathbf{k} \parallel \nabla \mathbf{n_e}$, $\mathbf{k} \perp \mathbf{B_0}$, and, of course, $\mathbf{E_1} \parallel \mathbf{B_0}$. The wave equation for these conditions is:

$$\frac{d^2 \hat{E}_{1z}(y)}{dy^2} + \frac{\omega^2}{c^2} \epsilon(\omega, y) \hat{E}_{1z}(y) = 0. \tag{4.17}$$

For clarity and to make the author's life easier, E will be substituted for $\hat{E}_{1z}(y)$ for the remainder of this section. First, a linear density profile for which the wave equation can be solved exactly will be presented. Equation 4.17 has the same form as the time independent Schroedinger Equation[e]:

$$\frac{d^2\psi}{dy^2} + \frac{2m}{\hbar^2}\left(E - V(y)\right)\psi = 0. \tag{4.18}$$

The WKB method commonly used to solve Eq. 4.18 will be discussed and finally an "Abel like" inversion of reflectometer data to give density profiles will be presented.

4.3.1 Exact Solution for Linear Density Profile

For O-mode propagation perpendicular to the magnetic field with a linear density profile, an exact solution can be obtained. Inserting

$$n_e(z) = n_c\frac{y}{y_1}, \qquad n(y_1) = n_c = \text{the critical density for } \omega, \text{ and } \epsilon = 1 - \frac{y}{y_1}.$$

into Eq. 4.17 and making the substitution:

$$\zeta = \left(\frac{\omega^2}{c^2 y_1}\right)^{1/3}(y_1 - y) \;=\; \left(\frac{\omega}{c}y_1\right)^{2/3}\epsilon(y), \tag{4.19}$$

reduces Eq. 4.17 to:

$$\frac{d^2E}{d\zeta^2} + \zeta E = 0. \tag{4.20}$$

Equation 4.20 has solutions of the form of Bessel functions with the boundary condition that $E \to 0$ as $y \to \infty$ (or $\zeta \to -\infty$).

$$E(\zeta) = A\zeta^{1/2}\left(J_{1/3}\left(\frac{2}{3}\zeta^{3/2}\right) + J_{-1/3}\left(\frac{2}{3}\zeta^{3/2}\right)\right) \qquad \text{for } \zeta > 0 \tag{4.21}$$

$$E(\zeta) = A(-\zeta)^{1/2}\left(-I_{1/3}\left(\frac{2}{3}(-\zeta)^{3/2}\right) + I_{-1/3}\left(\frac{2}{3}(-\zeta)^{3/2}\right)\right) \qquad \text{for } \zeta < 0, \tag{4.22}$$

[e]All those classes amount to one line in my thesis!

or the Airy integral:

$$E(\zeta) = \frac{3A}{\pi} \int_0^\infty \cos\left(\frac{x^3}{3} - \zeta x\right) dx. \tag{4.23}$$

For $\zeta \gg 1$, i.e. for y many wavelengths from the reflecting layer, Eq. 4.23 reduces to:

$$E(\zeta) \approx \frac{3A}{\sqrt{\pi}} \zeta^{-1/4} \cos\left(\frac{2}{3}\zeta^{3/2} - \frac{\pi}{4}\right) \tag{4.24}$$

The fields calculated here are for a standing wave with one wave travelling in and one travelling out. This can be seen most clearly by including the time dependent portion of E. The real portion of the electric field, $\xi'(\zeta, t)$, is simply:

$$\xi'(\zeta, t) = E\cos[\omega(t - t_0)] \tag{4.25}$$

$$\approx \frac{3A}{2\pi\zeta^{1/4}} \left\{ \cos\left[\left(\frac{2}{3}\zeta^{3/2} - \frac{\pi}{4}\right) - \omega(t - t_0)\right] + \cos\left[\left(\frac{2}{3}\zeta^{3/2} - \frac{\pi}{4}\right) + \omega(t - t_0)\right] \right\} \tag{4.26}$$

The first term on the right corresponds to a wave moving in the $+\zeta$ or $-y$ direction. The term on the left is a wave moving in the $-\zeta$ or $+y$ direction. With a little algebra, a portion of the argument of the cosines above can be written in a very suggestive form:

$$\frac{2}{3}\zeta^{3/2} - \frac{\pi}{4} = \left[\frac{2\omega}{3\omega y_1^{1/2}}\right](y_1 - y)^{3/2} - \frac{\pi}{4} \tag{4.27}$$

$$= \left[\frac{-\omega}{c y_1^{1/2}}\right] \int_{y_1}^{y} (y_1 - y')^{1/2} dy' - \frac{\pi}{4} \tag{4.28}$$

$$= \frac{\omega}{c} \int_y^{y_1} N(y') dy' - \frac{\pi}{4} \tag{4.29}$$

$$= \int_y^{y_1} k(y') dy' - \frac{\pi}{4}. \tag{4.30}$$

Now choosing t_0 so that the phase of the wave going in the positive y direction at some point y'' is zero at $t = 0$, we get:

$$\xi(y'',t) = K\cos\left(\omega t - \left[\frac{4\pi}{\lambda_0}\int_{y''}^{y_1} N(y')dy' - \frac{\pi}{2}\right]\right) + K\cos(\omega t), \tag{4.31}$$

where:

$$K = \frac{3A}{2\sqrt{\pi}\zeta^{1/4}} = \frac{3A}{2\left(\frac{2\pi^4 y_1}{\lambda_0}\right)^{1/6} N^{\frac{1}{2}}(y'')} \quad \text{and,} \quad \lambda_0 = \frac{2\pi c}{\omega} \tag{4.32}$$

So the phase difference between the launched and reflected waves for a linear profile equals the integral of the local index of refraction along the path travelled by the wave times $\frac{2\pi}{\lambda_0}$ minus a $\frac{\pi}{2}$ correction.

4.3.2 The W.K.B. Method

Key to the application of reflectometry is the approximation of "Geometrical Optics" or the "W.K.B. method"[f]. The approximation of geometrical optics is that the wavelength of E.M. radiation at a given location can be determined by the local index of refraction. Also, the power reflected from a gradient in the index is small. Again Ginzberg [35] gives a rigorous derivation of the approximation of geometrical optics. Dicke and Wittke [37] do the same for the quantum mechanical analog. The derivation will not be repeated here other than to say a function of the form:

$$E(y) = E_0(y)e^{-i\frac{\omega}{c}\psi(y)} \quad \text{and} \quad \psi(y) = \pm\int_{y_0}^{y} N(y)dy \tag{4.33}$$

[f] It should be noted that while Wentzel, Kramers and Brillouin each independently in 1926 and Jeffreys in 1924 applied this technique to wave mechanics, Gans used them to study radio waves in the ionosphere in 1915 and Lord Rayleigh used them to study sound waves in 1912 [36]. The value of working in a popular field is evident.

is inserted into Eq. 4.17 and ordered in terms of $\frac{\omega}{c}$. $E_0(y)$ is assumed to vary slowly with respect to λ and y_0 is an arbitrary constant. After some algebra the result,

$$E(y) = \frac{C_+}{N^{\frac{1}{2}}(y)} e^{+i\frac{\omega}{c}\int_{y0+}^{y} N(y)dy} + \frac{C_-}{N^{\frac{1}{2}}(y)} e^{-i\frac{\omega}{c}\int_{y0-}^{y} N(y)dy}, \tag{4.34}$$

is found, where the + and − represent waves propagating in the $+y$ and $-y$ directions. This approximate solution holds provided:

$$\frac{\lambda_0}{2\pi}\frac{\left|\frac{dN}{dy}\right|}{N^2} \ll 1. \tag{4.35}$$

The W.K.B. approximations fail near a reflection. The phase for a linear profile has been calculated above. If the profile is assumed to be linear near the reflecting layer, a correction of $-\frac{\pi}{4}$ to the phase is applied. Multiplying the total phase shift by two for propagation into and out of the plasma, we get:

$$\phi(f) = \frac{2\omega}{c}\int_{R_c(f)}^{a} N(y)dy - \frac{\pi}{2}. \tag{4.36}$$

The steepest density gradient expected in the main C-Mod plasma will occur in the SGR of an ELM free H-mode. The expected lower limit for the scrape off length, l_{SOL}, in the SGR is the ion banana orbit width $\sim$ 2mm. Assuming $n_e = n_c \exp(-y/.002)$ where n_c is the critical density for f. For an exponential density profile relation 4.35 reduces to:

$$\frac{\lambda_0}{2\pi l_{SOL}} \ll N = \sqrt{1 - \frac{n_e(x)}{n_c(f)}} \tag{4.37}$$

For wavelengths from .6 to .27 cm (50 to 110 GHz) and assuming $l_{SOL} \sim .002$ meters, WKB theory holds for $\frac{n_e}{n_c} \lesssim 0.7$. This is not a problem as long as the gradient continues to the critical density. However, if the profile has a kink in it as shown in Fig. 4-8, a significant reflection can occur at the steep gradient.

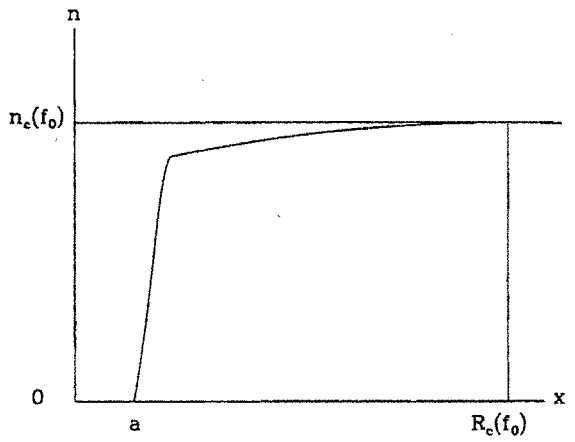

Figure 4-8: Profile Kink

4.3.3 Profile Inversion

For O-Mode, the phase of the returned wave is:

$$\phi(f) = \frac{4\pi}{c} \int_{R_c(f)}^{a} \left(f^2 - f_{pe}^2(x)\right)^{\frac{1}{2}} dx - \frac{\pi}{2} \tag{4.38}$$

As an electron density profile diagnostic, the desired term is $R_c(f)$. Some algebra allows its extraction from eq 4.38. Divide both sides by $\frac{4\pi}{c}$ and take the derivative with respect to f to get:

$$\frac{c}{4\pi}\frac{d\phi}{df} = -\frac{dR_c(f)}{df}\left(f^2 - f_{pe}^2(R_c(f))\right)^{\frac{1}{2}} + \int_{R_c(f)}^{a} \frac{f}{\left(f^2 - f_{pe}^2(x)\right)^{\frac{1}{2}}} dx \tag{4.39}$$

Now, $f_{pe}(R_c(f)) = f$(the plasma frequency at the critical radius of the frequency f is f) so the first term on the right hand side of the above equation is zero provided the density gradient is nonzero. The next few steps effectively perform an Abel inversion.

Multiply both sides by $(f_0 - f^2)^{-\frac{1}{2}}$ and integrate over f from 0 to f_0:

$$\int_0^{f_0} \frac{c}{4\pi}\frac{d\phi}{df}\frac{df}{(f_0^2 - f^2)^{\frac{1}{2}}} = \int_0^{f_0}\left(\int_{R_c(f)}^{a}\frac{f\,dx}{(f^2 - f_{pe}^2)^{\frac{1}{2}}}\right)\frac{df}{(f_0^2 - f^2)^{\frac{1}{2}}}. \tag{4.40}$$

Now switch the order of integration (We will revisit this step in a § 4.3.4.):

$$= \int_{R_c(f_0)}^{a}\int_{f_{pe}(x)}^{f_0}\frac{f\,df\,dx}{(f^2 - f_{pe}^2(x))^{\frac{1}{2}}(f_0^2 - f^2)^{\frac{1}{2}}} \tag{4.41}$$

$$= \int_{R_c(f_0)}^{a}\int_{u=0}^{(f_0^2 - f_{pe}^2(x))^{\frac{1}{2}}}\frac{du\,dx}{(f_0^2 - u^2 - f_{pe}^2(x))^{\frac{1}{2}}} \tag{4.42}$$

where $u = (f^2 - f_{pe}^2(x))^{\frac{1}{2}}$,

$$\int_0^{f_0}\frac{c}{4\pi}\frac{d\phi}{df}\frac{df}{(f_0^2 - f^2)^{\frac{1}{2}}} = \int_{R_c(f_0)}^{a}\frac{\pi}{2}dx \tag{4.43}$$

$$= (a - R_c(f_0))\frac{\pi}{2}. \tag{4.44}$$

Dividing both sides by $-\frac{\pi}{2}$ and adding a gives:

$$R_c(f_0) = a - \int_0^{f_0}\frac{c}{2\pi^2}\frac{d\phi}{df}\frac{df}{(f_0^2 - f^2)^{\frac{1}{2}}}. \tag{4.45}$$

So determining the radius, $R_c(f_0)$ where the plasma frequency equals the launched frequency f_0 requires knowing the term $\frac{d\phi}{df}$ for all f between 0 and f_0. At first this appears to be a daunting task, however it should be pointed out that the integrand strongly weights the the value of $\frac{d\phi}{df}$ near the cutoff over those at lower frequencies. As a consequence, reasonable profiles can be obtained using far less than the complete knowledge of the group delay from 0 to f_0.

4.3.4 Hollow Profiles

One problem with the derivation above is dealing with hollow density profiles such as the one shown in Fig. 4-9. Here f_j sees past the hollow profile, while f_i reflects

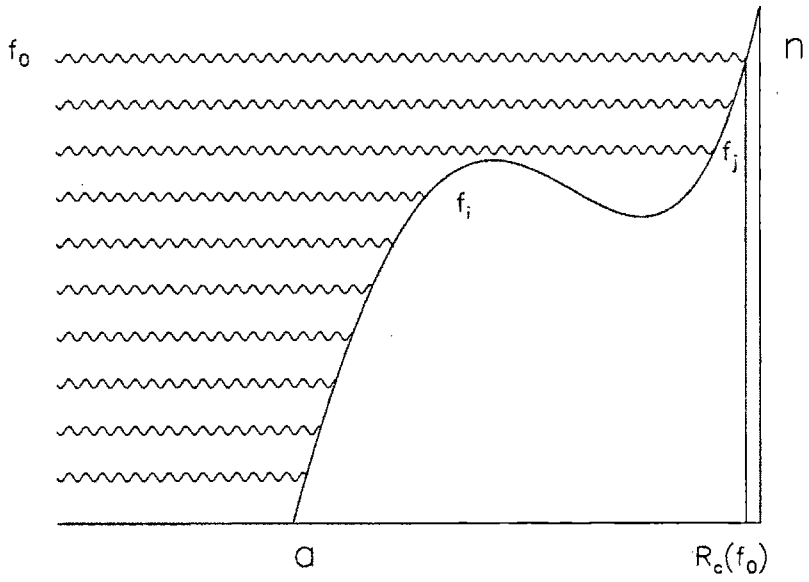

Figure 4-9: Hollow Profile Inversion Problems

before the hollow portion. The group delay observed by f_j does not contain enough information to reconstruct the profile of the hollow region. In the derivation above, the problem arises in going from Eq. 4.40 to Eq. 4.41 by switching the order of integration. This is only allowed if f and R_c are one to one. Figure 4-10 plots $R_c(f)$ and shows the difference in the two regions of integration. The horizontal lines in the left hand figure are the paths for the first integration in Eq. 4.40 which omit a portion of the hollow region. The figure on the right hand side shows the integration region for Eq. 4.41. The first integration follows the vertical paths shown. The result of a hollow profile will be an underestimation of the distance from "a" to the reflecting layer. While it may appear possible to reconstruct some of the hollowness for the particular case shown through an iterative approach and some smoothing procedure, in practice, the noise in each measurement and the fluctuation in the density at the local maximum and minimum between the cutoffs for f_i and f_j, make such analysis impractical.

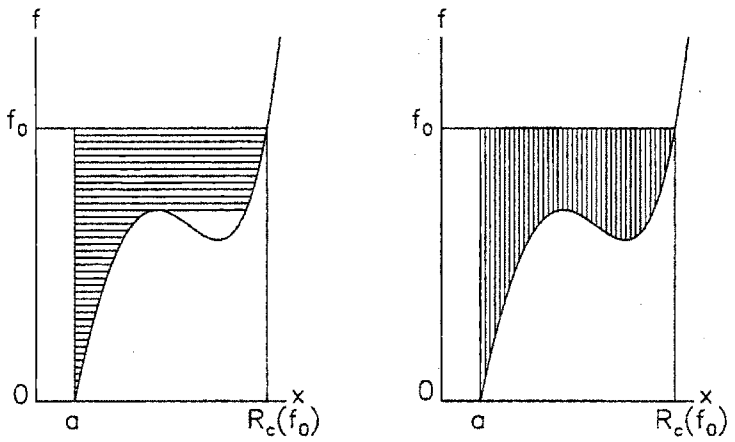

Figure 4-10: Integration Paths

4.4 Plasma Absorption and Emission

Hutchinson [38] derives the optical depth τ for single pass for the O-mode at an arbitrary angle. For the specific case of perpendicular propagation his result reduces to:

$$\tau = \frac{L\alpha}{\omega_{ce}} \quad \text{where,} \quad \alpha = \frac{\pi}{2c}\omega_{pe}^2 \left(1 - \frac{\omega_{pe}^2}{\omega_{ce}^2}\right)^{1/2} \left(\frac{T_e}{m_e c^2}\right) \quad \text{and} \quad L = \frac{\omega_{ce}}{\left|\frac{d\omega_{ce}}{ds}\right|} = R \tag{4.46}$$

where R is machine major radius. The cyclotron resonance for 110 GHz is at 90 cm for 5.3 Tesla operation. This is typically in the SOL with $n_e \leq 10^{20}$ m^{-3} and $T_e \leq 100$ eV giving a maximum optical depth of .3 for a single pass or .6 for a return path. This has not appeared to adversely affect operation. For the rest of the frequencies used the cyclotron resonance is well outside the main plasma. When operating at lower field absorption has limited access.

Emission of radiation in the frequency bands used can be an issue. If the plasma

density is low enough, runaway electrons can be present[g]. The runaways are very relativistic, thus reducing their emission frequency by the ratio of their rest mass to their relativistic mass. So the reflectometer can observe emission from these electrons despite the nominal cyclotron resonance being much higher. Large bursts of emission can often be seen often coinciding with sawtooth crashes. The bursts could be due to runaway electrons being kicked out of the center of the plasma where their emission was cutoff or having some of their parallel momentum converted to perpendicular momentum by the sawtooth crash, again causing their emission to be seen. Previous work on Alcator C has demonstrated the existence of a cyclotron maser [39] effect. On one occasion, a C-Mod reflectometer mixer failed during a shot with a high runaway population. High plasma emission or X-rays from fast electrons hitting machine walls are assumed to be the cause. Reflectometers on other machines have experienced failures due to unknown causes [40, 41]. Emission from runaways may be the culprit.

4.5 Relativistic Effects

Binslev [42] has worked out relativistic corrections to the cutoffs for reflectometry. For a given O-mode reflectometer frequency, the relativistic cutoff density, $n_{e\,\mathrm{rel}}$, will be slightly higher than the density, $n_{e\,\mathrm{cold}}$, calculated from cold plasma theory. For temperatures below 20 keV the correction factor to five significant digits is:

$$\left(\frac{n_{e\,\mathrm{rel}}}{n_{e\,\mathrm{cold}}}\right) = \nu_O \approx 1 + 4.892 \times 10^{-3}\left(\frac{T_e}{keV}\right) - 2.24 \times 10^{-6}\left(\frac{T_e}{keV}\right)^2 + 2.3 \times 10^{-8}\left(\frac{T_e}{keV}\right)^3 \quad (4.47)$$

[g]The collision frequency between particles in a plasma drops as their velocity increases. Runaways are electrons that have been accelerated by the ohmic current drive to velocities where the drag due to collisions is small compared to the accelerating potential. Such electrons can reach energies in the 10's of MeV's.

and the relativistic index of refraction N_O is

$$N_o \approx \left(1 - \frac{f_{pe}^2}{\nu_O f^2}\right)^{\frac{1}{2}} \tag{4.48}$$

For almost all our current operating conditions, T_e is less than 4 keV, giving $\nu_O \leq 1.02$. This is small compared to the other errors in our measurements, however this could become an issue in the future as heating power and confinement times increase. In particular, cross calibration of the Thomson Scattering system based on reflectometer cutoff (see § 6.4.4) should not be attempted on ICRF heated shots.

Chapter 5

The Alcator C-Mod Reflectometer

In this chapter the hardware and rf techniques used for the C-Mod Reflectometer will be described.

5.1 Design Philosophy

At the time this project was being developed, reflectometry had met with limited success [43, 24, 44, 45, 46, 47]. In order to apply Eq. 4.45, most experiments required that the phase of the returned signal be monitored as the launched frequency was swept over either a broad or narrow range. If at any point the returned signal disappeared or gained too much noise, the $d\phi$ term would pick up a modulo 2π error. The difficulty in following the phase of the returned wave over the long periods of the source sweep would compromise these diagnostics.

Hubbard, Prentice, and Sips from the Joint European Tokamak (JET) provided much useful advice on the specific difficulties they encountered with their reflectometer. Two issues that had been particularly challenging to the JET group were combining multiple frequency bands into one transmission and receiving line, and dealing with the complicated mode structure of their long, overmoded transmission line with multiple bends. C-Mod has the good fortune of comparatively easy access to the machine, and few of the radiation shielding requirements of the JET program. The diagnostic at A-port was arranged so that few bends in the waveguide runs

would be needed, and so it would not be necessary to be greatly overmoded. Also, each waveguide band was given a separate pair of horns. Additionally, this diagnostic was considered an experimental diagnostic subject to major reconfiguration. Further, connectorized components built to designated specifications for all rf circuit boards operating at more than 30 MHz were purchased, allowing the designers/builders of this diagnostic to expend and develop their expertise elsewhere.

5.2 Differential Phase or AM Reflectometry

Sufficient progress has been made in reflectometry so that it can now be proposed as a core electron density diagnostic for fusion research plasmas [48]. Key to this progress has been the development of alternative modulation techniques. "Differential Phase" (DP) or "Amplitude Modulated" (AM) reflectometry has become a common diagnostic technique [49, 50, 51, 52, 53]. This approach was first suggested by Rich Chedester of Millitech Corporation. It was first proposed as a plasma diagnostic on C-Mod in 1990 [54].

Figure 5-1 shows the fundamental idea behind DP reflectometry. Instead of measuring the change in phase as one sweeps the frequency, one launches two closely spaced frequencies and measures the phase difference of the returned waves.

$$\begin{aligned} &\text{Launched signal:} && \sin[2\pi(F+\Delta F)t] && +\sin[2\pi(F-\Delta F)t] \\ &\text{Received signal:} && \sin[2\pi(F+\Delta F)t-\phi_1] && +\sin[2\pi(F-\Delta F)t-\phi_2] \end{aligned}$$

$$\phi(f) = \frac{4\pi}{c}\int_{R_c(f)}^{a}\left(f^2 - f_{pe}(x)^2\right)^{\frac{1}{2}}dx - \frac{\pi}{2} \tag{5.1}$$

In the detector the two signals are mixed and the low frequency term is:

$$\sin[2\pi(F+\Delta F)t-\phi_1-(2\pi(F-\Delta F)t-\phi_2)] = \sin[4\pi\Delta Ft-\Delta\phi]$$

$$\text{where,} \qquad \Delta\phi = \phi_1 - \phi_2$$

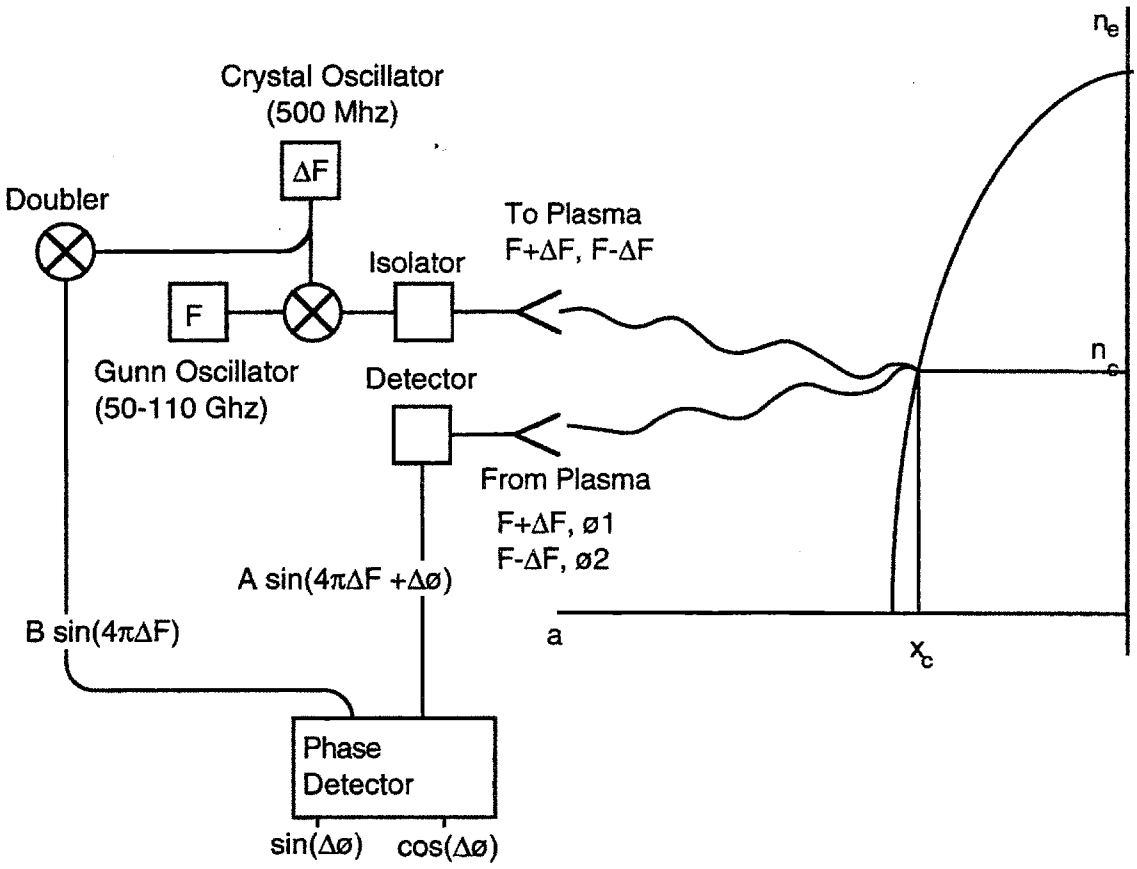

Figure 5-1: AM Technique $\Delta\phi = \phi_1 - \phi_2$

The group delay for the beat wave to travel to the reflecting layer and back is:

$$\tau_g = \frac{\Delta\phi}{4\pi\Delta F}. \tag{5.2}$$

As long as $\Delta F \ll F$ and the density profile does not have a major break in slope at $n_e = n_c(F)$, then τ_g is independent of ΔF. Then ΔF can be chosen such that the expected range of $\Delta\phi$ is less than 2π so there is no $\frac{n}{\Delta F}$ ambiguity in τ_g. For example, if the group delay from the launching horns to the critical layer can range from 1 to 2 ns (corresponding to an optical path from 30 to 60 cm), then $\Delta F \leq 500$MHz. Higher frequencies will give better phase resolution provided the separation distance between the two reflecting layers is small relative to the turbulence corelation length.

Another popular approach to making profile measurements with reflectometry is to use an electronically swept oscillator and monitor the returned phase or returned

frequency as the source is swept over either a narrow (100 MHz to 1 GHz) or broad (one waveguide band) range. The advantages and disadvantages of a fixed-frequency, multi-channel DP reflectometer as developed for C-Mod compared to such swept systems are:

Advantages:

- **No frequency modulation needed.** This reduces some of the complexity of the system.
- **No $2n\pi$ ambiguity in the returned phase.** By choosing ΔF small enough, as discussed above, temporary loss of signal due to plasma turbulence does not result in an ambiguity in the returned phase. Systems that depend on following the phase of the returned signal during a frequency sweep can "lose fringes".
- **Time response dictated by output filtering rather than sweep rate.** The integration time over which a measurement is made can be made as short or as long as desired.
- **Simplified transmission system.** The performance of a fixed frequency DP reflectometer is completely independent of the mode structure of the transmission line provided the isolation between the launching line and the receiving line is high. In a swept system, multiple reflections in the transmission lines must kept small or somehow calibrated out.
- **No reference leg is needed.** A swept system requires a reference arm. This can be a major or minor detail depending on the distance from the source to the launching antennas and the modulation technique.
- **Automatic frequency stabilization.** All drifts in the millimeter wave oscillators are mixed out in a DP reflectometer receiver. The phase information is carried on the $2\Delta F$ beat wave which can be provided by a very stable crystal oscillator.

Disadvantages:

- **Sensitive to multiple reflections.** Multiple reflections in the vacuum chamber during plasma operation or during calibration will corrupt signals in a DP reflectometer. A fast swept system can in principle distinguish between reflections from the plasma and multiple reflections inside the chamber. To accomplish this the launched frequency must be swept fast enough so that the expected returned frequency offset range is large compared to the broadening expected from fluctuations, and the expected range of returned frequencies from a plasma reflection must not overlap the range for multiple reflections.

- **More complicated fluctuation analysis.** The returned fluctuation signal from a DP reflectometer will be the product of the scattering of the two launched frequencies. To date, high frequency data have been of little application other than stating that the plasma is turbulent or quiescent. For analysis of frequency and **k** spectra a single sideband of the reflectometer should be used.

- **Limited number of data points.** For each data point of a DP reflectometer, a source and a receiver is needed. A swept system is limited only by the integration time needed per data point and the required sweep rate.

5.3 Choice of Frequencies and Polarization

The original goal of the reflectometer was to provide edge profiles to aid in the inversion of the interferometer chord-integrated density measurements. Before operating the machine, the expected plasma density profiles were parabolic with central densities of 1 to $2 \times 10^{20}\mathrm{m}^{-3}$. The separatrix density was predicted to be 2 to $5 \times 10^{19}\mathrm{m}^{-3}$.

The toroidal field on C-Mod is largely dictated by the ICRF heating scheme desired. The most successful heating scheme has been achieved using deuterium with a hydrogen minority at 5.3 Tesla. This puts the RHC out of reach (see Fig. 4-2). The LHC cutoff had not been used before for reflectometry. In order to get to the lower cutoff, the launched waves must pass the O-mode cutoff. Any power coupled into the O-mode by not matching the field pitch properly would be reflected. As this

reflecting layer may be much closer to the horn than to the lower X-mode cutoff, the measurements could be corrupted. To avoid these issues, this diagnostic operated in the O-mode. With the expected density range, frequencies between 50 and 110 GHz fit both the expected densities and financial restrictions.

The actual profiles have proven to be flatter than parabolic in L-mode and separatrix densities are about twice the expected values. In addition much of the current operation is in H-mode where separatrix densities generally exceed 1.5×10^{20} m^{-3}. Tests using X-mode are planned for Spring 1997 (see § 8.3.3).

5.4 Transmitters and Receivers

The diagnostic was built with 50 and 60 GHz in WR-15, 75 and 88 in WR-12, and 110 in WR-8 waveguides. The sources were purchased with the intention of also trying a narrow band sweep system, and trying several receiver arrangements for the DP technique. The 50, 75, and 88 GHz oscillators all have 1 GHz of veractor tuning and 2 GHz of mechanical tuning. The 110 GHz oscillators have somewhat less mechanical tuning. The 60 GHz oscillators were salvaged from the Tara interferometer and have very limited tuning capabilities. In retrospect, the wide tunability of most of the oscillators proved more of a complication than an asset as the frequency stability of the oscillators is somewhat compromised at the expense of tunability. Oscillators occasionally drifted beyond their operating band due to thermal variations during the run and possibly due to mechanical vibrations. Were the author to rebuild this diagnostic from scratch, thermally stabilized oscillators with 400 MHz[a] of mechanical tuning would be purchased. Figure 5-2 shows a schematic of the transmitter and receiver for the 50 GHz channel. Signal from the transmitting Gunn oscillator is upconverted, then passed through an isolator, and finally combined with the 60 GHz signal in a standard 3 dB directional coupler. After the coupler, the waveguide is tapered up to WR-42 for the ten foot run to the vacuum feedthrough. The upconvertor generates the first upper and lower sidebands while the fundamental sideband and all the other

[a]to allow for various modulation frequencies to be used

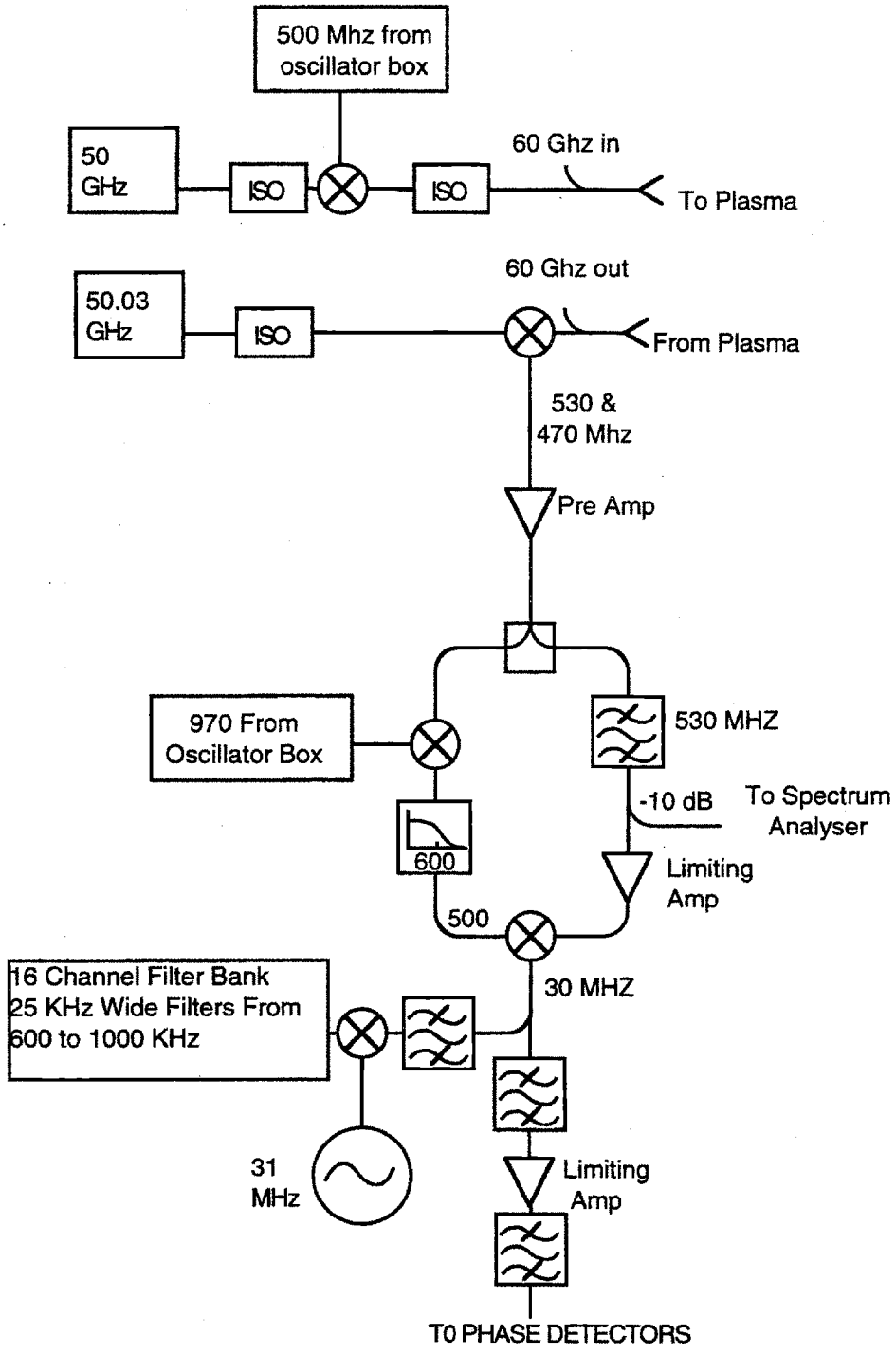

Figure 5-2: Receiver Details

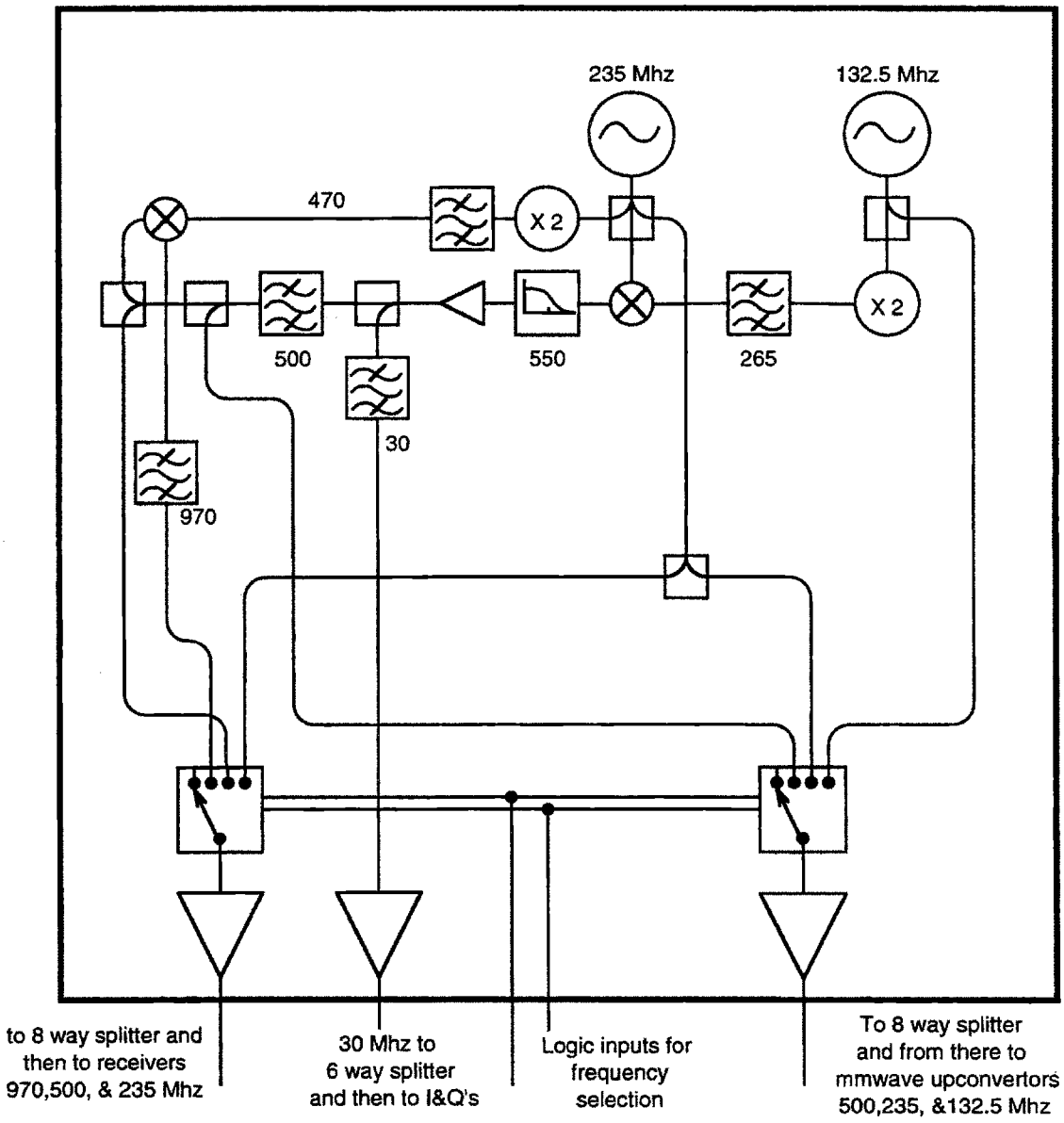

Figure 5-3: RF Source Box The source box shown above allows the user to select three frequencies (500, 235, and 132.5) to be sent to the upconvertors. The frequency choice can be made via CAMAC either between shots or during a shot.

sidebands are suppressed by 20dB relative to the two transmitted sidebands. Two 18 dB isolators are needed to prevent pulling of the oscillator frequency by changes in the power reflected by the plasma.

Experiments on JET [55] showed very rapid ($\sim 1\mu$s) 30 dB changes in the signal amplitude returned from the plasma. For the C-Mod reflectometer, the two returned sidebands, which can each vary by 30 dB, needed to be mixed. To mix the two returned sidebands without introducing large variations in the conversion loss, one sideband is passed through a limiting amp[b] giving a constant 10 dBm output which is put into the LO of a mixer. The other sideband, after being mixed with 970 MHz, is then mixed with the limited signal producing a 30 MHz signal carrying the group delay measurement. Since only one sideband has been limited, the power can still vary greatly. Before making a final phase measurement, the signal is limited again, then sent to the phase detectors. This system has a dynamic range of 50 dB with a phase variation of less than five degrees.

The bandwidth of the input to the limiting amp should be equal to the bandwidth of the filters on the output of the phase detectors in order for the quadrature sum of the phase detector outputs to remain constant. For this reason, when profile information was the primary interest, 2 KHz wide crystal filters centered about 30 MHz were placed before the 30 MHz limiting amp. This eliminated the possibility of studying fluctuations on that particular channel. Typically, this filter was used in all but the 88 GHz channel. Figure 5-4 shows the amplitude of the quadrature sum of the two outputs with and without the crystal filter.

Three different upconversion frequencies can be generated for the transmitter and receiver discussed above. When operating with the very narrow bandpass filters described above, the difference frequency between doubled upconversion frequency and the downconversion frequency must be good to a few hundred hertz. This narrow bandpass was not planned for when ordering the 970 and 500 MHz oscillators. These oscillators could not be tuned enough to bring them within the filter band-

[b]A limiting amp is an amplifier designed to run in saturation. The output power (typically 10 dBm) is independent of the input power. These amps serve the same purpose as automatic gain control (AGC) amps. A limiting amp typically settles faster but is noisier than an AGC amp.

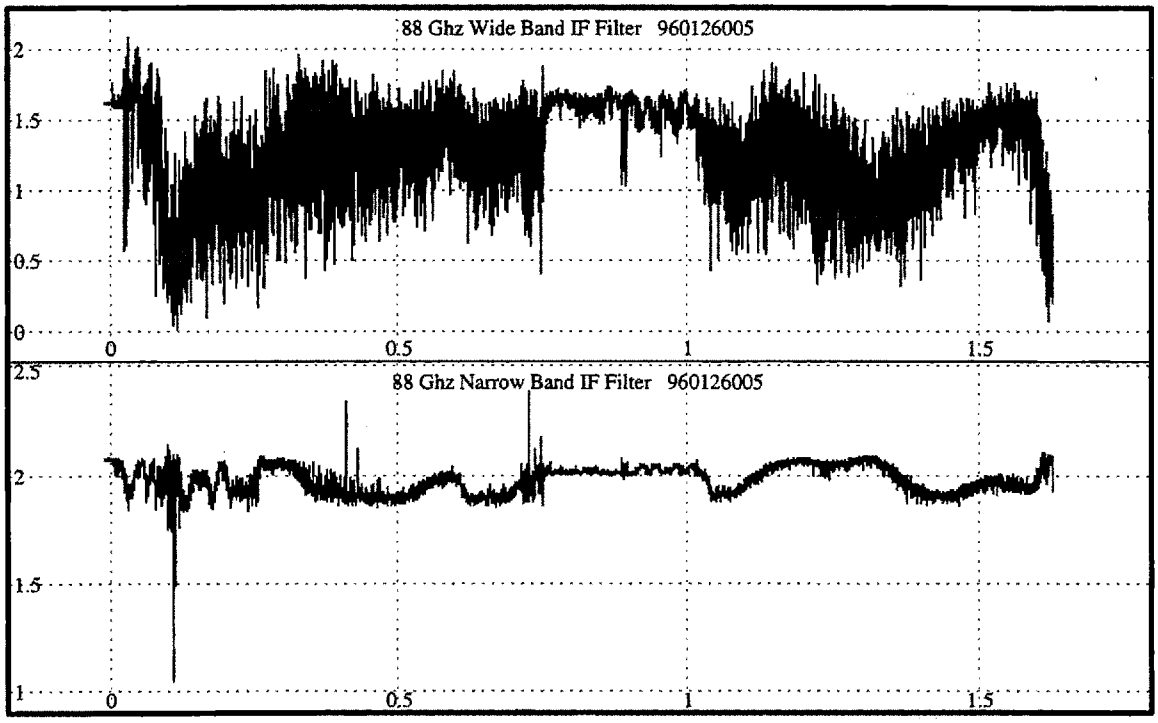

Figure 5-4: Effect of Crystal IF Filter. Both of the traces above are the quadrature sum of the outputs from the phase detectors using a 2 KHz low pass filter. The upper trace has a 2 MHz wide filter before the limiting amp; the lower trace has a 2 KHz wide filter before the limiting amp. During the period between .75 and 1.0 seconds the plasma is in H-Mode.

pass. Figure 5-3 shows the resulting RF source box. This design is somewhat more complicated than originally planned, however, the setup as shown worked fine. When operating with the 235 MHz upconversion frequency, the difference frequency between the Gunns is 295 MHz, and with 132.5 MHz, the difference frequency is 397.5 MHz. For all data shown in this thesis, the 500 MHz upconversion frequency was used as it provides the highest spatial resolution.

Not shown in Fig. 5-2 are digitally selectable bias voltages for the Gunn oscillators. In principle, the modulation frequency could be changed during a shot. This capability has not been pursued to date but could be useful in attempting to make radial correlation measurements.

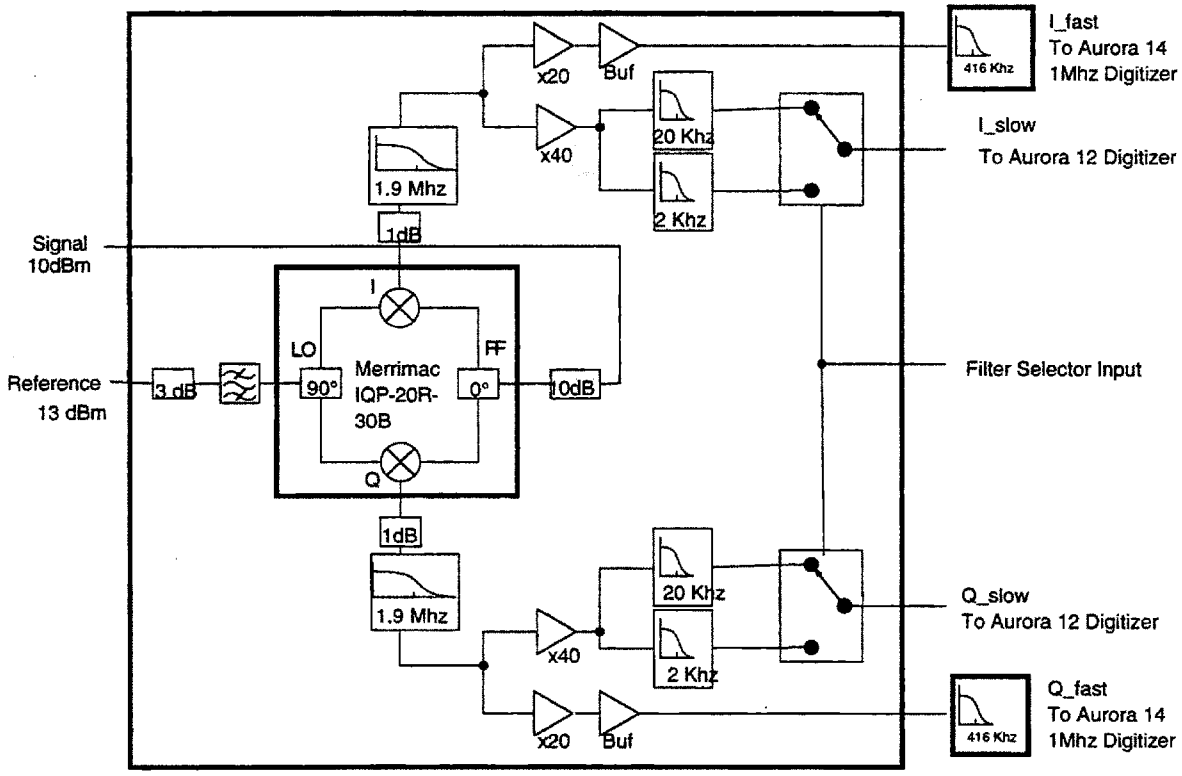

Figure 5-5: I/Q Schematic

5.5 Phase Detectors

The phase detectors are I/Q modules (cosine and sine detectors) with digitally selectable filters. Figure 5-5 is a block diagram of the device. The core of the device is an I/Q chip manufactured by Merrimac. It operates with a 30 MHz LO and a 27 to 33 MHz RF. The harmonics produced by this chip were isolated from the rest of the circuit by the filters and pads before and after the chip. Signals intended for profile studies were low pass filtered using the 2 or 20 KHz filters. These are active 8 pole Bessel low filters based on the Maxim 'MAX274ACNG'[c] filter chip. They are intended to avoid aliasing when digitizing at 5 and 50 KHz respectively. The Aurora A12 [d] digitizers can take 8192 samples per channel. At 5 KHz, 1.64 seconds of data can be obtained, which is longer than most shots currently run on C-Mod. The 416

[c]I found these to be quite useful chips. Each chip has four sections with a two pole filter provided by each section. Filter characteristics are specified by three precision resistors on each section. Software for choosing the resistors is also available.

[d]Now manufactured by Jorway.

KHz filter is a passive 12 pole Chebychev filter manufactured by K&L that eliminates aliasing when digitizing at 1 MHz. Aurora A14 digitizers were used for fluctuation measurements. They provided for 130 ms of data per shot. Multiple gates allowed this 130 ms to be distributed in multiple windows throughout the shot.

However, with the crystal filter in front of the limiting amp, operation was restricted to only the lowest frequency low pass filter.

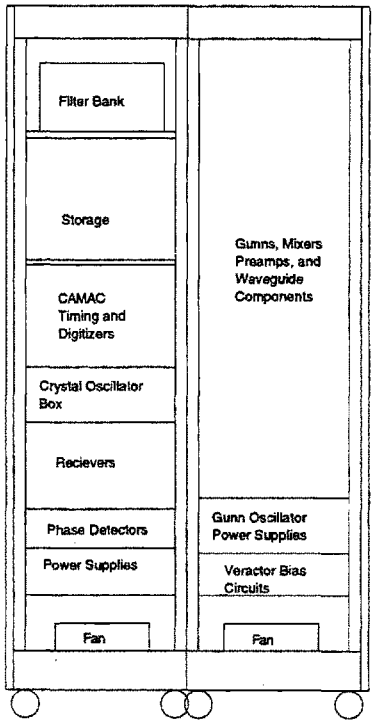

Figure 5-6: Equipment Rack Above is the equipment rack where all reflectometer electronics are housed. The many cables used in this device are not shown for clarity.

5.6 Waveguides, Windows and Horns

5.6.1 Waveguides

Access to the C-Mod vacuum chamber is rather restricted, so all electronics are located in a rack about ten feet from the vacuum flange. This distance also helps

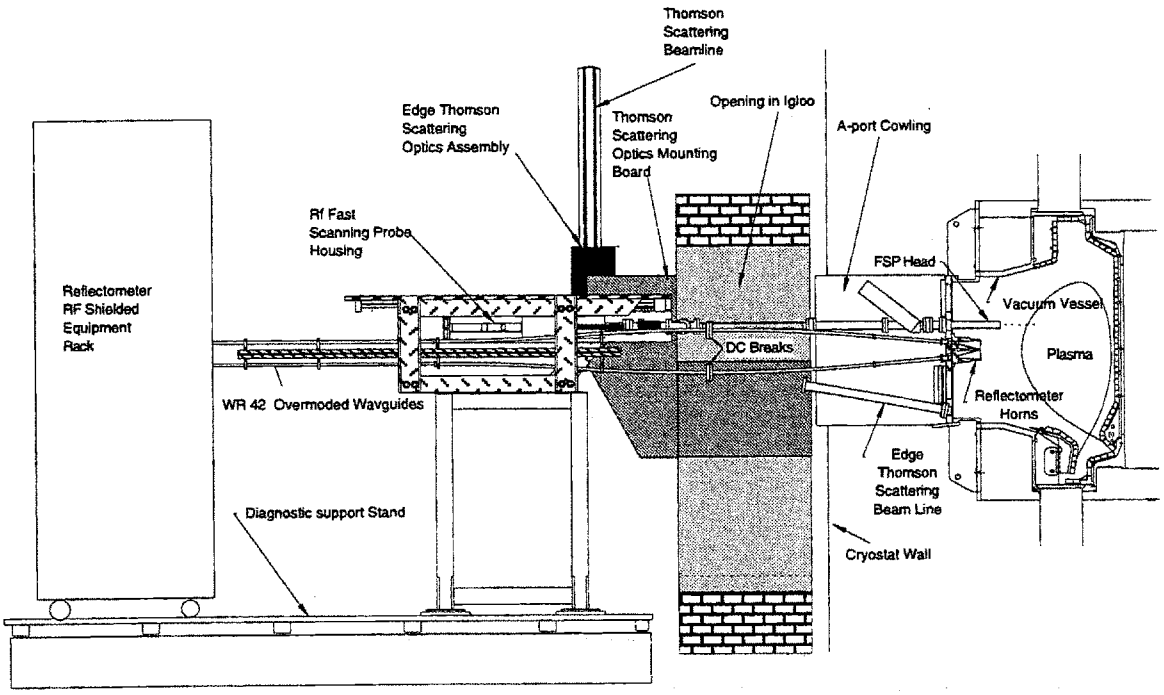

Figure 5-7: A-Port Side View Also in this port, though not shown, are two cameras and several other spectroscopic diagnostics. Spectrometers for the Edge Thomson Scattering are located to the left of the reflectometer rack.

reduce the flux of X-rays and neutrons on microwave components.[e] This waveguide run required tapering up to overmoded waveguide. WR-42 was used because it reduced the attenuation to an acceptable level and would not carry many modes other than the desired TE_{10}. In addition, WR-42 is the largest standard size waveguide that can easily pass through a 1.33" "Conflat" vacuum window. A larger waveguide would have greatly complicated the vacuum feedthroughs. With a very gradual bend the waveguide could be oriented to match the angles of the horns without tapering down again. For a continuous small perturbation to an overmoded waveguide, the conversion to other modes is small unless the two modes are phase matched [56].

[e]Data on radiation damage to millimeter wave components is unavailable. There has been a degradation over time of either sources or mixers. It is not clear if this is due to aging, operator error, or radiation damage.

5.6.2 Windows

The windows used for all but the 110 GHz system were 0.015" thick pieces of mica clamped between two O-rings: One sitting in a groove milled in a mini-Conflat (1.33") flange and the other in a groove milled in the flange of a short section of waveguide. While this configuration did produce a very low loss (> 0.5 dB), wide band vacuum feedthrough, the manufacture and installation of these feedthroughs was difficult due to the limited space on the surface of a mini-Conflat and the propensity of the mica to cleave when stressed nonuniformly. Because of these difficulties, standard glass mini-Conflat windows were used for the 110 GHz system. These resulted in a 1.5 dB loss for each window[f]. Specially milled gaskets hold the window end of the vacuum waveguide in place.

5.6.3 Horns

The Alcator C-Mod vacuum chamber is a uniquely hostile environment for conducting structures. A major issue for the design of the microwave horns was withstanding the torques induced in the horns during a plasma disruption. Elongated plasmas are vertically unstable. During a shot, the plasma is stabilized by feeding back on the current in the EF coils, particularly EFC (see Fig. 3-1). In the event of a failure in the feedback system, the plasma may move vertically 10 cm in one millisecond [57]. The resulting change in the radial flux through structures at the midplane drives currents that, when coupled with the toroidal field, induce a surprisingly high torque about the vertical axis [58]. All vacuum components were designed to withstand a vertical disruption of a 3 MA plasma at 9 Tesla with the plasma center at 75 cm and an upward velocity of 10 cm per millisecond. This was the most dangerous plasma being considered before Alcator was commissioned. Currently, "halo" currents flowing through the inner cylinder during disruptions limit operations to 1.5 MA[g] and 7.9 Tesla [59].

[f] In general returned signal amplitude was more than sufficient so a 3 dB loss from the windows did not compromise operation.

[g] Actually the limit was raised from 1.2 MA in August 1996. Only one shot so far has had 1.5 MA.

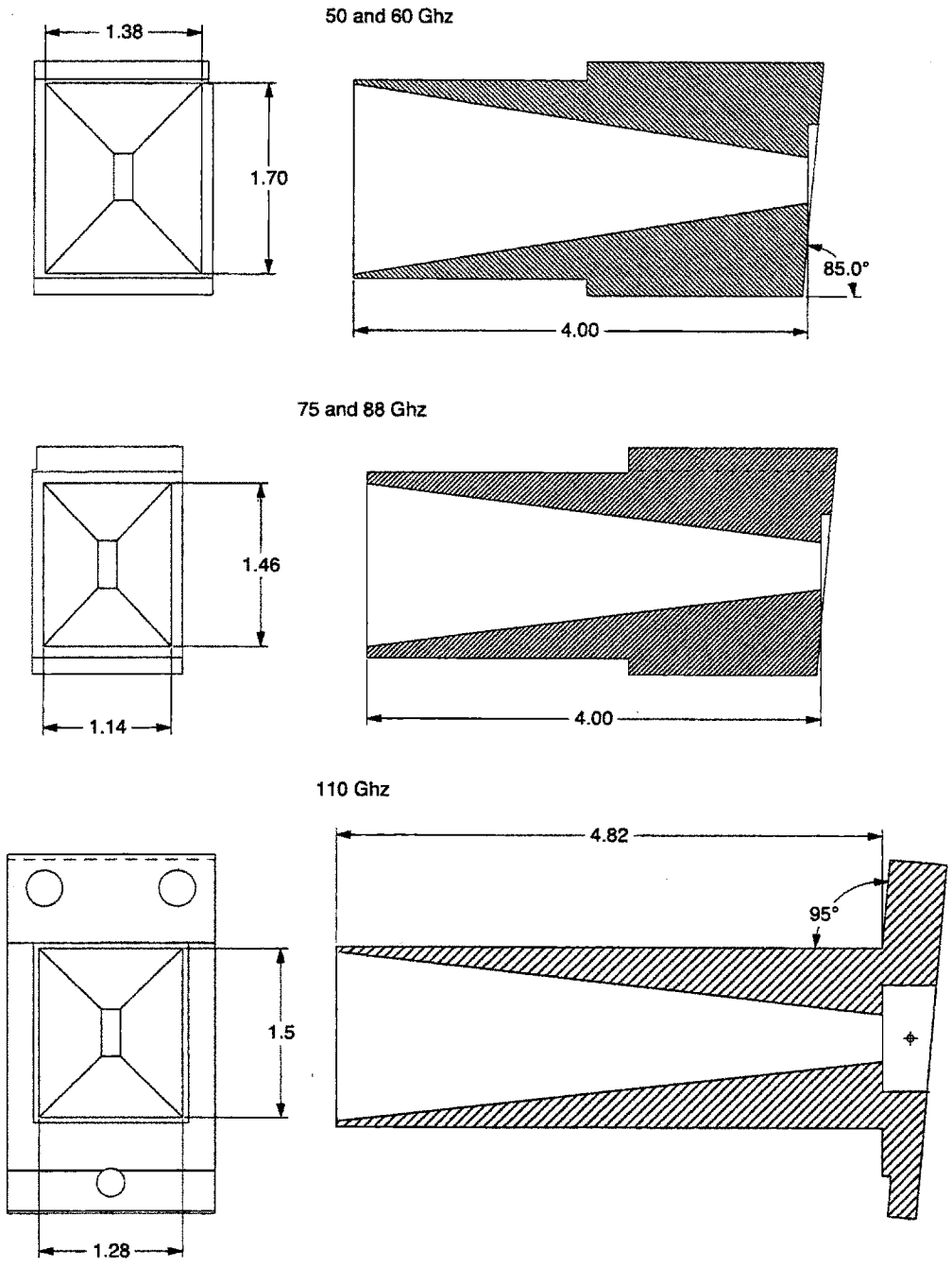

Figure 5-8: Horn Antennas Above are shown cross sections of the horn antennas mounted inside the C-Mod vacuum vessel.

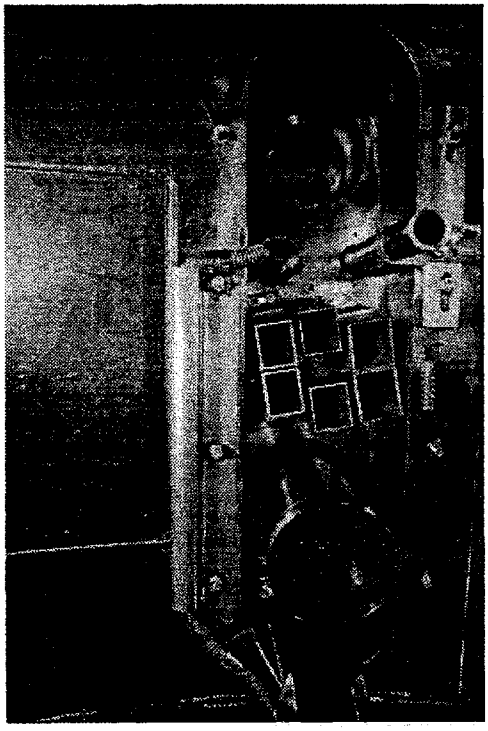

Figure 5-9: Horns in Machine This will be a photo looking radially outward of the horns. Note that they are rotated ten degrees to match the field pitch at the plasma edge and that they are pointing towards the midplane so that their beam patterns overlap.

In addition, ferromagnetic material near the plasma can greatly disrupt operations by perturbing the magnetic field symmetry and preventing the initial plasma breakdown. Standard microwave horns of electroformed nickel or copper are not suitable for use on C-Mod due to their high conductivity along with nickel's feromagnetism. Instead, C-Mod's horns were constructed by electric discharge machining (EDM) pyramidal holes in solid steel blocks. The width of the horns was dictated by the size of the horizontal port allocated to the reflectometer. Originally, 20 to 88 GHz horns were chosen. However, the 20 GHz horns were later replaced by horns for 110 GHz once it became clear that the edge densities were higher than expected.

The six horns are mounted on a reentrant flange at the midplane on A-port (see Fig. 5-7 and Fig. 3-2). The ends of the horns are at the major radius of the inside of the outer cylinder of the vacuum vessel. The three upper horns are pointed down at

5 degrees and the lower horns are pointed up at 5 degrees so that their beam patterns overlap at about 80 cm. The horns are rotated clockwise as seen by looking radially in ten degrees[h] to match the expected field line pitch. The angle of the field at the edge changes depending on the current, plasma shape, and toroidal field. Ten degrees was chosen because the faraday shields of the ICRF antennas are set at this angle so edge field pitch was expected to match this. (note: this was how I made that choice. I should probably come up with some discussion of what this angle should be in retrospect. It is not all together clear where the two modes separate with a sheared field and a density gradient.)

5.7 Data Aquisition and Data Analysis

Scientists and students working on C-Mod have the luxury of using the MDS+ [60] data aquisition system[i]. This provides a very simple to use, menu-driven interface between the CAMAC based data aquisition system and the user.

A 1 MHz clock is supplied to all diagnostics over an optical fiber. This clock is then divided down in a "decoder" module to provide slower digitization rates. Encoded in the clock is a start "event" four seconds before the anticipated initiation of the plasma. MDS+ then calculates time bases for each signal. This central timing system ensures that all digitizers use the same clock so that the timing of events seen on different diagnostics can be reliably compared.

After a shot, data from all diagnostics are transferred over a fiber optic data highway to a magnetic storage disk. Typically, within a few minutes of a shot, data from all diagnostics are available to all users on the C-Mod cluster of workstations. After a day's run, all data are archived in an optical disk "jukebox". All data from all shots on C-Mod are available automatically in a few minutes. Shots that have been accessed recently are stored on magnetic disk and are available within seconds.

Data are processed on Digital Alpha workstations using the IDL interpretive pro-

[h] B_T and I_p are always parallel.

[i] Replete with two computer scientists, Tom Fredian and Josh Stillerman, to whom the author is greatly indebted

graming language. Processed data are stored on the same magnetic and optical disks used for raw data.

Chapter 6

Profile Reconstruction

In this chapter, the steps involved in determining density profiles from the raw data from the five reflectometer channels are described in detail. The resulting profiles are compared with other diagnostics including the fast scanning probe, the grating polychromator, Thomson scattering, and the two color interferometer. Along the way, some of the common phenomena seen by the reflectometer will be presented. In addition, the perturbation to the SOL by the fast scanning probe will be documented and a couple of plausible models for this perturbation suggested.

6.1 Inversion Algorithm

In § 4.3.3, the location of the critical layer, $R_c(f_0)$, for a given frequency, f_0, was calculated from group delay measurements for an O-mode reflectometer via a simple integration:

$$R_c(f_0) = a - \int_0^{f_0} \frac{c}{2\pi^2} \frac{d\phi(f)}{df} \frac{df}{(f_0^2 - f^2)^{\frac{1}{2}}} \,. \tag{4.45}$$

The integral above requires knowledge of $\frac{d\phi}{df}$ for all f between 0 and f_0. For any practical reflectometer, the number of data points is limited and some interpolation scheme is needed. For a broad band swept system the number of data points is dictated by sweep rate and signal to noise ratio. For a fixed frequency or narrow

band swept system, however, the number of data points is dictated by the number of channels available. As a result, the number of data points measured in a profile is much smaller with a fixed frequency system. However, since no sweeping is required, the time response can be much higher. On C-Mod, the term $\frac{d\phi}{df}$ is measured for up to five different frequencies. Between measured frequencies, $\frac{d\phi}{df}$ is linearly interpolated with respect to f^{2a}. The density is assumed to be zero outside of the limiter radius and linear between the limiter and the first data point. This will be discussed further in § 6.3. The integral in Eq. 4.45 is approximated by the sum of 1 GHz wide bins:

$$R_c(f_0) = a - \frac{c}{2\pi^2}\sum_{f=0}^{f_0-2}\left.\frac{d\phi}{df}\right|^{f+\frac{1}{2}} \times \frac{1}{[f_0^2-(f+\frac{1}{2})^2]^{\frac{1}{2}}} + \frac{c}{2\pi^2}\left.\frac{d\phi}{df}\right|^{f_0-\frac{1}{2}} \times \left[\frac{\pi}{2} - \operatorname{acos}\left(\frac{f_0-1}{f_0}\right)\right], \quad (6.1)$$

where f is in GHz. The third term on the right is required to deal with the singularity in the integrand of Eq. 4.45 at $f = f_0$. Figure 6-1 shows the evaluation of several profiles using five data points as expected from the C-Mod Reflectometer and the inversion routine described above. In general, the inversion agrees reasonably well with the input profiles. Profiles with many sharp changes in slope, such as Fig. 5 in Fig. 6-1, are not well represented due to the limited number of measurements.

6.2 Data Reduction

The steps involved in converting raw group delay measurements into density profiles will be presented in the next few figures. Shot 950609011[b] will be used as an example. This shot was chosen because many of the phenomena typically measured by the reflectometer are present and the Thomson scattering system was absolutely calibrated a few days after this run. This was a 7.9 tesla shot with a lithium pellet injected

[a] $n_c \propto f^2$, interpolating w.r.t. f biases the inversion toward concave profiles.

[b] The shot numbering system deserves some explanation. The first two digits are the year, the next two are the month, the next two are the day, and the last three are the shot on that day. So this was shot 11 on the ninth of June, 1995.

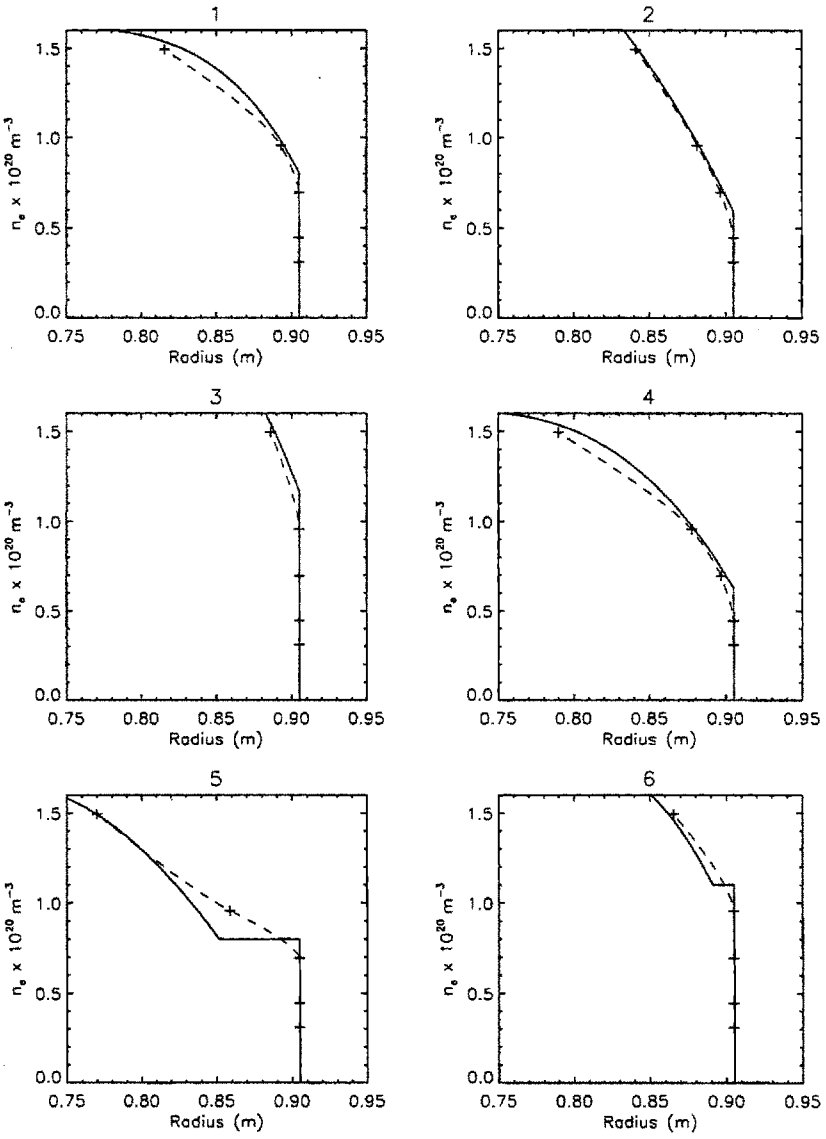

Figure 6-1: Model Profile Inversions. Input profiles are shown with solid lines and the inversions are shown with dashed lines. The +'s mark the five densities where group delays are measured.

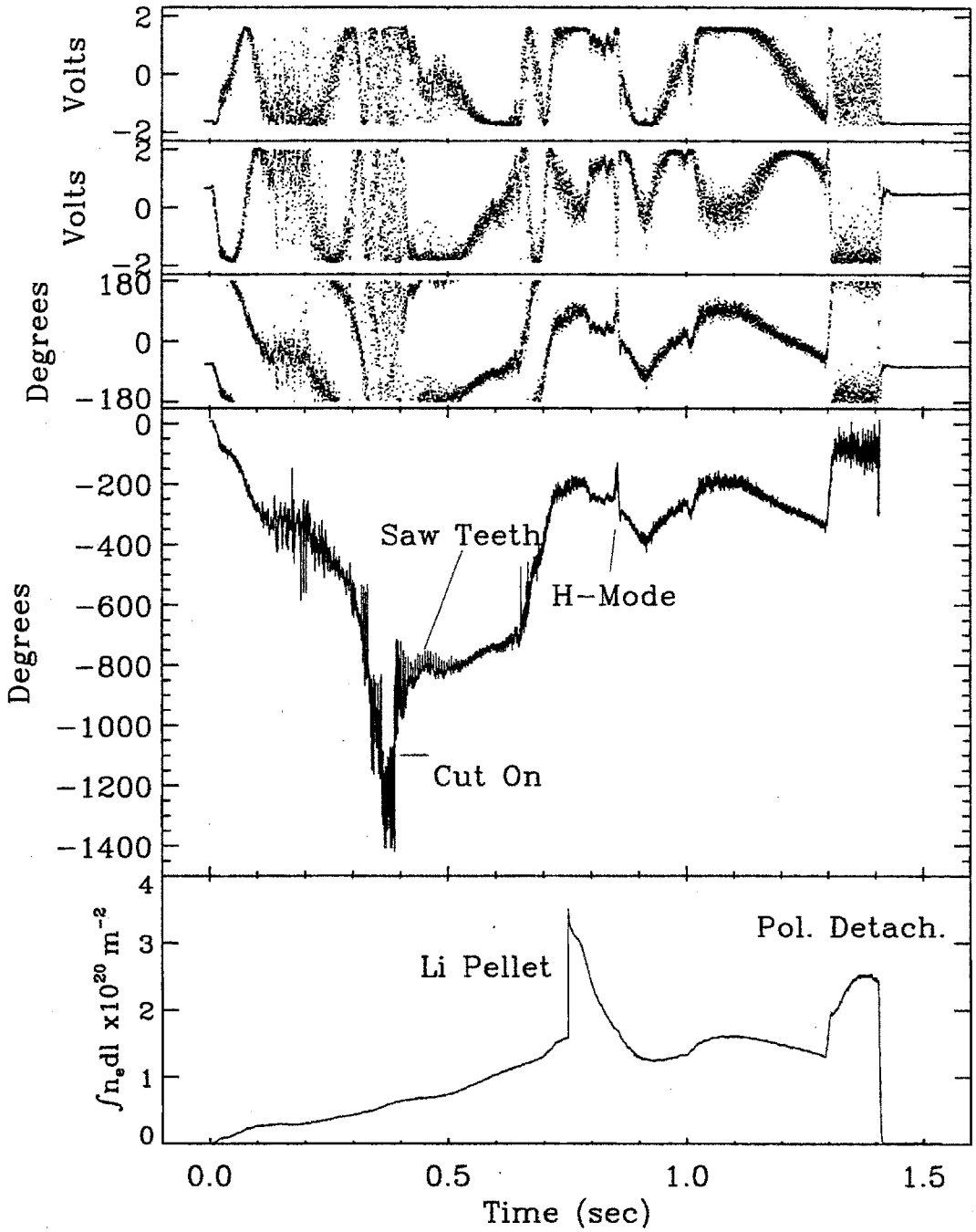

Figure 6-2: Raw 110 GHz Data (shot 950609011) The upper two plots are outputs from the I/Q outputs. The next is the phase determined from these measurements. The fourth plot is the phase with the fringe jumps taken out, and the 5th plot is the line integral density measured by the TCI.

at .75 seconds, followed by an H-mode[c] at .85 seconds, and a poloidal detachment starting at 1.3 seconds. The bottom plot in Fig. 6-2 shows the time history of the line integral of the plasma electron density as measured by the TCI. Clearly apparent is the pellet injection and the poloidal detachment. The very small kink in the density trace at .85 seconds is the H-mode. The top two plots in Fig. 6-2 show the I/Q output for the 110 GHz channel.

The phase of the returned signal (third plot from top) is extracted by taking the arctangent of the ratio of the two I/Q outputs. Fringe jumps are apparent between 0.4 and 0.5 seconds and at 0.7 seconds. The fourth plot shows the phase measurement after the fringe jumps have been removed. This step of the analysis is done by identifying fringe jumps manually via a graphical computer interface. A suitable automatic computer algorithm has not yet been developed. Visually determining when a fringe jump has occurred is generally straight-forward. However, there are times when it is possible to have a 2π ambiguity. These times are: during plasma startup; when the cutoff layer is inside or near the inversion radius where sawtooth modulation of the critical radius can be large and rapid; in the 300 ms following pellet injection, presumably, due to locally hollow portions of the density profile during the relaxation of the current profile; and during a dithering H-mode.

Prior to the shot, the reflectometer is reflecting off of the inner wall of the vacuum chamber located at a major radius of 44.0 cm. With a 1 GHz difference frequency (30 cm beat wavelength), a mirror located at 59, 74 or 89 cm would also give a phase of zero. For historical reasons, the the phase of the returned wave relative to one reflecting from a mirror at 89 cm major radius is displayed and a negative phase corresponds to a greater group delay. This means that a channel measuring 0 degrees is reflecting near the LCFS which is typically located at 89 to 90 cm. Figure 6-3 shows the phase of the returned wave for all five channels.

[c]This was the first H-mode ever observed above 5.3 tesla and was first identified by the reflectometer.

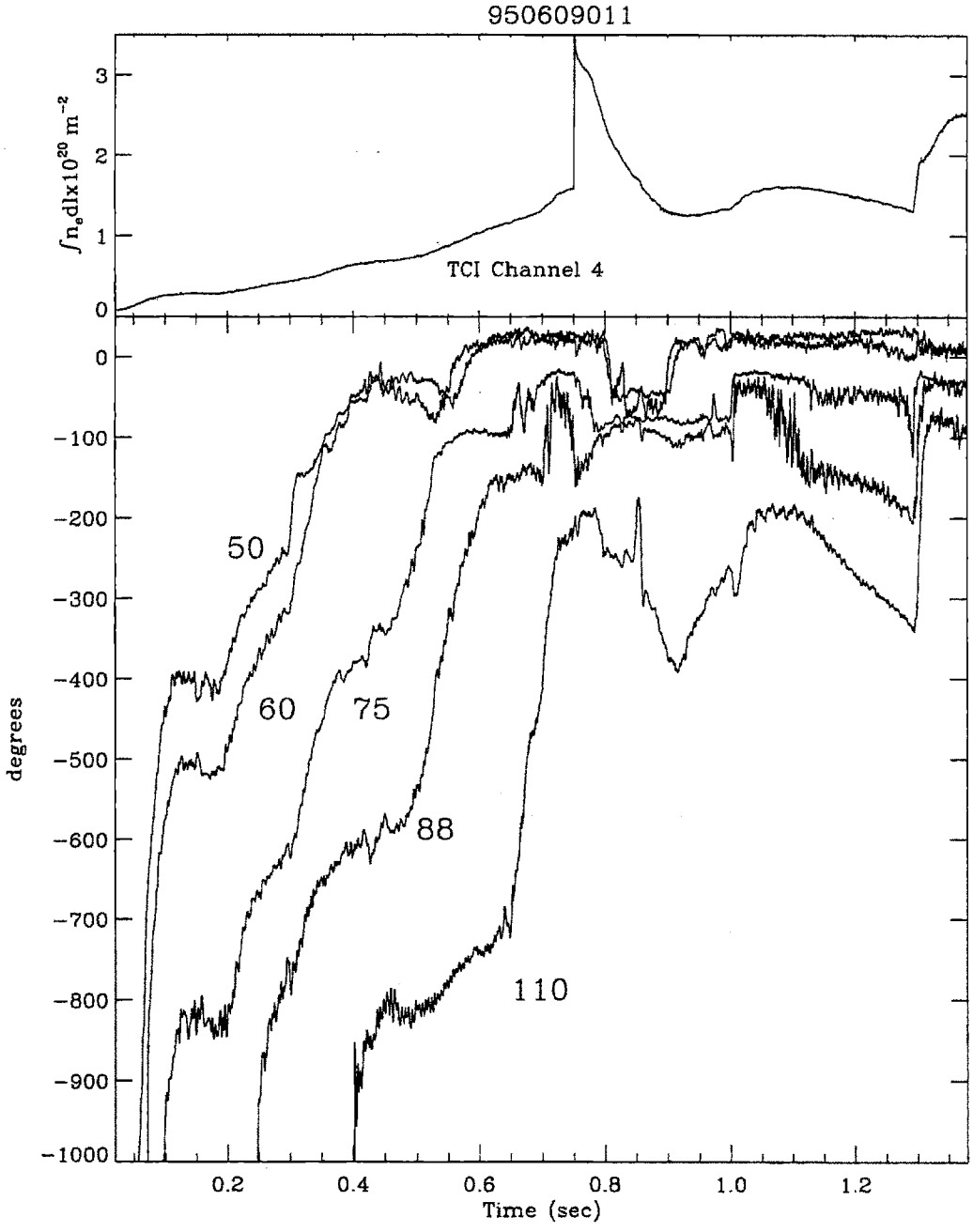

Figure 6-3: Example Raw Data (shot 950609011) A 500 Hz low pass filter has been applied to the data.

6.3 Calibration

A key element of the operation of any reflectometer is absolute calibration. This has been a challenge for several experiments [61, 24]. When launching into a metallic vacuum chamber, reflections will not be limited to the inner wall, and power reflected from objects other than the inner wall will corrupt the measured group delay[d]. In principle, a swept frequency reflectometer can distinguish between reflections from the inner wall and other structures in the machine. However, filtering in the receiver must be carefully chosen to eliminate spurious reflections while maintaining sensitivity to the expected range of profile shapes and locations [62]. For a fixed frequency reflectometer, any spurious reflections can corrupt the returned signal. That this is a problem for the C-Mod reflectometer can be seen in Fig. 6-4. This is from shot 950609013 which like 950609011 had a pellet and an H-mode. The H-mode between .8 and .86 seconds is much longer than the one in shot 11 and has a far more pronounced effect on the 110 GHz channel. In fact, the phases measured for the 75, 88, and 110 GHz channels are inconsistent: they predict the critical layers for 75 and 88 GHz lie further in the plasma than the critical layer for 110 GHz. By inferring an offset, these channels can be brought into agreement. Justification for inferring this offset and a protocol for doing so will occupy § 6.3.1 and § 6.3.2

6.3.1 High SOL Density Plasmas

Fig. 6-5 shows the phase measurements for shot 951206031. This was a particularly high density, gas fueled, ohmic shot. Note that as the density rises, all channels of the reflectometer go out to a fixed value. Also they reach this value in sequence, from lowest to highest frequency. This value is independent of plasma shape and position and remains the same from shot to shot. In particular it is independent of gaps between the LCFS and any limiting surface. This effect can be seen on the lower frequency channels for most diverted shots and on the higher frequency channels

[d]Other potential problems include amplitude to phase modulation in the receiver, pulling of oscillators and induced phase shift in filters due to the magnetic fields induced by the EF coils, and poor isolation between the receiving and launching arms of the receiver.

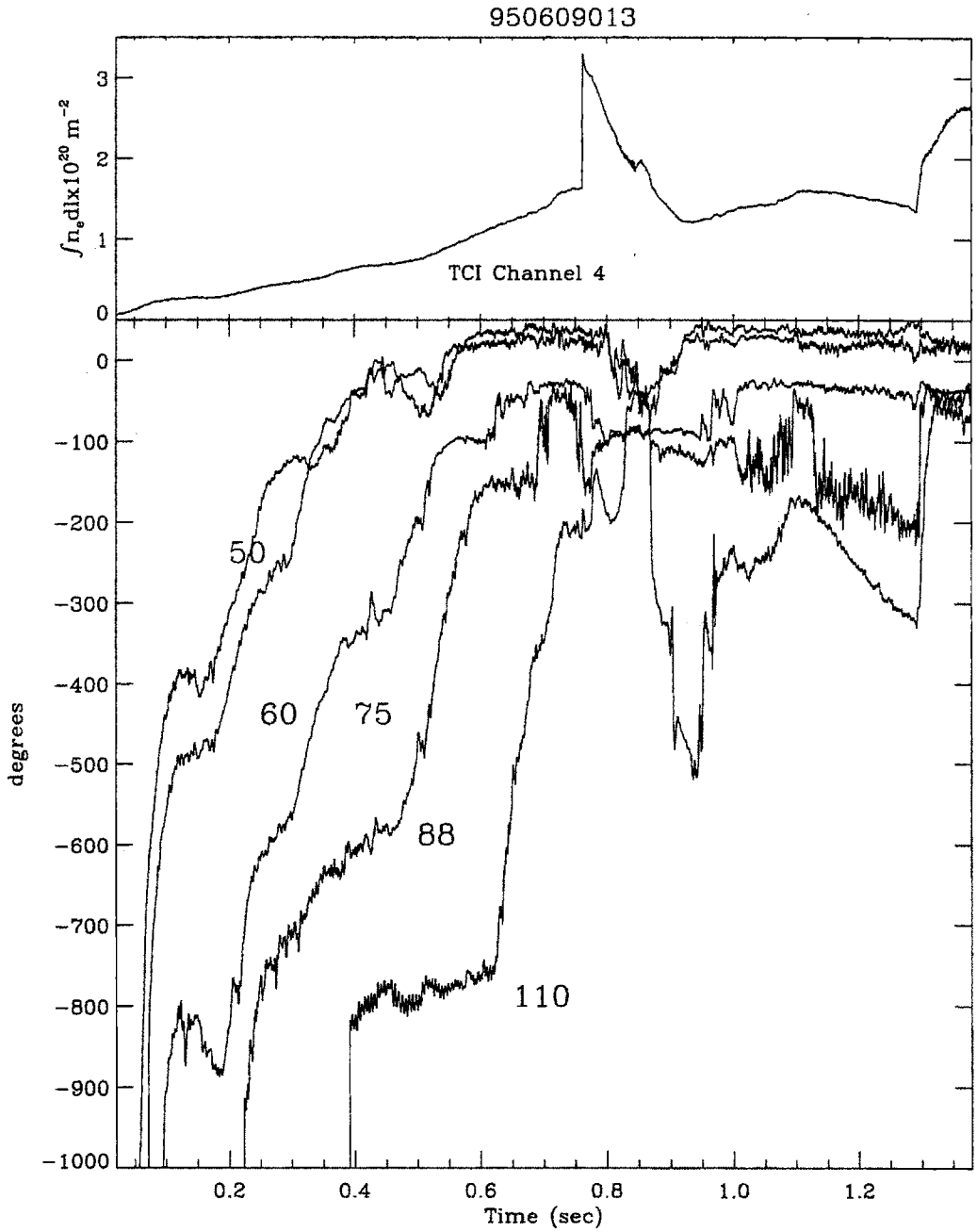

Figure 6-4: Example of Problem Raw Data (Shot 950609013) At .85 seconds the 110, 88, and 77 GHz channels are inconsistent. Also from .9 to .95 seconds the phase of the 110 GHz channel is ambiguous. The measurement could be 360 degrees higher during this period. A 500 Hz low pass filter has been applied to the data.

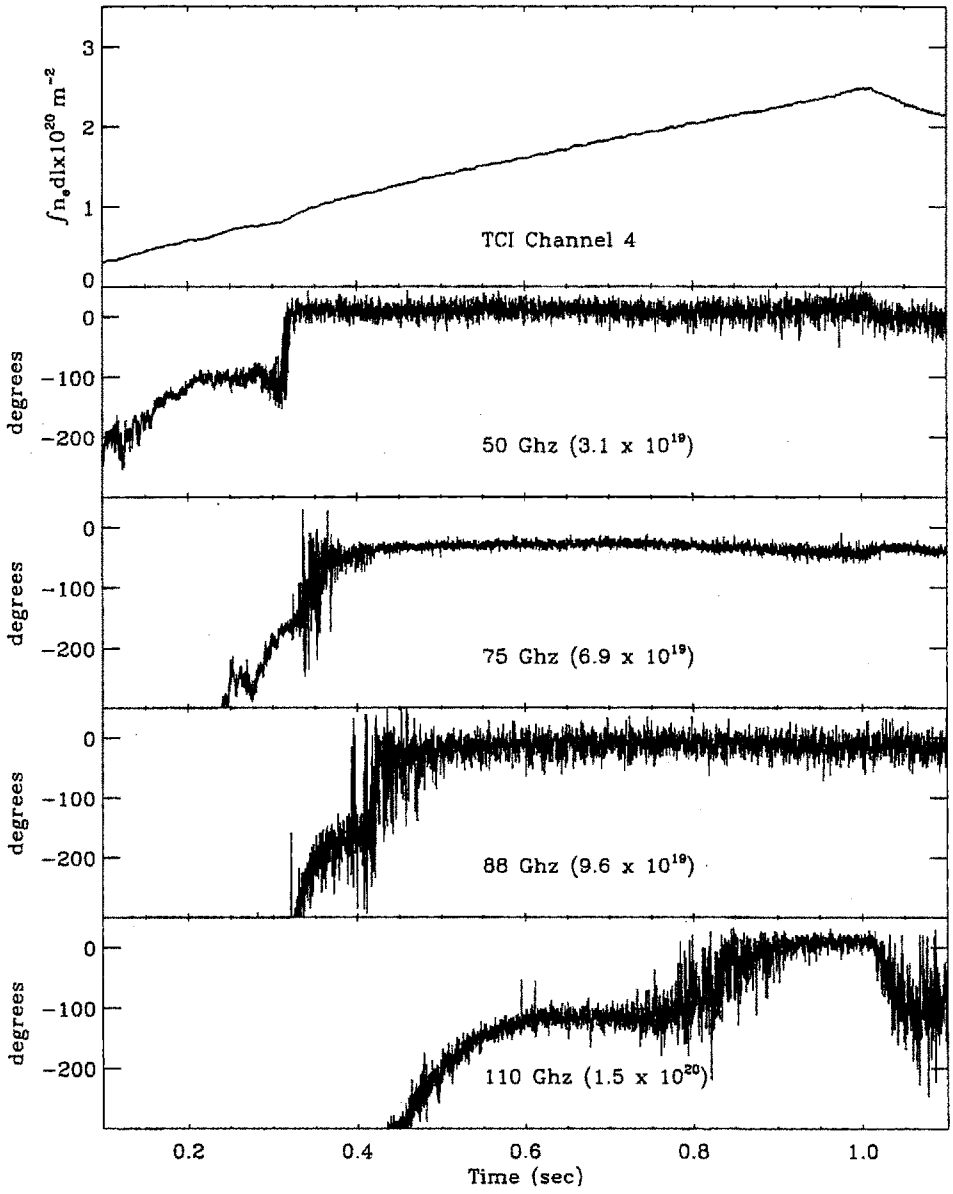

Figure 6-5: High SOL Density Shot. Above is shown a particularly high SOL density shot. Note that from .9 to 1.0 seconds all four channels are at a fixed location near $\theta = 0$. This position is assumed to be the limiter radius.

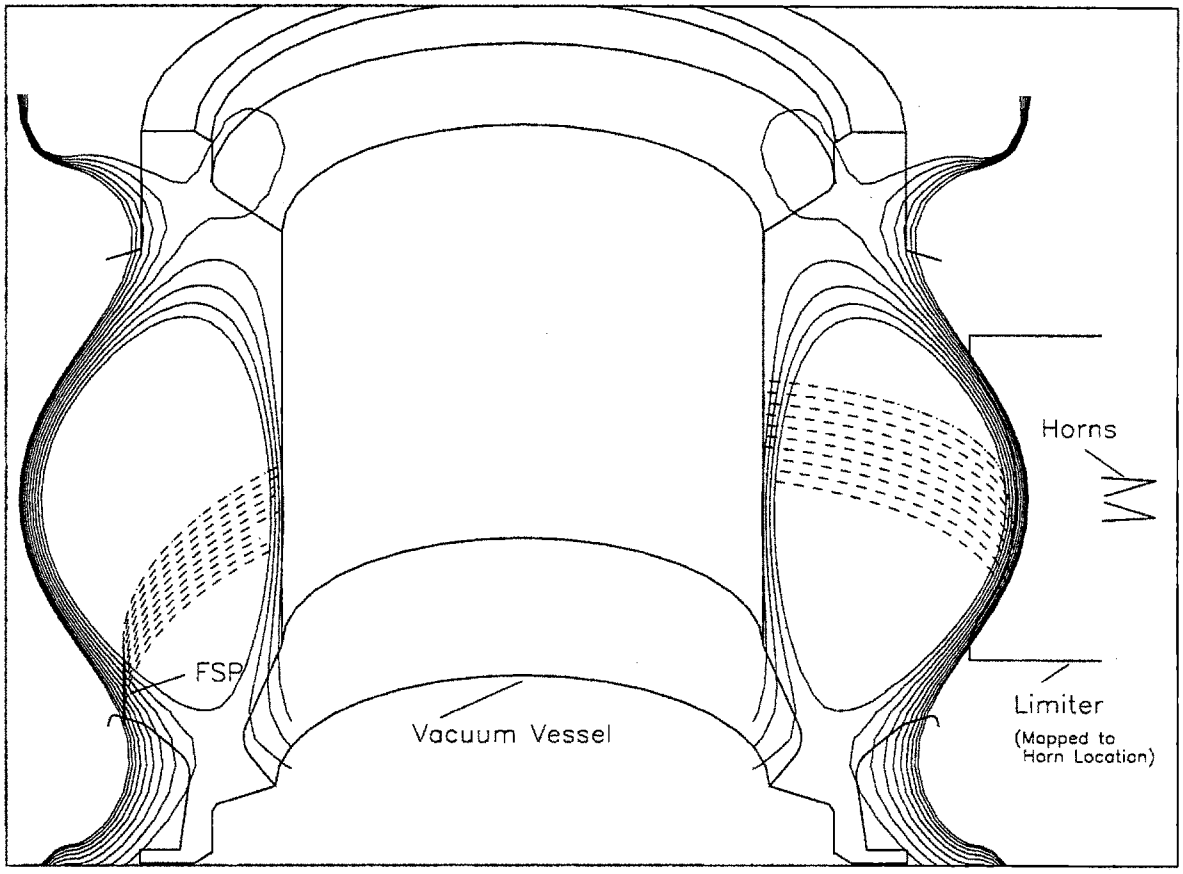

Figure 6-6: Fast Scanning Probe Mapping for a high field, high q shot.

on shots with extensive gas puffing, especially when the divertor is detached. This effect is also visible, though less clearly, on shot 950609011 (see Fig. 6-3). Note that channels 50 through 88 GHz all encounter an upper limit at .7, 1.05, and 1.3 seconds. The only fixed object that can be causing this is the limiter located 16 cm toroidally from the reflectometer horns (see Fig. 3-2). These observations point to there being a steep gradient in the plasma density at the limiter radius, near the limiter. This steep gradient can be used to calibrate the reflectometer by assuming a step function in the plasma density at the limiter radius.

6.3.2 Comparison with Fast Scanning Probe

The fast scanning probe (FSP) is located 180 degrees toroidally from the reflectometer (see § 3.2.3 and Fig. 3-2). In general, the FSP insertion into the SOL up to the LCFS

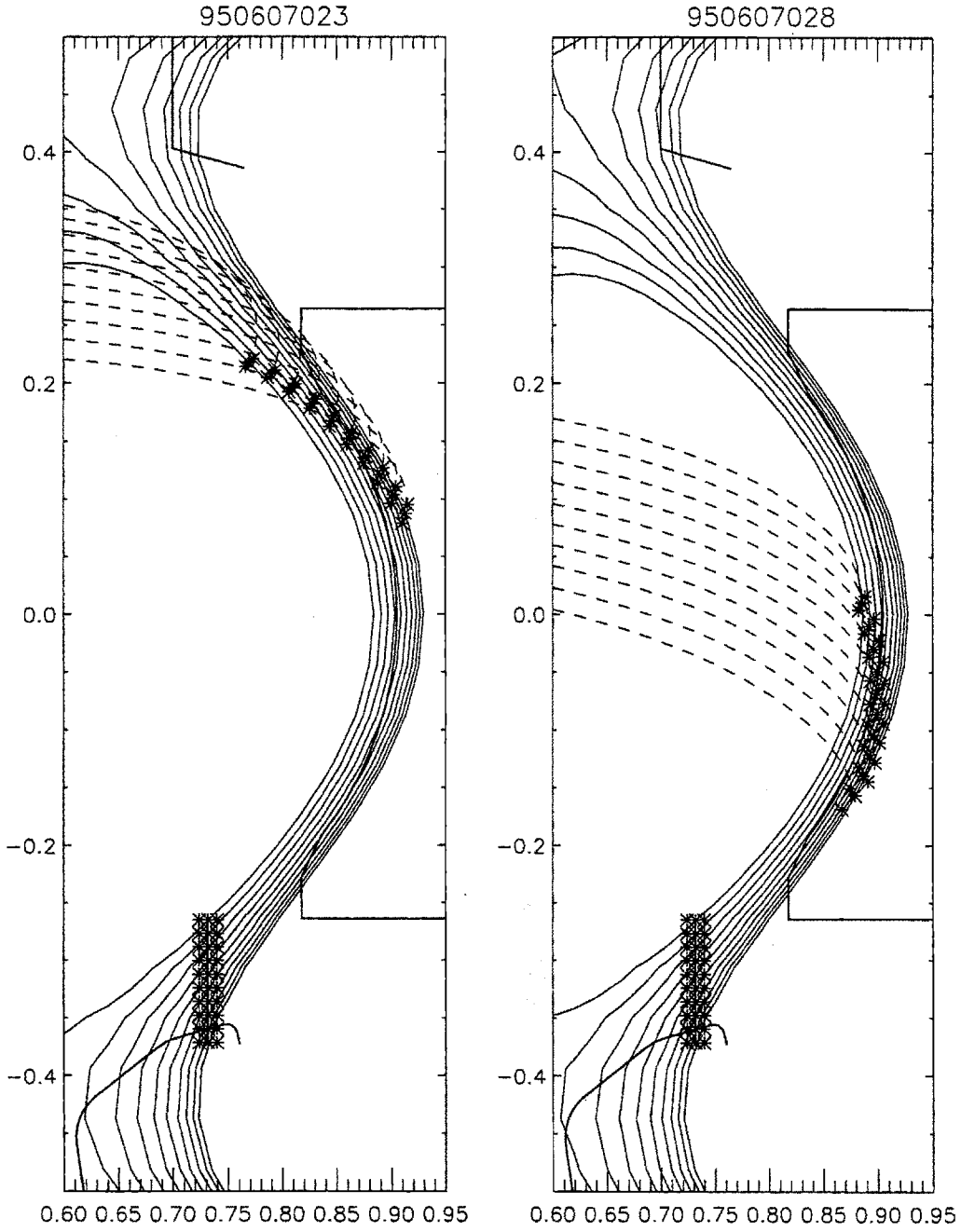

Figure 6-7: Closeup of Mapping of Fast Scanning Probe for two shots. These are expanded views of the flux mapping shown in Fig. 6-6. Shot 23 was a 3.5 tesla while shot 28 was at 7.0 tesla. The mapping to the toroidal location of the reflectometer is indicated by the stars. The stars in the lower portion indicate the FSP location on the opposite side of the machine.

produces no significant change to the main plasma other than an occasional rise in the radiation from molybdenum lines[e]. For a small number of shots the edge q was high enough[f] for the location of the FSP to map along the field lines to the view of the reflectometer (see Fig. 6-6). For ohmic plasmas with the proper field mapping, a perturbation to the SOL caused by the FSP can be seen with the reflectometer. This perturbation is not seen on shots where the flux tube intersected by the FSP does not map to the reflectometer view. Figure 6-7 shows an expanded view in Fig. 6-6 of the mapping of the probe flux tube to the reflectometer toroidal position for two shots. In shot 950607023, the mapping misses the reflectometer field of view and no perturbation of the profile is observed. Shots 950607030, 28 and 29 (see Fig. 6-8 & 6-9) are a density scan at constant B_T and plasma current. In shot 30, only the 60 GHz channel was at the fixed position[g] that is presumed to be the limiter radius prior to the FSP insertion. The group delay is increased on the 60 GHz channel during portions of the period of the probe insertion, but the other three channels show no significant effect. Also note that the first perturbation on the 60 GHz profile occurs at approximately the same time as the tip of the FSP crosses the limiter radius. Profiles for the reflectometer during both the depleted phase and the post probe phase are plotted with a smoothed profile from the FSP. Note the quite good agreement during the depleted phase between the probe and the reflectometer. The reflectometer profiles were obtained using the algorithm described earlier in this chapter with an offset such that the fixed position attained by each reflectometer channel corresponds to an step function in the density profile at the limiter radius.

Shots 950607028 and 29 show the same traits as shot 30 but at higher density. For shot 28 only the 75 Ghz channel is affected and on shot 29 only the 88 Ghz channel is significantly affected. The reflectometer profiles for each of these shots also show better agreement with the FSP during the depleted phase. On shot 29 the limitations of using only five fixed frequencies is apparent. The critical radius for the 110 GHz channel probably does not change as the probe is inserted, however there are not

[e]The probe head is constructed from molybdenum.

[f]High B_t, low plasma current

[g]On this day the 50 GHz channel was not operating.

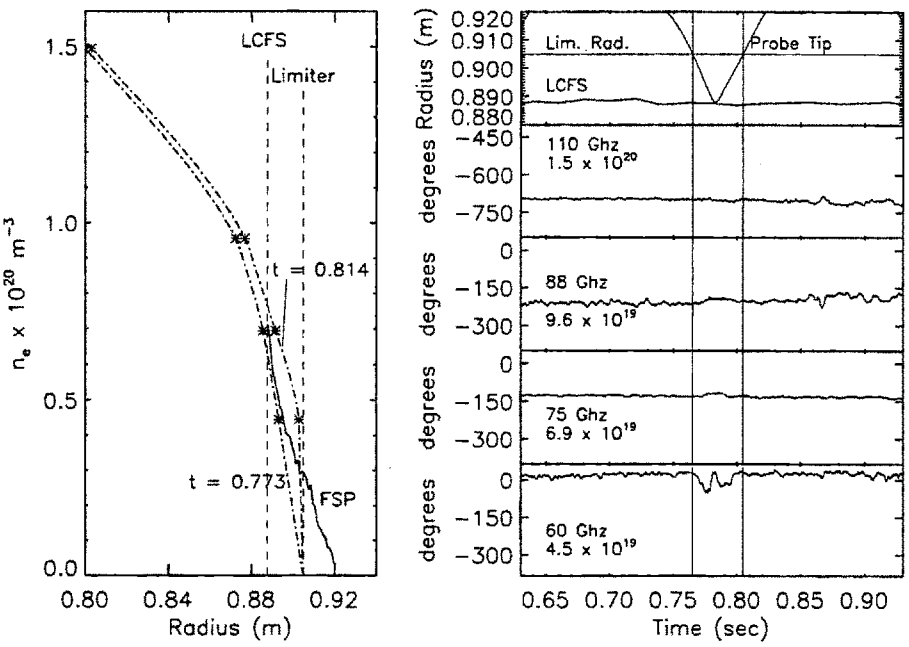

Figure 6-8: SOL Perturbation by Fast Scanning Probe shot 950607030. The left hand plot is a profile generated by the FSP (solid line) and the reflectometer both during the probe insertion and afterwards. The right hand plot is the raw phase measurement of the four channels working that day. Note that only one channel is strongly affected by the probe. Also, the timing of the perturbation is coincident with the FSP tip crossing the limiter radius.

enough data to construct a profile with an inflection point as in shot 28.

6.3.3 Models for Probe Observations

Two models can explain the observed interaction between the SOL, the limiter, and the probe. It should be pointed out that either of these models will allow this steep gradient to be used as a calibration marker. The first, and more conventional, is to assume that the limiter and the probe are both sinks for particles. Figure 6-10 shows a two dimensional representation of the SOL. Ions and electrons will recombine at the limiter so it is a plasma sink and will deplete the plasma along the field lines that intersect it. Cross field transport will supply plasma to these field lines creating a

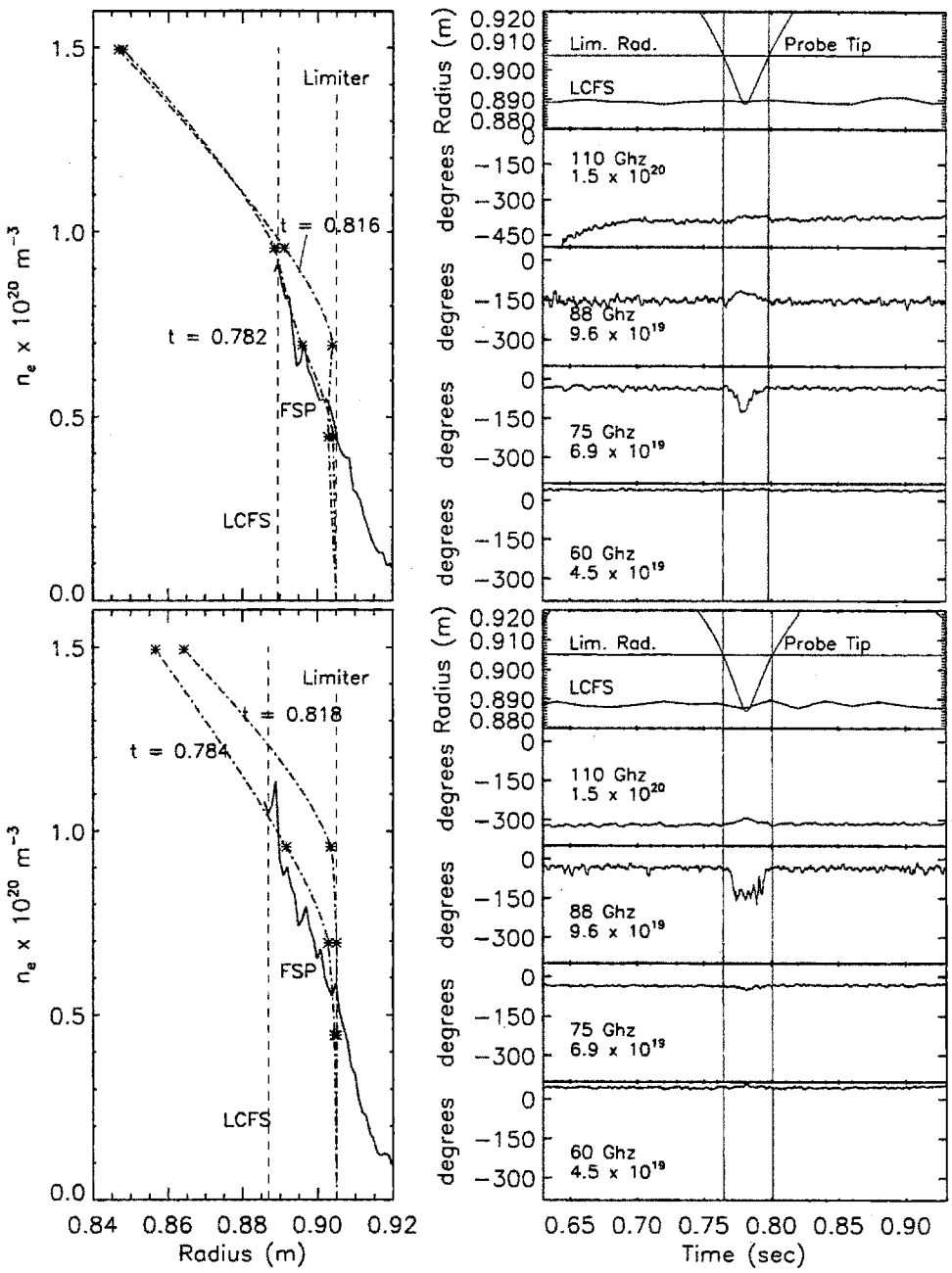

Figure 6-9: SOL Perturbation by FSP at Higher Density shots 950607028 & 29. A density scan at the same field and current as in Fig. 6-8. Note that only one channel is strongly affected by the probe in each shot.

net flow from the main plasma to the limiter. The reflectometer sits approximately 16 cm from the AB poloidal limiter. The fast scanning probe lies approximately 2.8 meters along the field line from the limiter. The divertor is approximately another three meters further along the field line. If we take the probe to be located in a region without significant flow Stangeby [63, 64] provides a rather simple model of the density profile along the x axis. Assume a constant source, S, depositing particles into the flux tube as shown. Defining the Mach number, M, and the ion sound speed, c_s:

$$M = \frac{v}{c_s} \qquad \text{where} \quad c_s = \left[\frac{k(T_i + T_e)}{m_i}\right]^{1/2} \tag{6.2}$$

Stangeby derives the following relation from the momentum equation and continuity

$$\frac{dM}{dx} = \frac{S}{nc_s}\frac{1+M^2}{1-M^2}. \tag{6.3}$$

For $S \propto n$ this can be integrated to give:

$$\frac{L-x}{L} = \frac{2M}{1+M^2} \quad \text{and} \quad \frac{n(M)}{n_0} = \frac{1}{1+M^2} \tag{6.4}$$

where L is the distance from the probe to the limiter. The Bohm condition that the velocity at the edge of the sheath equals the sound speed is assumed. From this parameterization, the density variation along the flux tube is obtained. Note that the reflectometer is expected to measure 60% of the value measured by the fast scanning probe. This depletion in front of the reflectometer at the limiter radius may explain the fixed value in the group delay measured by the reflectometer channels for high SOL density shots.

The probe inserted into the SOL depletes the density along the flux tube that it intersects. This increases the group delay for a channel previously seeing the limiter radius and now looking deeper into the SOL and decreases the group delay for channels looking deeper into the plasma. This can be seen in Fig. 6-9 for the 88 and 110 GHz channels respectively. Stangeby [64] gives a value for the length of the flux tube

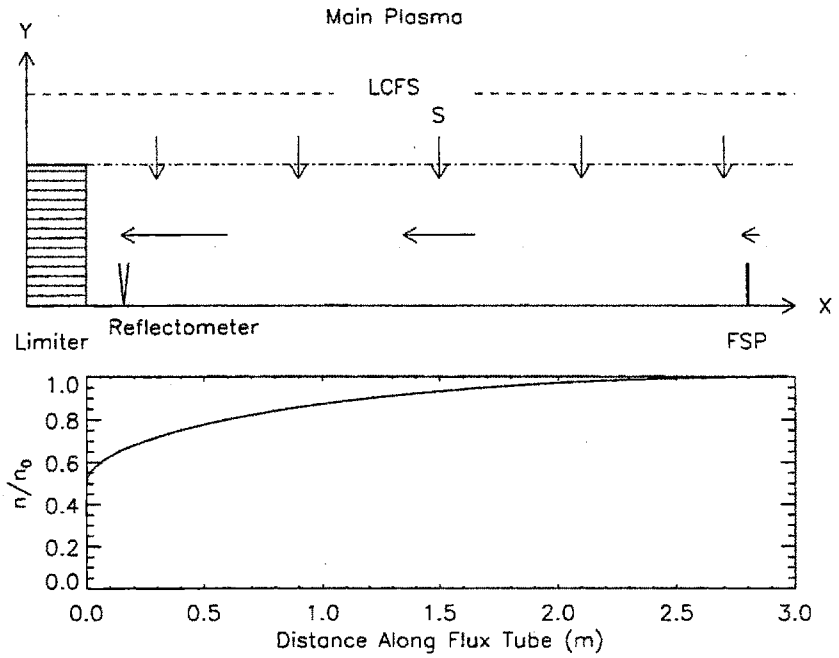

Figure 6-10: SOL Model

depleted by a probe of dimension d:

$$L_{col} \approx \frac{d^2 c_s}{D_\perp} \tag{6.5}$$

The probe is 1.5 cm in diameter and for a 5 eV deuterium plasma $c_s \approx 16$ km/s giving $D_\perp < 1.7\text{m}^2/\text{s}$. This is far greater than the Bohm value of $\approx 0.06\text{m}^2/\text{s}$ or the value of 0.08 to 0.2 m^2/s estimated from fast scanning probe measurements [65]. So while this calculation demonstrates that observing a perturbation of the SOL from the FSP is expected, the upper limit it gives to the diffusion coefficient is so far removed from the expected value that the measurement is not particularly useful beyond calibrating the reflectometer. Matthews [66] has performed similar experiments on DITE using two probes rather than a probe and a reflectometer. He was able to make quite detailed measurements of $D_\perp$ by measuring the two dimensional profile of the perturbation caused by one probe. Unfortunately the current C-Mod arrangement provides no spacial resolution in the poloidal direction, preventing similar measurements from being performed here.

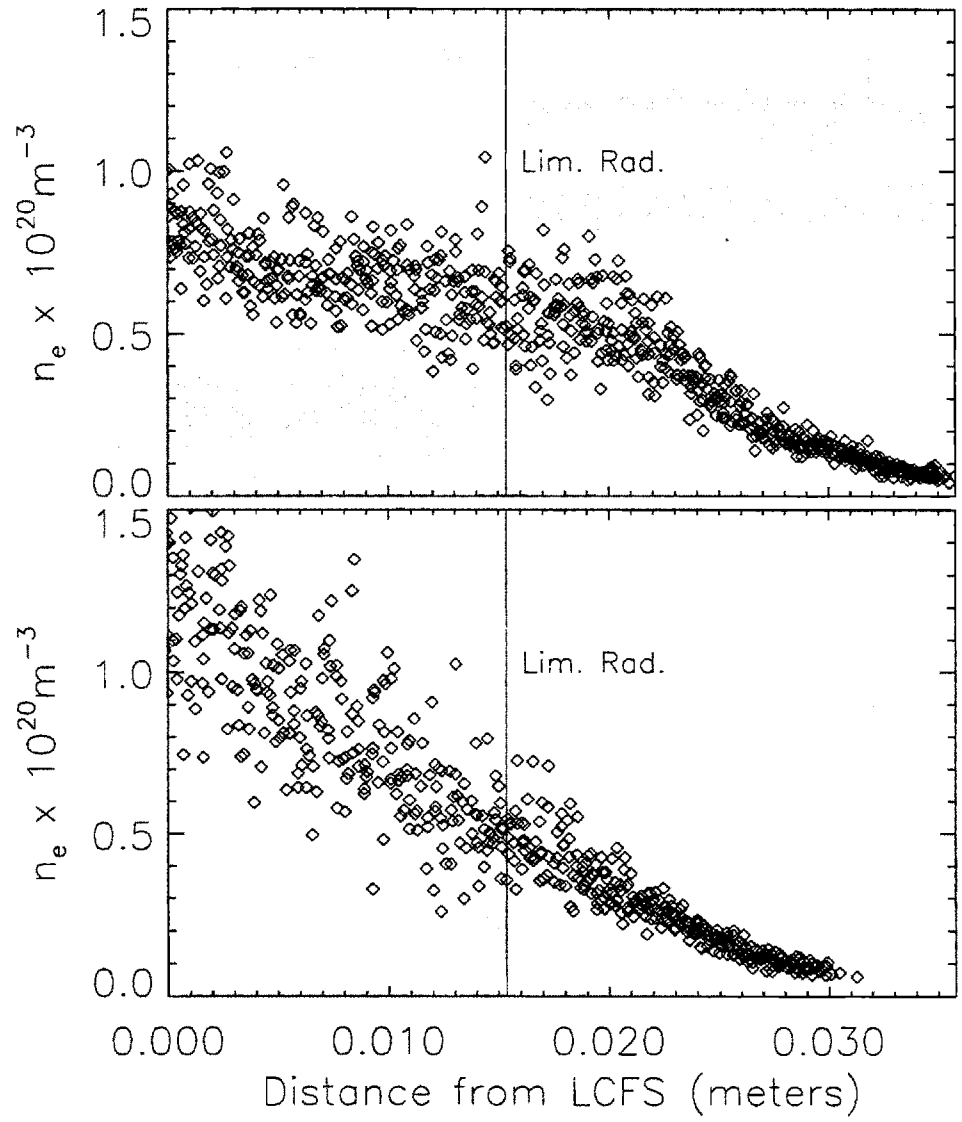

Figure 6-11: Density Measurements From FSP shot 950607029 The upper plot is from the probe facing the limiter while the lower one faces the divertor. Note the large scatter in the data.

Another model for the probe and limiter measurements assumes that the SOL is extremely turbulent. For the comparisons shown in Fig. 6-9, the electron density measured by the two working langmuir probes on the end of the FSP were smoothed and averaged. Figure 6-11 shows the densities measured by the probe looking towards the limiter and looking towards the divertor. The noise on the data is quite apparent and presumably represents fluctuations in the plasma density. A density profile that is varying greatly in space will bias a reflectometer measurement to larger major radius as shown in Fig. 6-12. If the limiter somehow damps the oscillations in the plasma, the reflectometer will see what appears to be a very steep gradient at the limiter radius. If the probe moving into the SOL does the same thing, it will allow a reflectometer channel that previously saw only to the limiter radius to see deeper into the plasma, in agreement with what we observe.

6.4 Comparison with Other Diagnostics

6.4.1 Typical Features Observed with the Reflectometer

Returning to shot 950609011, the profile generated using the inversion scheme described earlier is shown in Fig. 6-13. There are a few common phenomena that are worth mentioning that are apparent during this shot. First, the deuterium pellet that is fired into the plasma at .75 seconds has very little effect on the region of the plasma that the reflectometer is observing. The pellet apparently deposits little in the plasma edge, while the plasma inventory increases greatly (as shown by the TCI in Fig. 6-2). Second, when strong gas puffing is applied, the region between the LCFS and the limiter can reach densities of 10^{20} m^{-3} or more. The gas valve is controlled by the hybrid computer, which compares the density measured by the TCI with a preprogrammed density waveform. Typically, the gas puff is turned off after a pellet as the central density exceeds the preprogrammed density. The closing of the gas valve results in a dramatic decrease in the SOL density and quite often an H-mode. When the gas puff is turned back on again, the high SOL density returns. Third, a

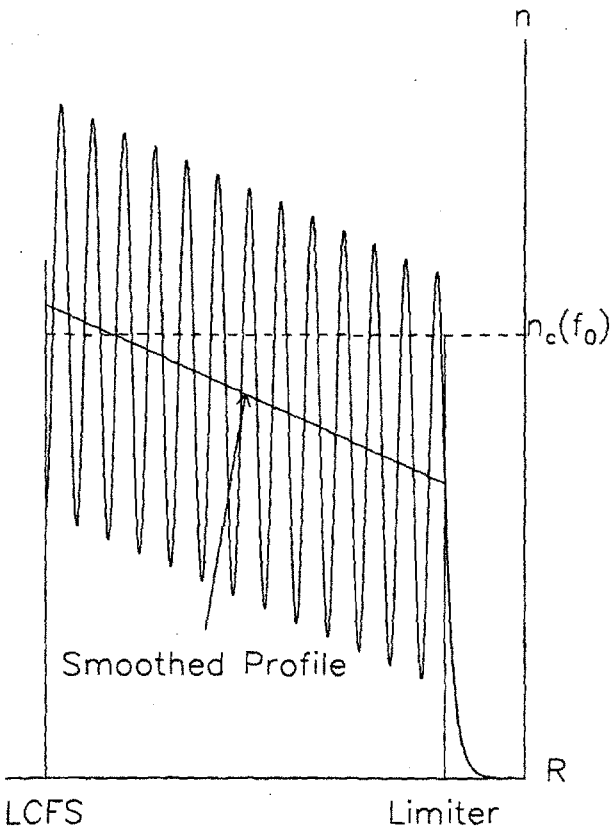

Figure 6-12: Reflectometer View of a Turbulent Edge. If the plasma edge is very turbulent a reflectometer channel reflecting in this region will measure a shorter group delay relative to a time averaged or spatially smoothed profile.

shot that survives until current rampdown, often will exhibit a poloidal detachment. In the shot in question, this occurs at 1.3 seconds. At this time the plasma current is being ramped down and rather than being diverted it is limited on the inner wall. The cold plasma outside the LCFS again can be quite dense ($> 1.5 \times 10^{20}$ m^{-3}).

6.4.2 Sawtooth Observations

One check on the inversion routine is to compare where the reflectometer would position various sawtooth phenomena to what the x-ray tomography and ECE diagnostics observe. A sawtooth is a relaxation oscillation at the plasma center. The generally accepted explanation for this oscillation is that the current density will tend to peak

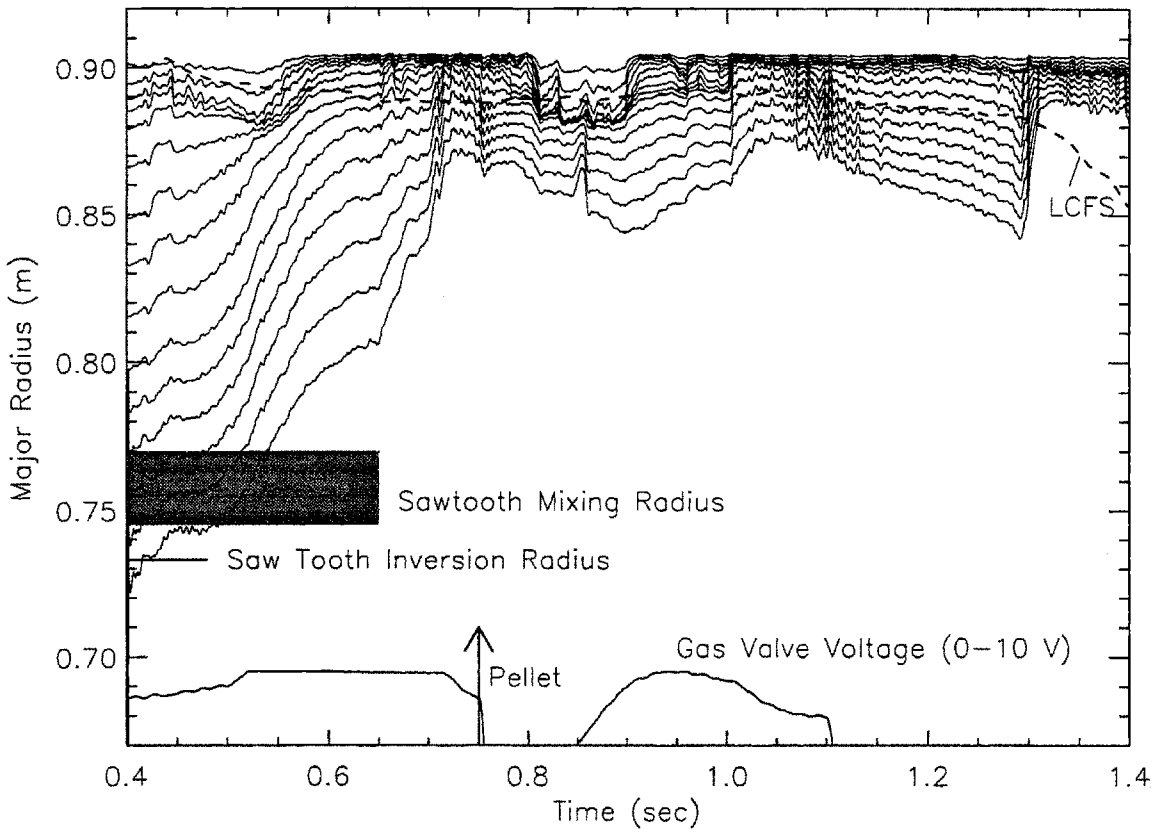

Figure 6-13: Density Profile Evolution for Shot 950609011. Contour spacing is 10^{19} m^{-3} from 1 to 15 $\times 10^{19}$.

on axis where the conductivity is the highest. However if the current density gets too high the central plasma is unstable to resistive tearing modes. During the sawtooth crash, plasma inside the inversion radius mixes with plasma just outside the inversion radius[h]. The effect on the density profile is shown schematically in Fig. 6-14. The effect on the temperature profile is similar except the heat pulse generally extends diffusively out to the plasma edge. The inversion radius is pretty clearly observed via either ECE or x-ray tomography. Here the value for the inversion radius is taken from the x-ray diagnostics. The mixing radius is where the temperature and density are promptly effected by the sawtooth crash. The mixing radius is not as clearly defined as the figure suggests. After the sawtooth collapse, the profile gradually peaks up again to the presawtooth shape. At larger radii the plasma sees a perturbation appearing on a diffusive time scale.

[h]The inversion radius is widely believed to be at the q = 1 surface.

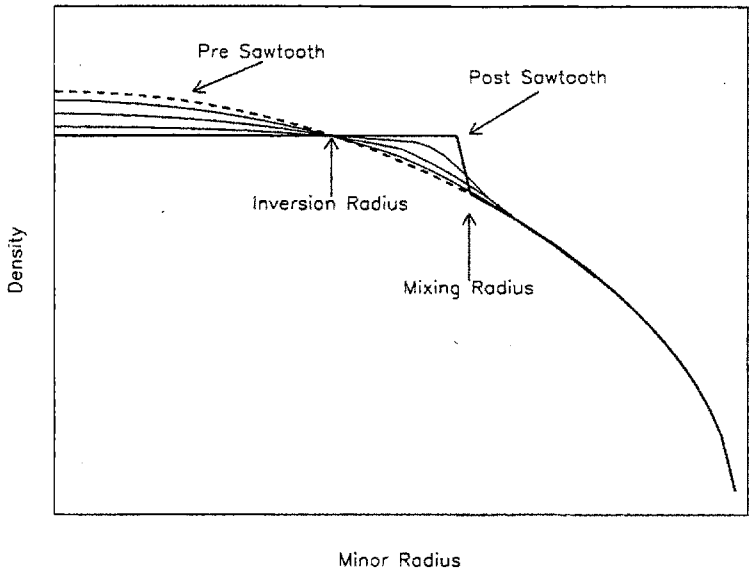

Figure 6-14: Crude Sawtooth Model. The density and temperature profiles change in less than a millisecond from the dashed profile to the solid profile. The thin lines show how the profile may evolve back to the pre-sawtooth profile during the 10's of milliseconds before the next sawtooth.

Figure 6-15 shows sawtooth signals from the reflectometer and several of the GPC channels. Channel 5 of the GPC shows a very rapid upward spike in the temperature at the sawtooth crash. This channel is clearly looking in the region between the inversion radius and the mixing radius. Channel 6 however has a more rounded shape, putting it near or just inside the mixing radius. This places the mixing radius somewhere between 0.75 and 0.78 meters major radius. Looking at the 110 GHz reflectometer channel for this shot in the top plot in Fig. 6-15, three distinct sawtooth responses can be seen as the plasma density is ramped up. Before 0.41 seconds the group delay modulation from the sawteeth is too large for the reflectometer to follow. Presumably, this corresponds to a presawtooth location for the critical layer inside the inversion radius. From 0.41 to 0.52 seconds the reflectometer sees a very rapid spike corresponding to a reduced group delay. Since the group delay is reduced, the channel is looking outside the inversion radius. The very rapid response implies that the critical layer is inside the mixing radius. The slower sawtooth response to the

sawteeth after 0.53 seconds indicates the critical layer is outside of the mixing radius.

Comparing these observations with the inversion generated by the reflectometer gives quite good agreement. At about 0.42 seconds the inversion radius is crossed by the contour corresponding to 1.5×10^{20} m^{-3} or the 110 GHz channel.

6.4.3 Comparison with TCI and TS

Figure 6-16 shows profiles generated by the reflectometer, Thomson scattering, and the two color interferometer for shot 950609011 again. The agreement between the Thomson scattering and the reflectometer is rather good, though the two central channels of the TS are inside the inversion radius, a region not measured by the reflectometer. The interferometer on the other hand measures a much higher density between 0.80 and 0.90 meters. While the interferometer profile inversion is hampered by a shortage of information about the density at large minor radius, the chord measurements at 0.76 and 0.78 meters in general indicate substantially larger densities than those measured by the reflectometer. This effectively eliminates the possibility of including the reflectometer and the TCI in a combined profile inversion. A source for this problem has not yet been determined, though a likely explanation is plasma unaccounted for outside the LCFS, particularly in the upper portions of the machine where there are no probes present.

6.4.4 Thomson Scattering Calibration

One of the most powerful plasma diagnostics is incoherent Thomson scattering (see § 3.2.2). Thomson scattering can give local measurements of the electron temperature and density, however it is also one of the most difficult to calibrate. Determining the electron temperature can be comparatively straightforward by observing the linewidth of the scattered light. The electron density calibration is much harder to determine because it depends on the absolute magnitude of the ratio of the scattered over incident light. Any time alignment, transmission efficiency, or detection efficiency changes, the diagnostic needs to be recalibrated. The standard calibration

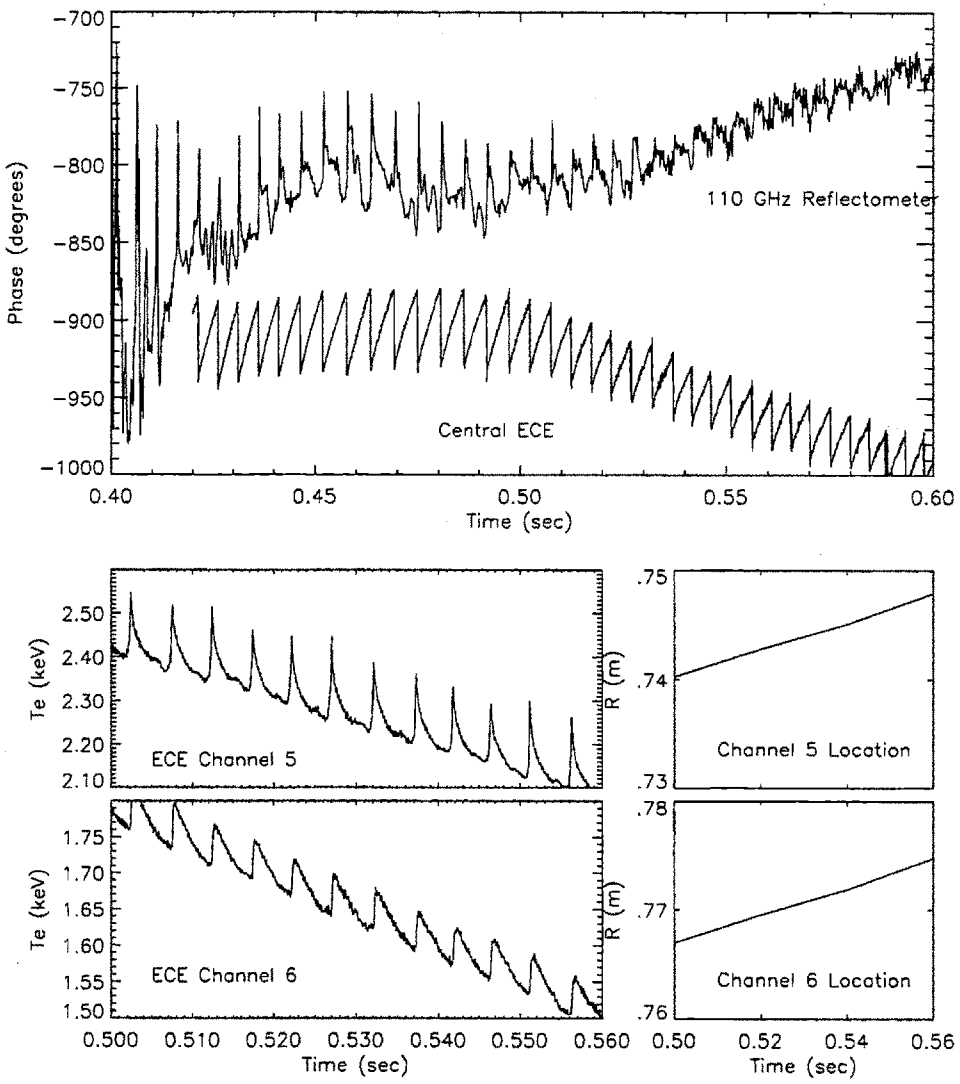

Figure 6-15: Sawtooth Mixing Radius shot 950609011 Channel 5 of the GPC shows a very rapid upward spike at the sawtooth crash, indicating that it is located inside the sawtooth mixing radius. Channel 6 shows a more rounded sawtooth response, indicating it lies at or outside the sawtooth mixing radius. (The position of the GPC channels is moving because the TF is ramping up.) The reflectometer sawtooth response resembles channel 5 of the GPC at 0.45 seconds and channel 6 at 0.55 seconds indicating the cutoff is moving from inside to outside the mixing radius.

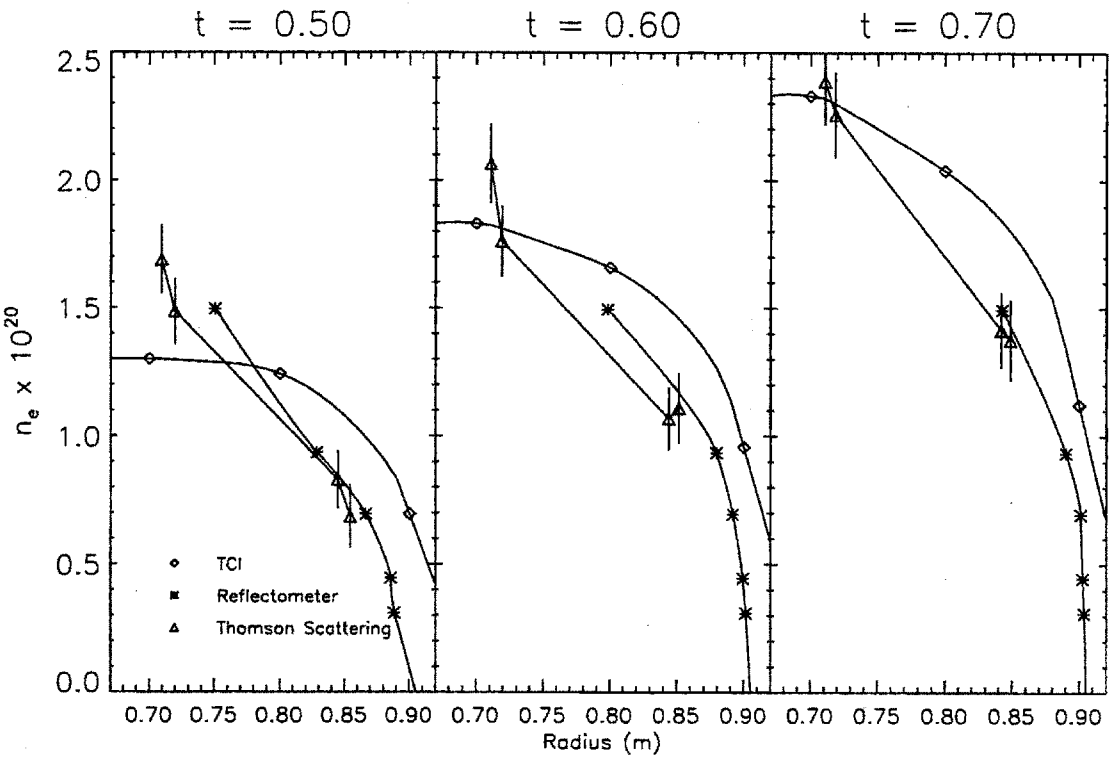

Figure 6-16: Comparison of TCI, TS, and Reflectometer. shot 950609011 The Thomson scattering diagnostic and the reflectometer agree reasonably well during the shot, however the interferometer gives a consistently higher value at large R and a somewhat lower value in the center.

technique involves backfilling the vacuum chamber with some gas (typically hydrogen or argon) and observing light from Raman or Rayleigh scattering. Typically the vacuum chamber must be kept at a uniform temperature and a whole day is needed to get the desired statistics. On C-Mod this can only be accomplished during an extended (one month or more) maintenance period. The TS can be cross calibrated with the density profiles generated by the reflectometer or the interferometer or by observing the cutoff on the ECE for particularly high density shots. This of course transfers whatever systematic errors are present in one diagnostic to the Thomson scattering.

An alternate, and potentially very accurate, technique for calibrating at least the central channel of the TS is to observe the transition from transmitting to reflection

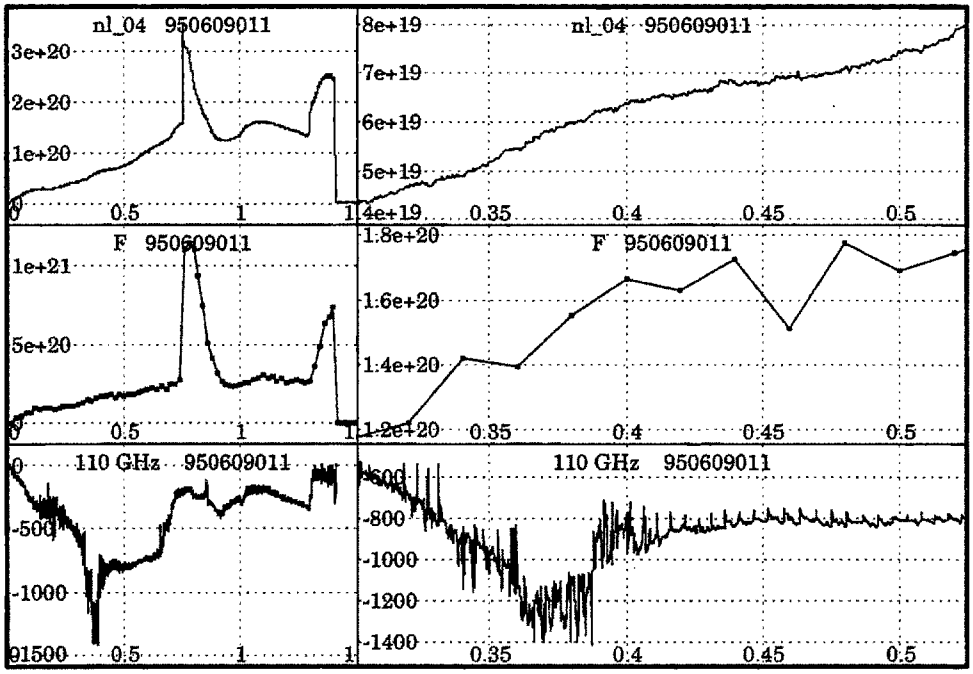

Figure 6-17: Thomson Scattering Calibration from Reflectometer Cutoff. On the left are traces from the TCI, TS and 110 GHz Reflectometer Channel for the entire shot. On the right is a blown up view of each trace during the initial density ramp as the reflectometer cuts on. The TS measurement from the plasma center crosses 1.5×10^{20} m^{-3} as the reflectometer sees the cut off.

of a channel of the reflectometer. Figure 6-17 shows shot 950609011 again[i]. Shown on the left are the the central channel of the interferometer and TS along with the 110 GHz channel of the reflectometer. On the right is a blowup of the same signals near the time of the reflectometer is making the transition from looking through the plasma (t=0 to 0.36 seconds) and reflecting off the plasma (t > 0.41 seconds.) During this time, the density measured by the TS increases from 1.4×10^{20} to 1.65×10^{20} m^{-3}. If the plasma is assumed to be peaked on axis and a constant value over the central 2 cm that the TS scatters from, then the density must have equalled the critical density for 110 GHz (1.5×10^{20} m^{-3}) at some point during the period $0.36 < t < 0.41$. Hence, the reflectometer confirms the calibration of the central channel to $\sim$ 10%. This is not too impressive: however, on shots where the density ramp is slower, this number

[i]This run day was the last of the spring 95 campaign so the TS could be calibrated in the days immediately following the run.

can be reduced to $\sim 5\%$, making this calibration technique potentially more accurate than traditional scattering calibrations. It should be pointed out that this technique only assumes that the plasma density has a maximum on axis, the plasma density is relatively flat near the center, and the definition of the plasma frequency is accurate, all rather safe bets.

Chapter 7

Reflectometer Studies of H-modes

As was discussed in § 2.6 and § 3.3.4, an important topic in fusion research is understanding and controlling the characteristics of H-mode plasmas. The dominant characteristic of these modes is the formation of a high gradient in density and temperature at or near the LCFS. Reflectometry is particularly well suited to the study of the evolution of this Steep Gradient Region (SGR). In this chapter, the transition rate from an L-mode to an H-mode density profile and the width of the fluctuation suppression region during C-Mod H-modes will be presented.

7.1 H-mode Characteristics

Figure 7-1 shows the raw data from a typical ICRF heated H-mode from the spring of 1995. After 100 ms of application of 2 MW of ICRF power, the D_α emission drops dramatically at 0.82 seconds indicating a drop in particle recycling and a transition from L to H mode. This is followed by a few ELMs and an ELM-free period to 0.85 seconds after which the ELMs start again and a return to L-mode at 0.885 seconds. During the ELM-free period the stored energy as measured by the magnetics rises modestly from 90 to 115 kJ while the line integrated density rises much more dramatically. However, showing the greatest change is the radiated power as measured

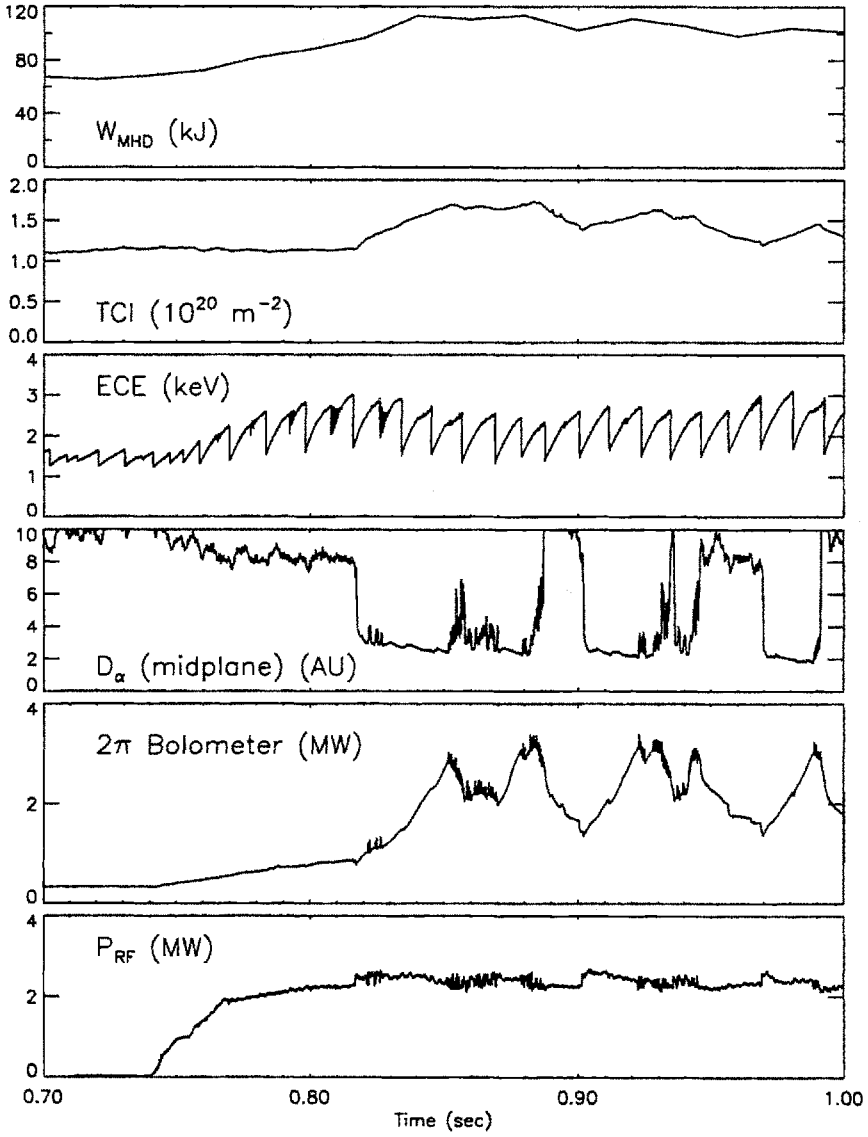

Figure 7-1: Radiation Limited H-mode (shot 950602024) The L-H transitions occur at the rapid drop in the D_α emission beginning at 0.82 seconds. The spikes in the D_α emission are type 3 ELMs. Note the rapid rise in the radiated power measured by the "2π bolometer" during the ELM-free periods.

by the "2π bolometer"[a] indicating an accumulation of impurities. By the end of the ELM-free period, the radiated power exceeds the applied RF power and approaches the total input power (typically the ohmic power is 1 to 1.5 MW). This high radiated power can not be sustained for long. ELMs starting at 0.85 reduce the radiated power, presumably by pumping out impurities. This radiation limited behavior is typical of operation during the spring '95 run period, with ELM-free periods during RF heating lasting 20 ms or less. This is shorter than the energy confinement time[b]. H-factors ($\tau_e/\tau_{ITER89-P}$) did not exceed 1.4 for any 5.3 tesla H-mode lasting on the order of an energy confinement time.

7.1.1 Edge Temperature Threshold

There is a strong correlation between the temperature measured at the plasma edge and the plasma state (L-mode, H-mode, or ELMy H-mode)[c]. Figure 7-2 shows the outermost channel of the GPC positioned 2 cm inside the LCFS during the shot discussed above. The sawtooth modulation of the edge temperature is evident. If a sawtooth raises the edge temperature above 400 eV, the plasma enters an H-mode, and below 320 eV the plasma returns to L-mode. Observing a GPC channel within a few centimeters of the LCFS shows this pattern in general. However, the exact location where the temperature needs to be a given value is still an area of research [67]. The decline in the edge temperature during the H-mode is due to an increase in radiated power (See Fig. 7-1). Note that the radiated power exceeds the input ICRF power after 20 ms in H-mode, causing the edge to cool and drop below the threshold power.

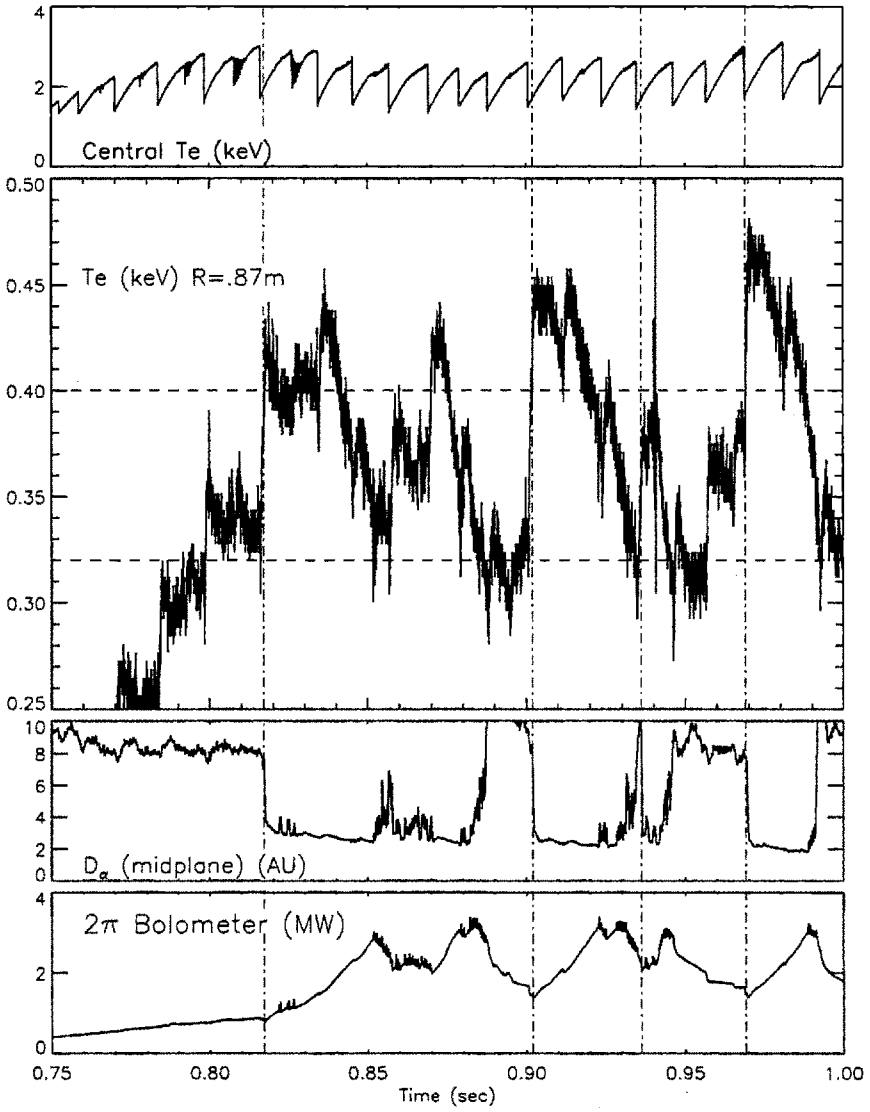

Figure 7-2: Edge Temperature Threshold shot 950602024. The dashed vertical lines indicate L-H transitions. Note that they are triggered by sawteeth and the temperature on the GPC channel at 87 cm needs to exceed ~400 eV for plasma to be ELM-free and must stay above 320 eV to remain in H-mode. Studies with the a GPC channel closer to the separatrix give values closer to 100 to 150 eV [67] as the threshold temperature near the LCFS.

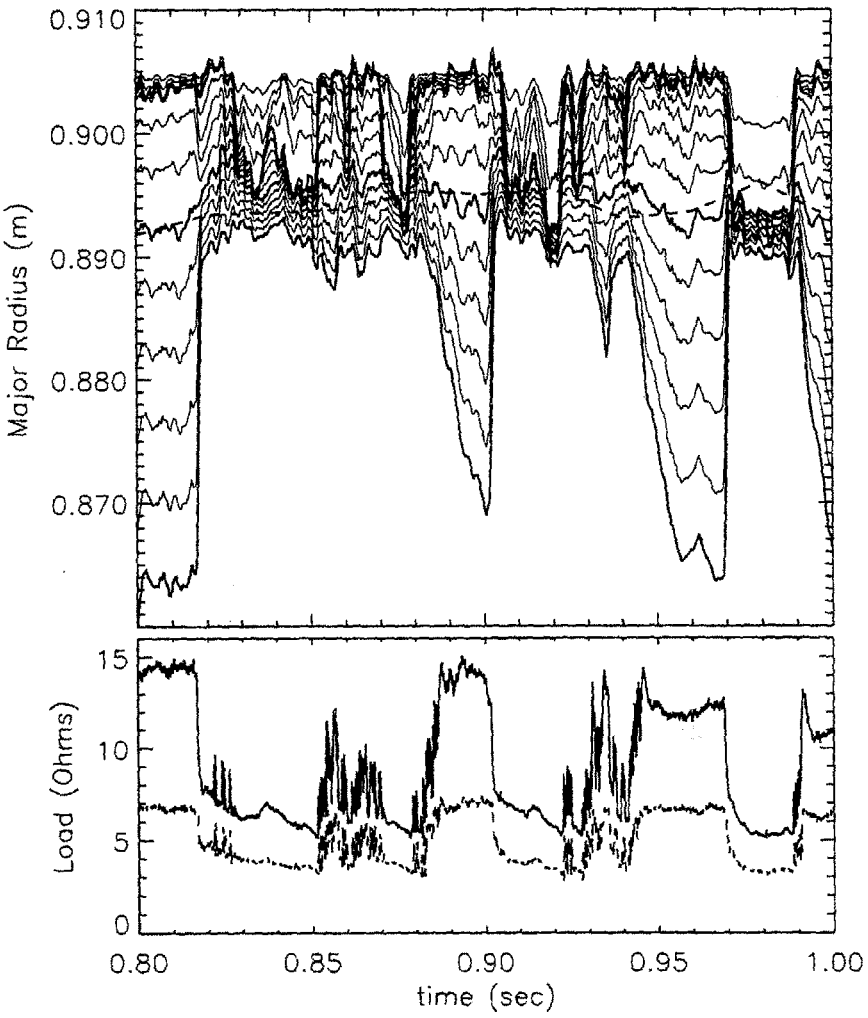

Figure 7-3: H-mode Profile and RF Coupling shot 950602024. The contour spacing is 10^{19} m^{-3} with the darker contours at 5, 10, and 15 $\times$ 10^{19} m^{-3}. The dashed line in the top plot is the LCFS. The lower plot is the real portion of the antenna loading. The solid line is for the D-port antenna and the dashed line is for the E-port antenna.

7.2 Electron Density Profile Evolution

Figure 7-3 shows the time evolution of the density profile during ICRF heating for shot 950602024. Note that the density gradient at the LCFS increases dramatically at the L-H transition. On the same time scale or slower, the density in the SOL drops leading to a density gradient[d] on the order of 2×10^{22} m^{-4}. The temperature profile measured by the GPC during one percent B_T scans also shows a steep gradient located very close to the LCFS with a scale length on the order of 0.7 cm [68]. The gradient during the ELMy period (ex. 0.865 seconds) is substantially less with the greatest change being in the SOL density. At an H-L transition the SOL density immediately increases while the profile inside the LCFS relaxes within 10 ms.

7.2.1 ICRF Loading

The loading to the ICRF antennas is strongly dependant on the SOL directly in front of the antenna. The cutoff density for the fast ion cyclotron waves for the $\mathbf{k}_{\|}$ spectra launched is $\sim 7 \times 10^{18}$ m^{-3}(see § 3.3.2). This is well below the cutoff density for the lowest frequency of the reflectometer (50 GHz, 3.1×10^{19} m^{-3}). The flux tube viewed by the reflectometer does not map directly to the region in front of the antennas and the antenna Faraday shield sits one centimeter behind the A-B limiter. Nonetheless, the loading should be expected to correlate somewhat with the lowest densities measured by the reflectometer. The drop in antenna loading during H-mode appears to correlate more with the formation of a steep gradient at the LCFS than the density near the limiter radius. This indicates that the SOL in front of the ICRF

[a]The 2π bolometer is a diode sensitive to X-ray and UV emission from the plasma. It does not provide as accurate a measurement of the emission as the bolometer arrays, however it has the fast time response needed for studying these rapidly changing plasmas.

[b]For shot 950602024 $\tau_e = W_{MHD}/(P_{ohmic} + P_{RF}) \approx 120$ kJ/4 MW = 30 ms

[c]This section is included as edge temperature thresholds are key to understanding C-Mod H-modes and the author contributed to its observation, though, of course the real credit belongs to Hubbard and O'Shea (see references).

[d]This value is at the limit of the reflectometer resolution, and the actual gradient may, in fact, be greater than this. This resolution is in part determined by observing the profiles calculated by the reflectometer during ELM free H-modes. On occasion, the group delay measurements will imply a multivalued density (see for example Fig. 7-10). The "overhang" is never greater than 0.5 cm, hence the assumed error bar.

antennas is substantially different than the SOL in front of the reflectometer horns. The sharp change in the density at the LCFS also contributes significantly to power reflection, or the turbulence, which is higher when the gradient at the LCFS is lower, increases transport to the region directly in front of the antenna (behind the poloidal limiters and the antenna limiters).

The low loading values during ELM-free H-modes limit the power that can be transmitted by the ICRH system. In addition, the sudden drops in loading at L-H transitions trigger temporary transmitter shutdowns because they are indistinguishable from arcs in the ICRF transmission lines or antennas. To ameliorate the deleterious effects of the drop in antenna loading at the L-H transition, radial position feedback on the ICRF loading was implemented beginning in November '95. The outer gap (the gap between the LCFS and the limiter) is controlled by the hybrid-computer (see page 42). Experimentally, the outer gap should be 1 to 2 cm to switch from L to H-mode. After the H-mode commences, this can be reduced to as little as 0.5 cm[e]. This motion is not enough to keep the loading at the L-mode level, but it is sufficient to keep the ICRF from tripping out [70]. Because of this motion, the density profile changes in the SOL are much less distinct after the implementation of radial position feedback.

7.2.2 Profile Transition Time Scale

The density rise inside the LCFS can be extremely fast. The transition at 0.97 seconds in Fig. 7-3 is an example of a fast transition with no ELMs. The density profile as measured by the reflectometer changes from an L to an H-mode profile in less than 0.5 milliseconds. Two possible issues present themselves. First, is the density profile monotonically decreasing as one travels from the plasma center to the edge? The 110 GHz channel may be reflecting off of a local maximum near the LCFS. Second, the the 110 GHz channel reflecting off of the SGR rather than the actual cutoff further

[e]Based on correlations with the divertor probes, during L-mode, EFIT calculates the LCFS contour to within a few millimeters, however during H-mode the limitations of the EFIT current model may increase this error to as much as a centimeter [69], so while the gap may be 0.5 cm according to EFIT, the actual gap may be closer to 1 cm.

in the plasma.

To determine if the density profile is monotonic, an approach is to compare the rise in the line integrated density to the increased inventory required to fill in the shaded region in Fig. 7-4. One question is whether the density profile is hollow in the region inside the SGR during the initial phase of the H-mode. The TCI indicates a very rapid rise in the line integrated density during the initial portion of the H-mode on shot 950602024 (see Fig. 7-1). However, for this shot the SOL density is also very high. Figure 7-5 shows a cross section of a similar plasma with the TCI chords overlaid. Note that all the TCI cords have long paths passing through the SOL (demarked by dashed contours) both above and below the main plasma. Also the density at the pivot point[f] is 10^{20} m^{-3}, so the density rise inside the LCFS that can be documented by the reflectometer is actually less than the drop in density outside the LCFS. As a result, the density rise inside the LCFS during the initial portion of the H-mode for shot 950602024 can be accounted for by a drop in the plasma inventory in the SOL.

Shot 950602028 is a lower density shot with virtually the same magnetic configuration as shot 950602024 and displaying the same radiation limited H-mode phenomena. Because the SOL density is lower on this shot, the interferometer can provide more information about the density rise inside the LCFS. Figure 7-4 shows the profile change between L and H-mode. The 110 GHz channel moves to its H-mode position 4 ms after the H-mode commences. During this time the interferometer channels one and four see a line integrated density rise of $4 \times 10^{18} m^{-2}$. Figure 7-5 shows how the reflectometer profile can be used to predict the interferometer measurements. Assuming a piecewise linear profile divided into 32 levels and assuming density is constant on a flux surface, a pathlength matrix can be constructed such that [nl] = [path length matrix]· [n]. Rows from the path length matrix for channels one and four are plotted in the upper left hand corner of Fig 7-5. Below that is the measured change in density predicted by the reflectometer assuming the density profile is not hollow. For r/a greater than 1.1, the reflectometer has no measurement, however for low density

[f]The pivot point it the location where the density remains constant during the L-H transition. This is typically very close to the LCFS. Outside the pivot point the density drops and inside the pivot point the density rises.

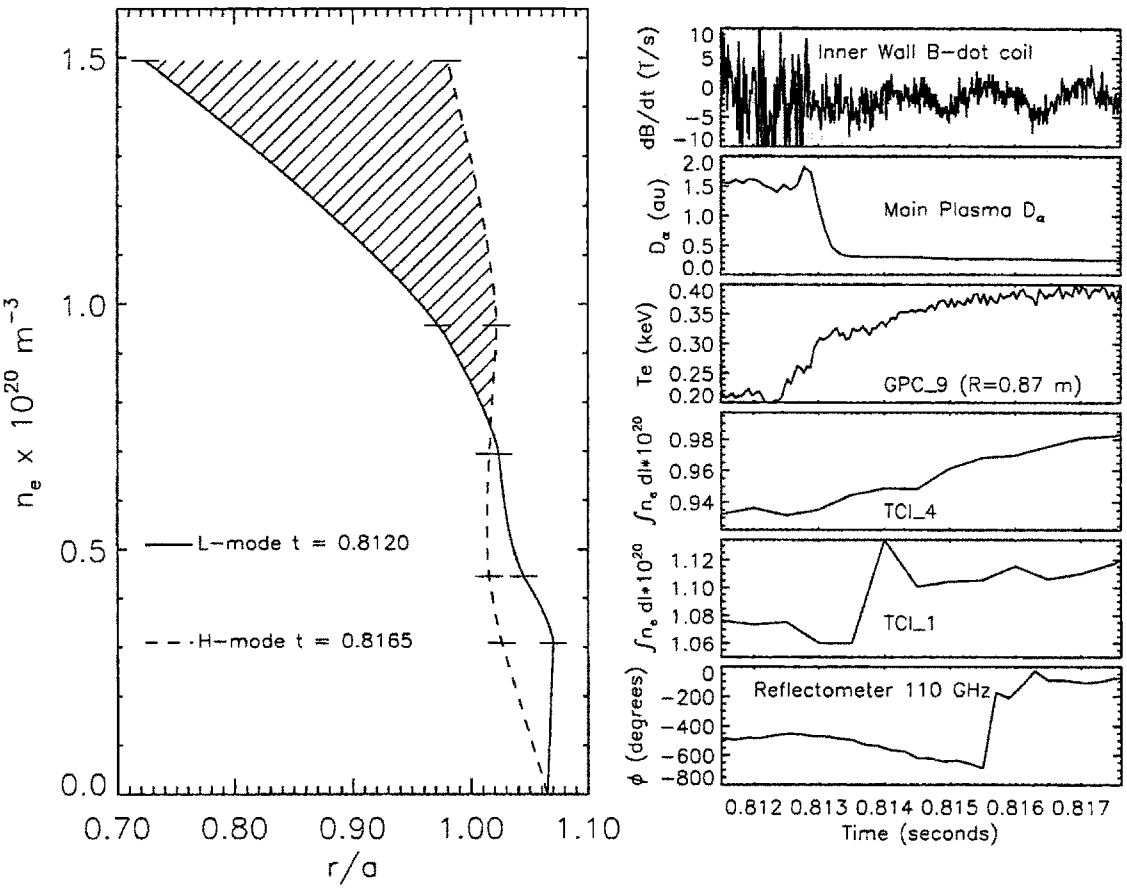

Figure 7-4: Rate of L-H Profile Change Shot 950602028 was a comparatively low density shot resulting in a rather slow ($\sim$ 4 ms) transition from an L-mode to an H-mode profile. The transition can be clearly seen on the inner wall magnetics and the main plasma D_α at 0.8129 seconds shortly following the arrival of a sawtooth heat pulse as seen by the edge GPC at 0.8125 seconds. The 110 GHz reflectometer channel assumes an H-mode value after 0.8165 seconds. The question is, is the shaded region filled in at this time.

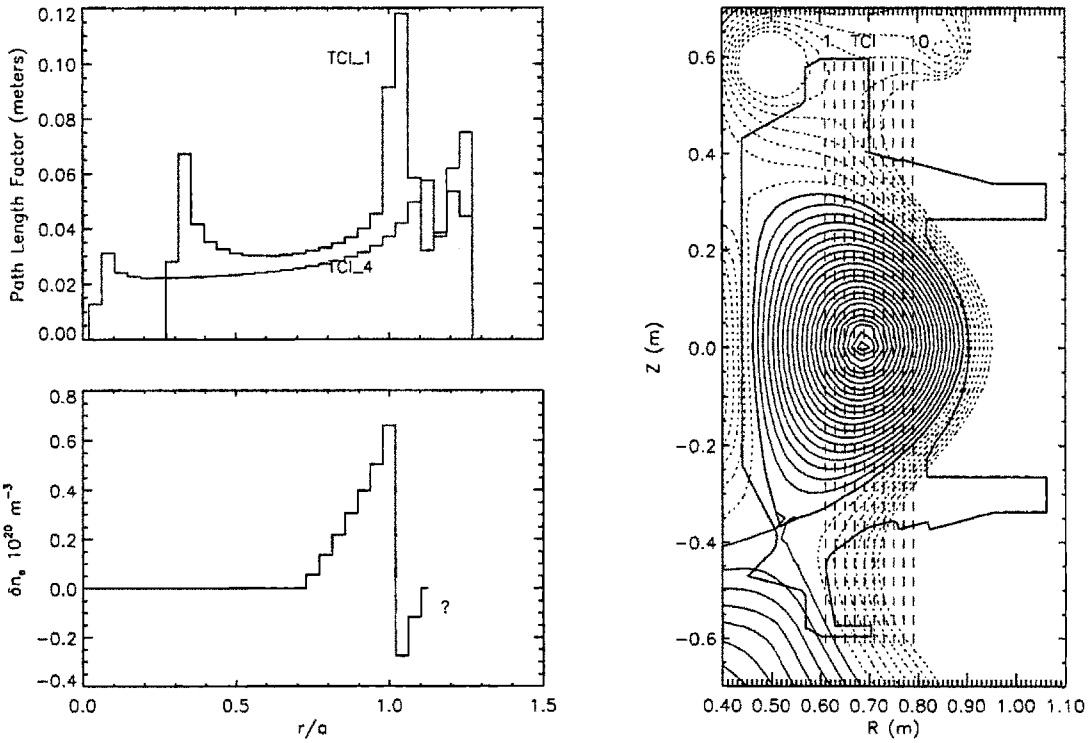

Figure 7-5: Modeling TCI Through L-H Transition shot 950602028 On the right is the equilibrium reconstruction showing the 32 contours of assumed constant density. In the upper left are the path length factors for each contour for channels one and four of the TCI. Below that is the change in density for each contour as measured by the reflectometer. At r/a greater than 1.1, the reflectometer has no measurements hence the question mark.

shots such as 950602028, the density outside the LCFS is expected to be small. The plot in the lower left corner shows the expected change in the line integrated density compared to the measured change. Based on these measurements the shaded region is not fully filled in at this time, 4 ms after the H-mode begins. This is however not unexpected. The plasma source is either neutrals in the main chamber being ionized in the plasma edge or plasma from the divertor and SOL being transported into the main plasma via some anomalous pinch. The second source is at the edge with some presumably narrow width dictated by edge transport issues. The neutrals entering the plasma will also be ionized near the LCFS[g]. The time scale discussed here is short relative to the 20 ms [71] particle confinement time for an L-mode plasma, so a local maximum near the LCFS might be expected.

Unfortunately the errors on the above calculations are large. The three largest sources of error are: the absolute calibration and inversion of the reflectometer ($\pm$2.5 mm in critical layer location), effective TCI chord location ($\pm$1 cm radially), and the density outside the limiter radius. The upper plot in Fig. 7-6 shows the change in density for a non monotonic profile (solid line). The dashed line is given by assuming that the L-mode reflectometer measured profile is displaced inward relative to the real profile and that the density outside the limiter radius is 0.15×10^{20} m^{-3} ,or half of the cutoff density for the lowest reflectometer frequency. During the H-mode the density outside the limiter radius is assumed to go to zero. This will give a lower bound on the change in the interferometer measurements required keep the H-mode profile monotonic. This is the lower line plotted in the lower curve. The starred line is the measured change in line integrated density and the upper curve is the measurements expected with the measured reflectometer profile with the density outside the limiter radius remaining constant during the L-H transition. Unfortunately, without a point density measurement, the errors in the reflectometer and the interferometer measurements due primarily to plasma outside the limiter radius.

[g]For a 100 eV plasma the electron impact ionization and charge exchange reaction rates are 3 and 3.75 $\times 10^{-8} cm^3/s$ respectively. Assuming an electron density of $10^{14} cm^{-3}$ and that the neutral deuterium atoms have the Frank-Condon energy of 3 eV, the neutrals will travel 0.25 cm before either ionizing or charge exchanging. Including multiple charge exchange events broadens the source somewhat, but it is still limited to 1.5 cm from the plasma edge.

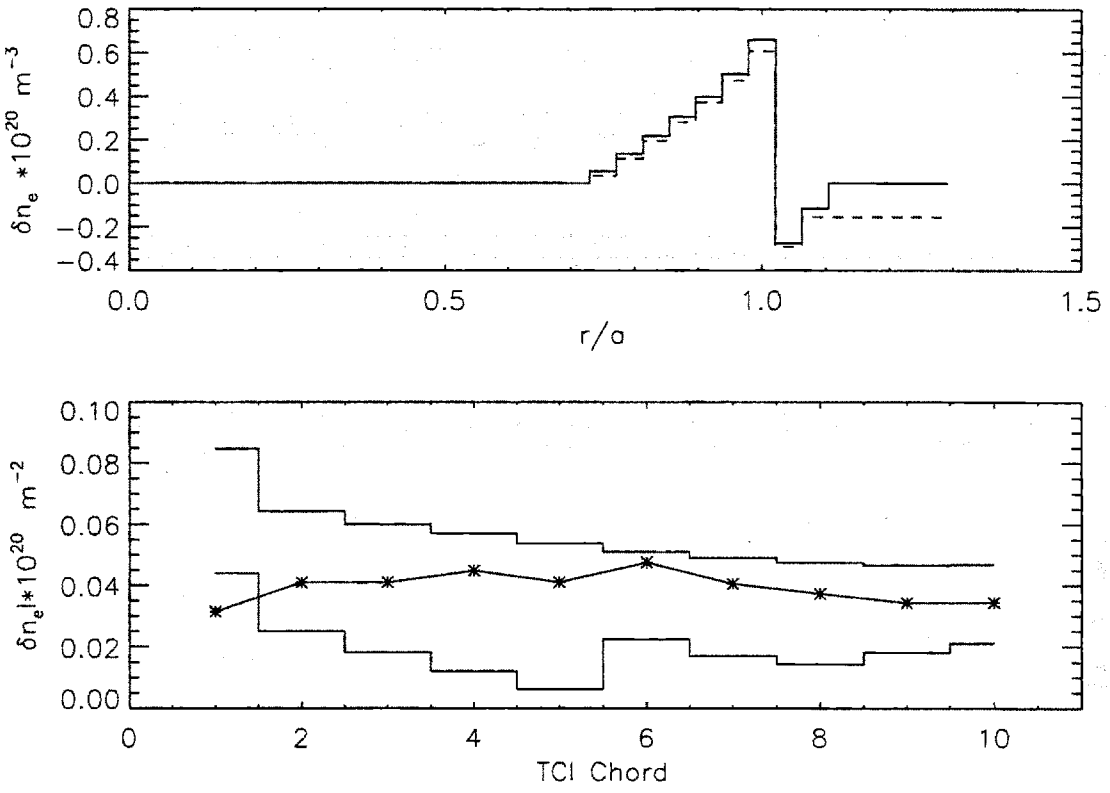

Figure 7-6: Modeling TCI Through L-H Transition (part2).
Please see text for explanation.

7.3 Fluctuation Suppression During H-mode

As was discussed in § 2.6, the anomalous transport of particles and energy in tokamak plasmas is believed to be due to microinstabilities driven by gradients in constituent temperature and/or density. The nature of these instabilities is poorly diagnosed and hence poorly understood. During an H-mode, a transport barrier forms near the LCFS. On other tokamaks, very high rotation velocities have been measured near the LCFS, leading to the hypothesis that a radially sheared velocity profile near the LCFS suppresses the microinstabilities or decorrelates them sufficiently to allow a large pressure gradient to form. The reflectometer is an excellent qualitative tool for studying this fluctuation suppression region or FSR because of its high sensitivity to fluctuations and good radial spatial resolution.

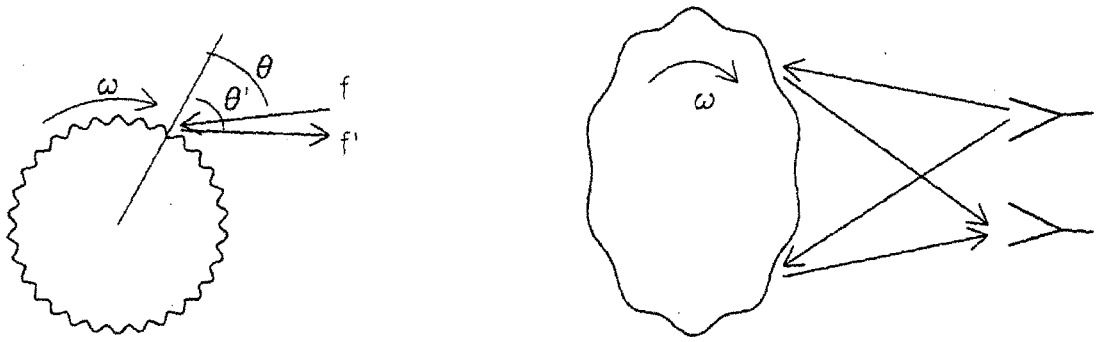

Figure 7-7: Model of Scattering from a Rotating Mode. The figure on the left shows a Doppler wheel as used in a heterodyne interferometer. A mode rotating in a plasma can give the same upsift in a reflectometer.

7.3.1 Note on Fluctuation Measurements

The study of plasma fluctuations via reflectometry is not straightforward and was not intended to be the main focus of this thesis. Unlike collective Thomson scattering or magnetic diagnostics, the frequency and amplitude of the returned phase does not directly correlate with the motion of the plasma. The first issue is plasma rotation. A good analogy is the Doppler wheel often used in heterodyne interferometry [38, 72] (see Fig. 7-7). The upshifted frequency is:

$$f' = f \times \left(\frac{1 + \frac{\omega r}{c} \sin\theta}{1 - \frac{\omega r}{c} \sin\theta'} \right)$$

The angle and power of the upshifted beam is determined by the line spacing on the wheel and the blaze of the grating. A plasma has perturbations that travel on a flux surface in just such a fashion. A rotating metallic drum with some dents can easily produce the Doppler wheel effect in a reflectometer mockup. (Without the dents no Doppler shift is seen.) Nazikian [73] demonstrated this effect on TFTR. Continuing the analogy, the blaze and the spacing of the waves in a tokamak plasma are not givens, but the quantities one would hope to infer. Note that as a result

the frequency spectra seen by a reflectometer may not be the same as seen by other diagnostics such as magnetics. A further complication is the sensitivity to a given $\delta n/n$ is higher as n approaches n_c, so the slope of the profile near the cutoff can greatly affect the sensitivity to fluctuations. This is particularly an issue for studying fluctuation levels during L-H transitions when the gradients vary greatly.

In addition there are several problems unique to the C-Mod system. The intention of the differential phase arrangement is to reduce the effects of fluctuations on the group delay measurement. Fluctuations that appear coherently on both side bands are largely subtracted out. The incoherent portions are not. This effectively amplifies fading and power reflected from the edges of the beam pattern over the fluctuations directly in front of the horn. In addition, the limiting amps that are required to make reliable phase measurements of the beat wave, will produce harmonics of any fluctuation signals. With these caveats, the reflectometer typically sees a rather featureless fluctuation spectra with a slow decay out to the filter cutoff frequency of 416 kHz. The amplitude of the fluctuations does change dramatically depending on the plasma state.

7.3.2 Rate of Fluctuation Suppression at L-H Transition

Figure 7-8 shows the suppression of fluctuations at an L-H transition. The diagnostic that shows the transition first in low density plasmas is the magnetics on the inner wall (second plot from the bottom). At 0.908625 seconds the fluctuations are suppressed. On the reflectometer (third plot from the bottom), the transition is less clear, but has certainly occurred by 0.90865 seconds. Also, the average phase of the returned wave remains at the L-mode position for 50 μs after the fluctuation level has dropped. This implies that the profile near the reflecting layer has not changed. So while some of the observed drop in the fluctuations during an H-mode seen by the reflectometer can be attributed to an increase in the gradient near the reflecting layer reducing the reflectometer sensitivity to some $\delta n/n$, the amplitude of the fluctuations also drops.

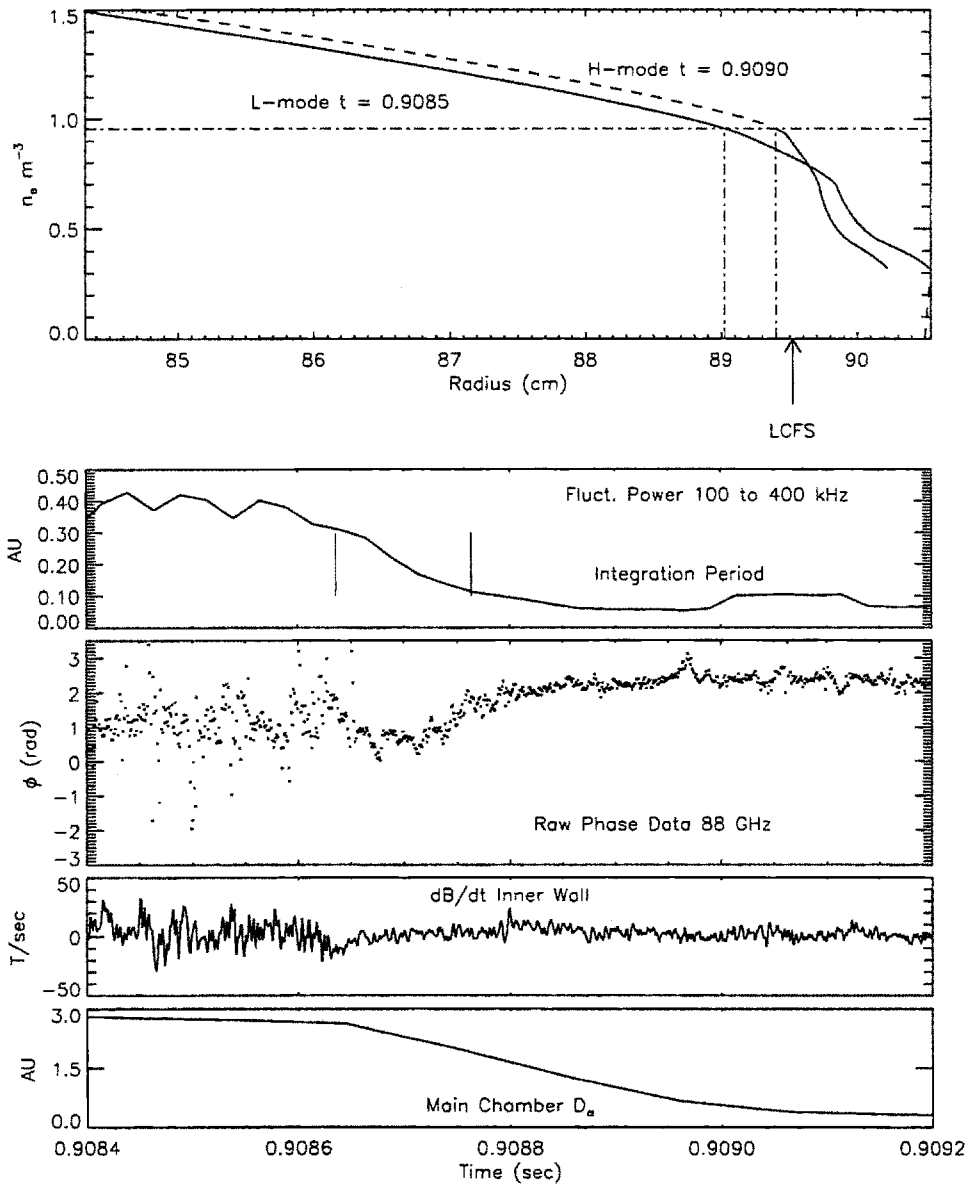

Figure 7-8: Fluctuation Suppression Viewed by Reflectometer Channel Initially in FSR. Shot 950602028. The 88 GHz reflecting layer is within 0.6 cm of the LCFS prior to the H-mode and remains in the FSR. The transition can be seen on the magnetics at about 0.908625 seconds. The fluctuations on the reflectometer drop within 25μs of the transition.

7.3.3 Transport Barrier Width

The fluctuation level as observed by the reflectometer drops dramatically during most H-modes. Figure 7-8 shows how the fluctuations drop quickly for a channel cut off near the LCFS in the L-mode phase prior to the H-mode. However, the drop in fluctuations is limited to a region near the LCFS. Figure 7-9 shows shot 950602024 again[h]. The main chamber and one channel from the divertor D_α array are shown in the top two plots. The divertor D_α channel views the region near the inner nose of the divertor. The D_α views elsewhere drop coincident with the L-H transition. Only after the divertor D_α emission and the SOL layer density drops does the fluctuation level on the 75 GHz channel drop.

The FSR appears to be limited on the outside to 0.5 cm of the LCFS. The extent of the FSR into the main plasma is more difficult to measure with reflectometry. For virtually all ELM-free H-modes, all 5 channels of the reflectometer are reflected in the SGR or at larger major radius within 500 μs of the transition. However for very low initial density H-modes, the change in the electron density profile is slow enough to allow for a brief study of the fluctuation level inside the main plasma after the H-mode commences. Shot 950602019 was the lowest density shot to achieve ELM-free H-modes on this day[i]. Figure 7-10 shows the first 1.5 ms of an H-mode during this shot. At 0.8614 seconds, the fluctuation level measured by the magnetics on the inner wall drops and is followed shortly by a drop in the D_α emission (see lower two plots). The phase signal measured with a 400 kHz bandwidth is shown in the middle trace. Notice that the fluctuation level drops dramatically at 0.86205 seconds, 650 μs after the start of the H-mode. The power in the band from 100 kHz to 400 kHz integrated over 128 μs is displayed above the raw phase data. For at least the initial 300 μs of the H-mode, the fluctuation level does not change significantly and the average phase stays constant. The fluctuation level increases at 0.8618 seconds as the cutoff moves

[h]It should be pointed out that this shot has a rather high lower triangularity (same shape as shown in Fig. 7-5) and a slot divertor, however the fluctuation phenomena are not unique to this magnetic configuration.

[i]At lower densities Z-effective is higher, so more power is radiated. This shot stays in H-mode for only 5 ms before returning to L-mode due to radiative energy losses.

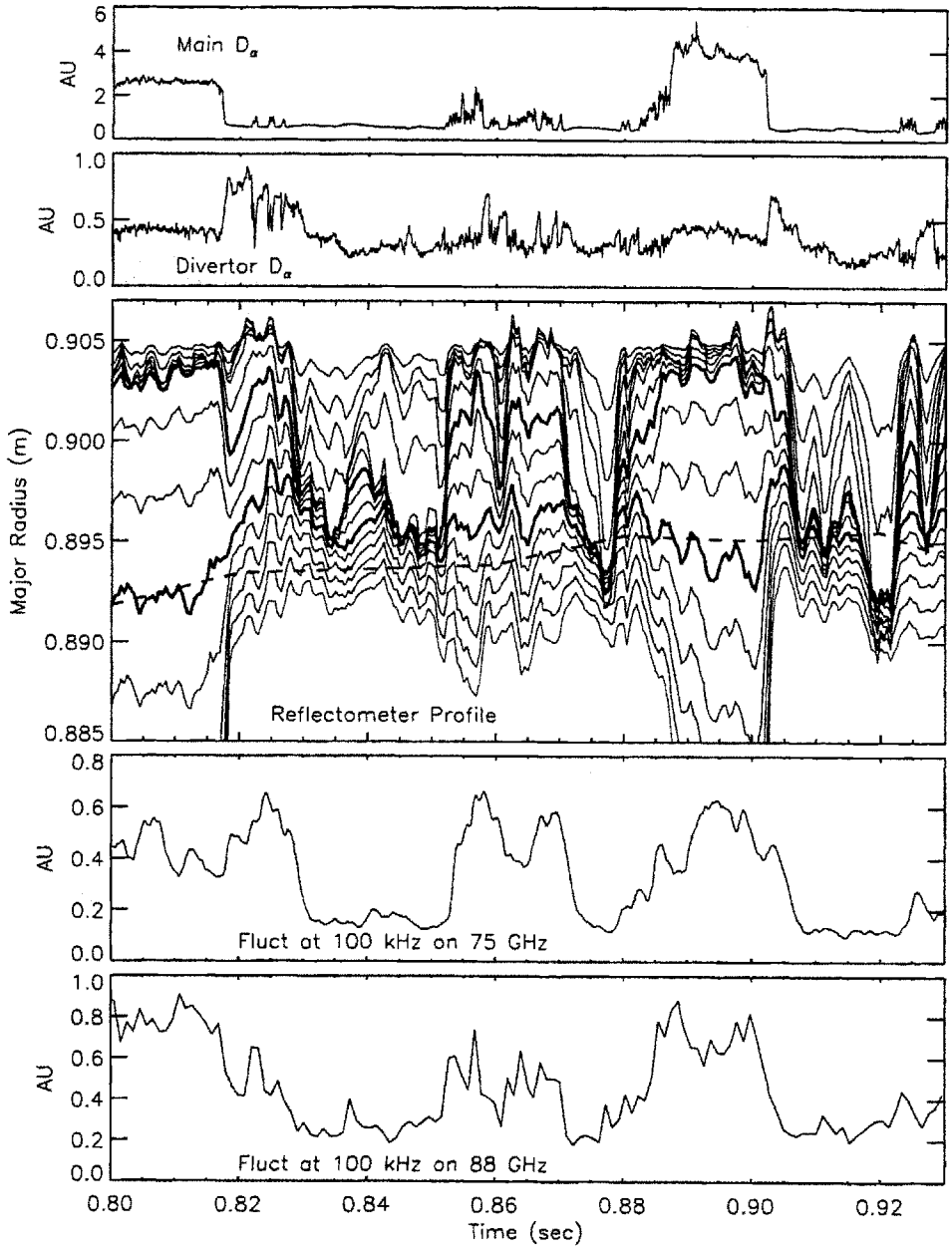

Figure 7-9: Outer Limit of Fluctuation Suppression Region During H-mode. Shot 950602024. The H-mode can be seen to start at 0.817 seconds, however the fluctuations on the 75 GHz channel begin to drop only after the 75 GHz cutoff layer moves into the SGR and the divertor D_α begins to drop at 0.83 seconds.

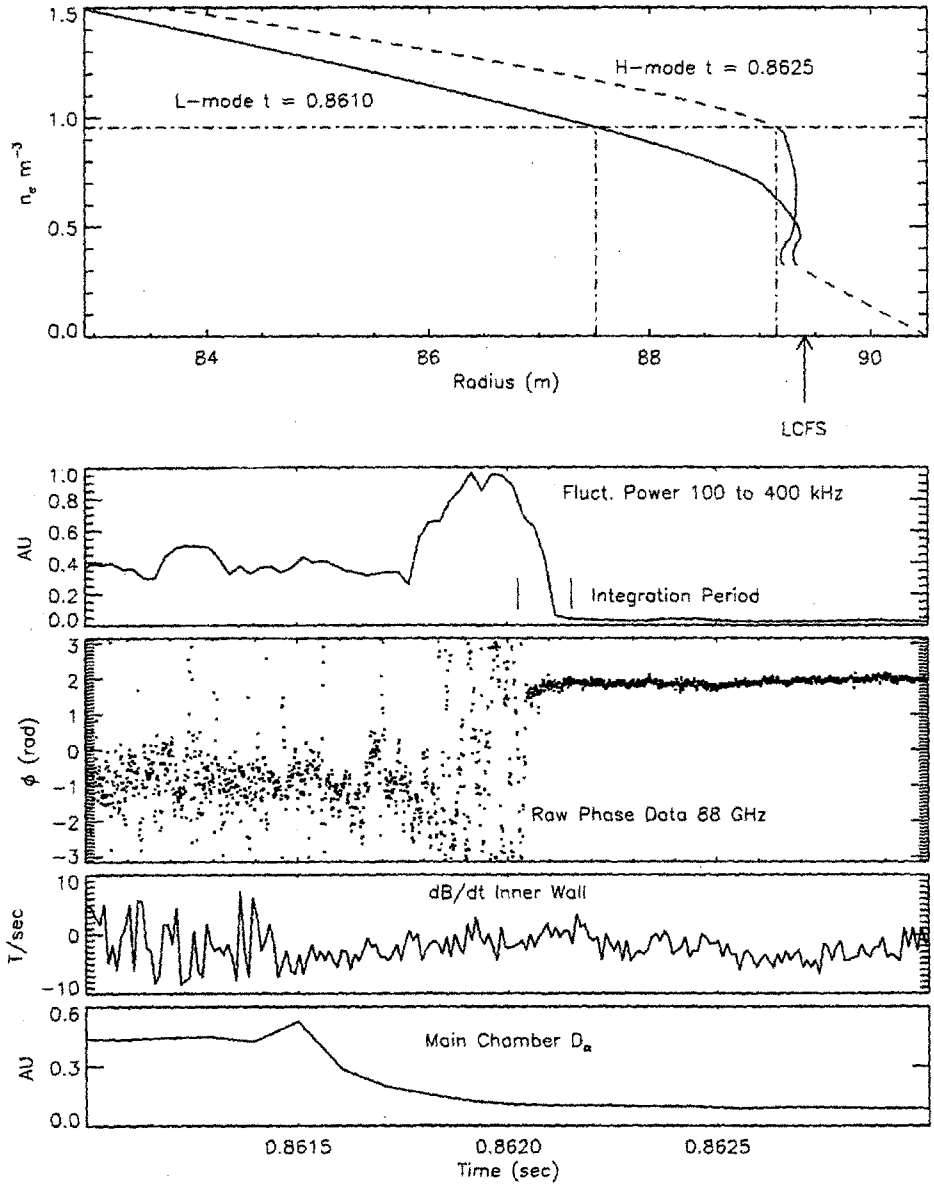

Figure 7-10: Inner Limit of Radial Extent of Fluctuation Suppression Region Shot 950602019. The H-mode starts at 0.8614 seconds as witnessed by the magnetics. The fluctuations observed by the reflectometer remain constant until 0.86175 seconds, indicating that the FSR does not extend 1.5 cm inside the LCFS during the initial 300 μs of the H-mode.

from the L-mode to the H-mode position. This is to be expected as the profile near the cutoff is flatter or nonmonotonic during this period

The profiles both before and after the L-H transition are shown in the top figure[j]. The 88 GHz cutoff density is shown with the horizontal dashed line. The cutoff location moves from 0.874 to 0.892 meters between 0.8618 and 0.8621 seconds. For at least the first 300 μs the FSR extends less than 1.8 cm inside the LCFS.

With an O-mode reflectometer, this approach of measuring the FSR width is very limited. A channel cutoff inside the plasma before the L-H transition generally changes to being cutoff in the SGR some time after the L-H transition with a discontinuous jump. With the planned divertor cryo-pump, the density rise during ELM-free H-modes may be controlled sufficiently to keep the density in the SGR below the critical density of the highest reflectometer channel. An X-mode reflectometer using the RHC on a machine where $\omega_{pe}/\omega_{ce} \ll 1$ would have more success with this measurement as the location of the cutoff is not as dependent on the density profile.

7.4 Enhanced D_α H-modes

7.4.1 Post-Boronization

In January of 1996, the machine walls were "boronized" [74, 75] (coated with boron via plasma deposition). This greatly reduced the rate of high Z impurity accumulation in H-mode plasmas and allowed H-factors of 2.5 to be reached in ELM-free plasmas. Figure 7-11 shows a "trophy" shot from an impurity confinement study during this period. The rise in the radiated power beginning at 0.7 seconds is due to an intentional impurity injection (scandium). This shot demonstrates a very long confinement time for impurities in ELM-free plasmas $\sim$ 1 second [76]. After 0.86 seconds the D_α light

[j]The H-mode profile between the 88 and 110 GHz cutoffs is shown as a dashed line because during this transient phase, there may be far more structure in the profile than the reflectometer can resolve. The group delay for the 110 GHz channel actually increases during the H-mode. However on the 1 ms time scale, the profile at 0.83 meters (r/a = 0.7) probably does not change. The profile reconstruction routine, however, does not take this into account. The actual profile is expected to be somewhat higher than shown in the few cm inside the LCFS and closer to the L-mode level near 0.84 meters.

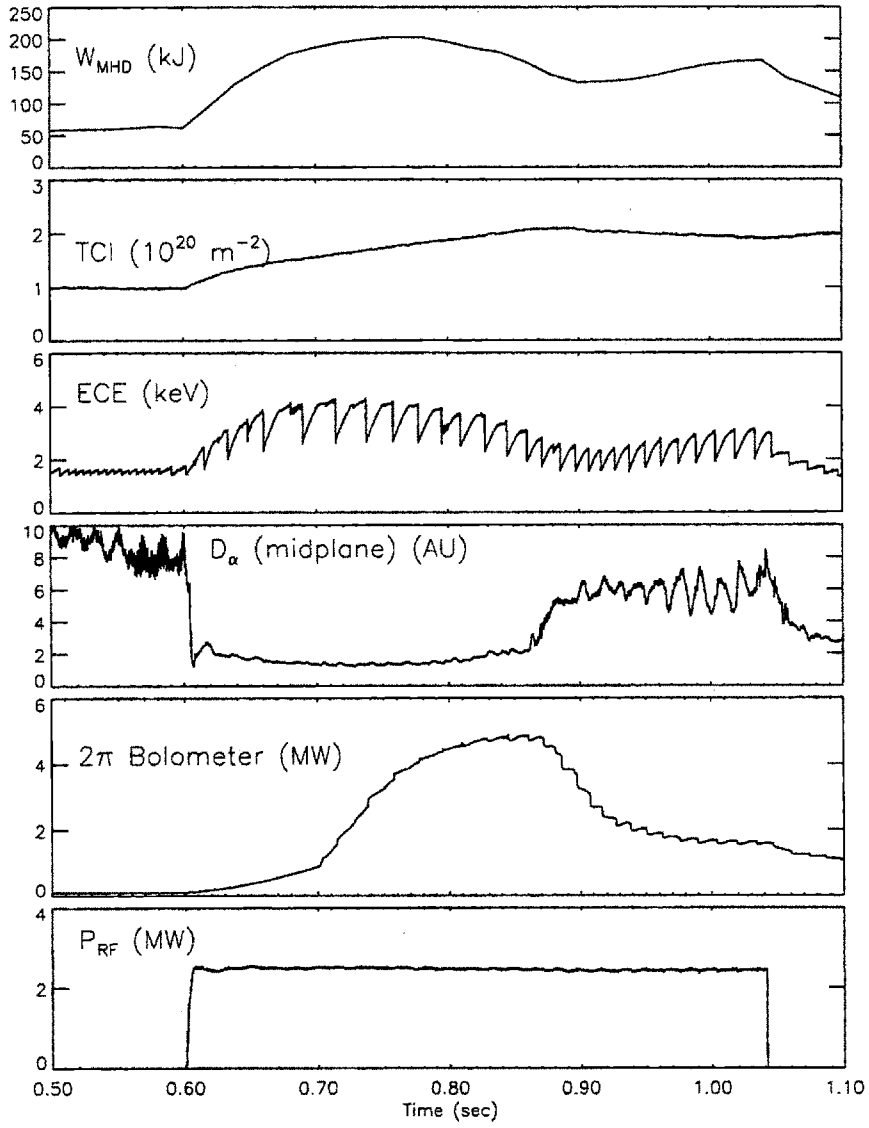

Figure 7-11: ELM-free and EDA H-mode. shot 960214030 The plasma is in an ELM-free H-mode from 0.6 to 0.86 seconds. At 0.7 seconds, scandium is injected which accelerates the rise in impurity radiation. After 0.86 seconds the plasma enters an Enhanced D_α phase. Impurity confinement is greatly reduced as witnessed by the drop in radiated power as seen by the 2π bolometer decays away. Also the TCI shows that the plasma inventory stabilizes.

rises and the radiation measured by the bolometer decays. Impurity confinement drops to ~ 0.1 second [76] and the stored energy increases modestly. Very occasional isolated ELMs have been observed during the period of elevated D_α emission, but none that have the periodicity of type three ELMs often seen during ohmic H-modes, nor do they have a significant effect on the stored energy that one would expect from type 1 ELMs. One possibility is that the emission we see is due to "grassy" ELMs[k] that are too fast for the C-Mod diagnostics to observe or the response time of the C-Mod SOL is long compared to the ELM period. Magnetic fluctuations are often seen during these Enhanced D_α (EDA)[l] H-modes [77] at typically 65 kHz, however they saturate in amplitude rather than showing the exponential growth characteristic of ELM precursors.

Since boronizing the machine walls, such EDA H-modes have become quite common. They present a very promising mode of operation for future fusion reactors as their energy confinement time is quite high (H-factor ~ 2) yet the particle confinement is greatly reduced from that of an ELM-free H-mode (see § 2.6.3). These are effectively steady state H-modes with their duration dictated by operational issues, in contrast to the H-modes from the spring '95 run whose duration were limited by high radiated power due to impurity accumulation.

The reflectometer was handicapped during this run period due to two problems. The first was a failure of a mixer in the 110 GHz system. The second was a change in the interaction between the SOL and the limiter radius. In general, the steep gradient previously seen at the limiter radius was not observed after boronization, except during strong impurity puffing. The assumption is that the higher edge temperatures seen after boronizing resulted in a narrower SOL. As a result the calibration technique presented in § 6.3 was in general not available. However, shot 960214030 provides a an opportunity to compare uncallibrated data from an ELM free H-mode and an

[k]Grassy ELMs have been observed to have many of the same qualities as the EDA H-modes in that they reduce particle confinement without reducing the energy confinement greatly.

[l]The name for this type of plasma has changed with each conference in the last year. They have also been called as Enhanced Recycling H-modes or High Recycling H-modes. The publication of this thesis with the Enhanced D_α name and EDA acronym should end any controversy on this subject.

EDA H-mode. Figure 7-12 displays the 60 to 88 GHz channels for this shot. Notice that after the H-mode commences at 0.61 seconds, there is very little variation in the group delay even when the plasma enters the EDA phase at .87 seconds. In addition, the loading on the antennas does not change significantly, also indicating that the decay lengths in the SOL are not changing dramatically. The position feedback on the loading is on at this time which will tend to stabilize the loading, however the position of the LCFS changes only 2 millimeters during this period. The pedestal height for this shot is on the order of 3×10^{20} m^3, so these measurements only indicate that the SOL and the lower third of the SGR are still in an H-mode state in an EDA H-mode.

During EDA H-modes, the fluctuation level observed by the reflectometer increases dramatically (see Fig. 7-13). The frequency spectrum of the observed fluctuations is quite broad out to 400 kHz (the cutoff frequency of the anti-aliasing filter). There is a broad peak typically between 100 and 150 kHz. During EDA H-modes is one of the few occasions when the fluctuations observed by the reflectometer show any significant features. This peak has only been observed during EDA H-modes and all occasions when the fast sampling window is positioned during an EDA H-mode, a peak in the spectra has been observed. Comparisons between the reflectometer and the magnetics have not shown any significant correlation [78]. The frequency of the peak in the spectra is on occasion modulated by the sawteeth as shown in Fig. 7-14.

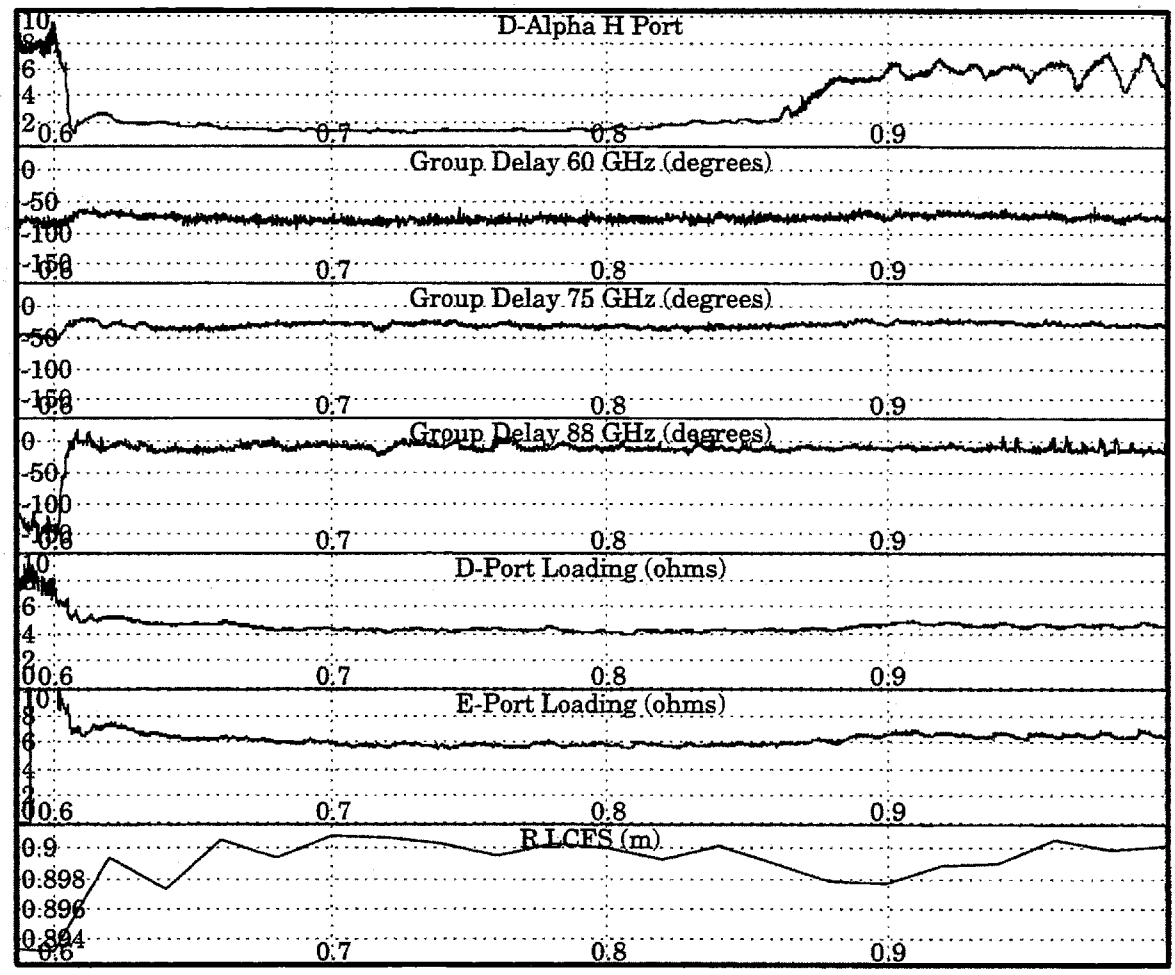

Figure 7-12: ELM-free and EDA H-mode (part 2). shot 960214030 Note that the reflectometer group delays and the loading on the antennas do not changesignificantly at the transition from ELM-free to EDA H-mode, indicating that the SOL density profile change is limited.

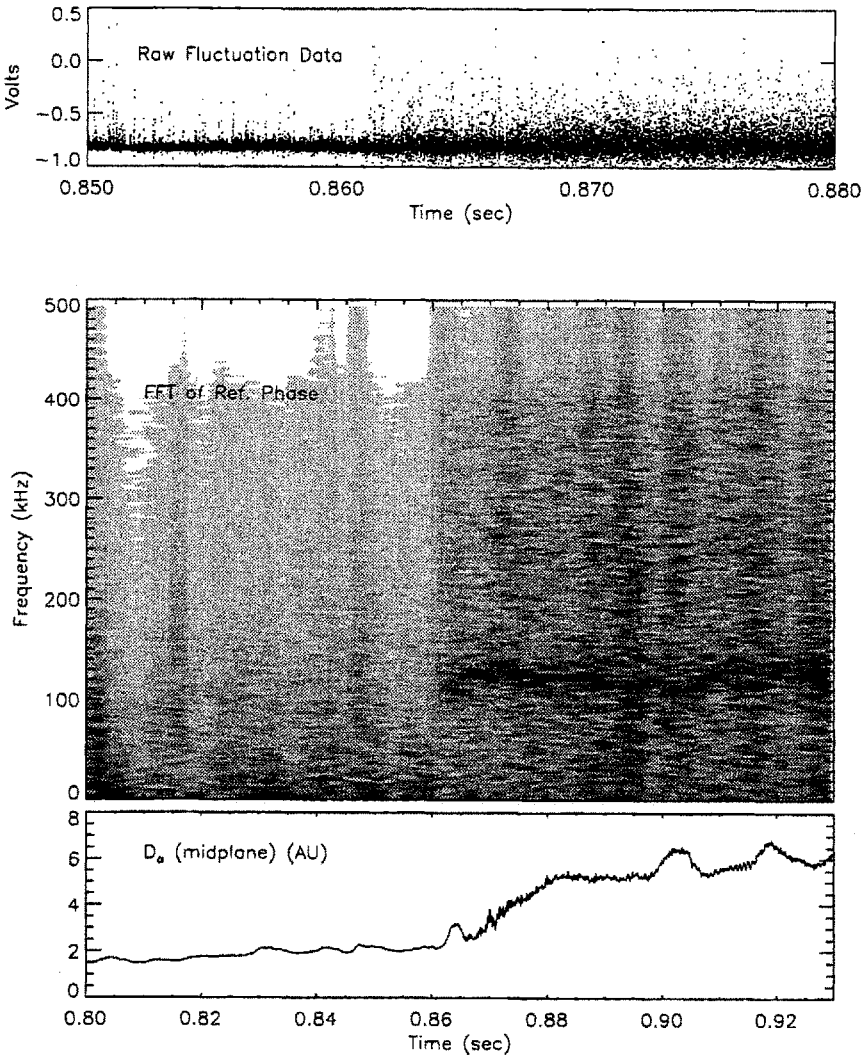

Figure 7-13: FFT of Fluctuations During EDA H-mode shot 960214030 The darker the region, the higher the absolute magnitude of the FFT. Note that the D_α emission increases coincident with the rise in the total fluctuation level and the peak at 125 kHz. Above the contour plot, one channel of the raw data is presented. (Note the different time base.)

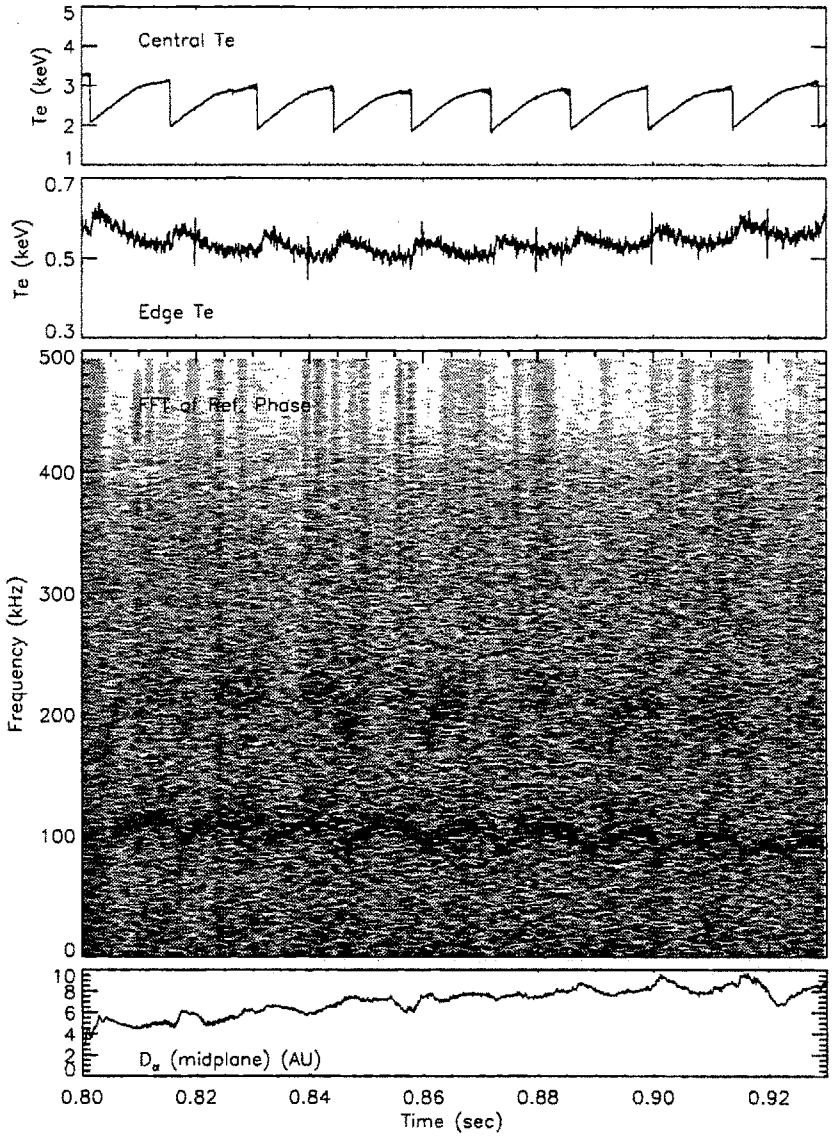

Figure 7-14: EDA H-mode Fluctuation Frequency modulated by Sawteeth. In this contour plot of the amplitude of the Fourier transform of the fast signal from the 88 GHz channel, the modulation of the peak frequency can be seen. The spikes in the edge ECE signal at 0.02 second intervals are instrumental.

Chapter 8

Conclusions and Future Work

8.1 Conclusions

Multi-channel, differential phase reflectometry can provide very accurate electron density profiles with, depending on plasma conditions, fraction of a millisecond time response. However, calibration remains a significant challenge due presumably to multiple reflections in the vacuum chamber before and after a plasma. By calibrating the reflectometer channels via observed features in the density profile, profile reconstructions with accuracy of approximately 0.5 cm have been obtained that agree well with many diagnostics, though not with the TCI. It is believed that the discrepancy between the reflectometer and the TCI can be at least in part attributed to inadequately modeled high density plasma outside the LCFS. Fluctuation measurements with a differential phase reflectometer, though qualitatively useful, are not well suited to quantitative fluctuation measurements. However, as will be shown in the following section, some comparatively simple additions to the basic DP receiver will allow for fluctuation studies using individual sidebands. A comparison of the capabilities of the three main electron density diagnostics is presented in table 8.1.

Density profiles during many phases of C-Mode plasma operation have been measured using the differential phase reflectometer. L-H transitions have proven particularly interesting with density gradients of 2×10^{22} m^{-4} measured 0.5 ms after an L-H transition. This rapid rise in plasma inventory is in rough agreement with measure-

	Interferometry	Thomson Scattering	Reflectometry
Profile reconstruction	moderate	excellent	good
Component durability	good	moderate	good
Usefulness for feedback control	excellent	bad	bad
Ease of analysis and availability of data	excellent	good	poor (could be good)
Cost	moderate to high	very high	moderate to high
Dynamic range	good	excellent	poor
Maintenance	high	very high	high (could be low)
Ease of calibration	excellent	poor	poor (could be high)
Time response	excellent	poor	excellent
Edge profile diagnosis	poor	moderate (could be excellent)	good (could be excellent)
Fluctuation diagnosis	moderate (good central poor edge)	very poor	good

Table 8.1: Electron Density Diagnostic Comparison (for 1995 run)

ments from the TCI, however for brief periods after the L-H transition a locally hollow density profile probably exists. At the L-H transition the fluctuation level measured by the reflectometer drops dramatically for channels reflecting in a 1 cm the region extending from the LCFS inward. The rapid density rise inside the LCFS following the L-H transition prevents one from making these fluctuation measurements after the first few milliseconds of the H-mode.

8.2 Future Reflectometry Work

The success of this thesis and the need for more detailed knowledge of the electron density profile in C-Mod warrant an aggressive approach to further reflectometry development[a]. However, the current funding and manpower shortages on the C-Mod experiment place a limit on what experiments can be done. The following actions are recommended, assuming the current staffing arrangement[b] and the continued interest in studies of enhanced confinement modes of operation.

8.2.1 Reliability Improvement and Maintenance Reduction

The reflectometer was developed as an experimental diagnostic and as a graduate student thesis project. As might be expected some aspects bear the shortcomings of an initially less than polished design and many late night modifications. The wiring and hardware are currently being streamlined by a graduate student and a staff engineer. In addition to general straightening up of the experimental rack several upgrades are needed. The Gunn oscillators should be stabilized such that their IF drifts less than 1 MHz. This will reduce the need to tune the system in the morning before each run day and is essential for the instrumentation described in § 8.2.6 for fluctuation diagnosis. The mica vacuum windows should be replaced with a more rugged design. Quite probably a simple glass window will suffice though the transmission needs to be tested. At the same time, an improved technique should be developed for installing and removing the waveguides from the narrow reentrant vacuum port. In addition, all other experiments using triggers from the reflectometer CAMAC crate should receive their trigger through a fiber rather than direct cable connection to reduce the possibility of damage to sensitive equipment due to ground loops.

The analysis software can benefit from similar attention. In particular, data reduction and profile inversion requires far more operator input in fringe jump detection

[a]This section is intended not only as a the author's suggestion of how to develop reflectometry, but also as a memo to the C-Mod scientific staff regarding what work is needed for the diagnostic's continued use on C-Mod.

[b]A single graduate student working under the guidance of a staff scientist with occasional help from the engineering and technical staff

than it should. The author will attempt the software upgrades some time after this thesis is complete to simplify this process. Also, dropping the upconversion frequency from 500 to 350 MHz could significantly simplify the the fringe jump correction routine. This upgrade is also needed for following PEP mode profile evolution.

8.2.2 Calibration and Profile Reconstruction

Probably the biggest issue with the current system is the difficulty in calibrating the diagnostic. A movable calibration plate mounted on a rod such that it can be moved radially should do much to alleviate this problem. Figure 8-1 is a sketch of the proposed calibration assembly. Also, installing absorbing structures on both sides of A-port would reduce the multiple reflections that are assumed to be the cause of calibration difficulties. These upgrades should allow improvement in the reliability and accuracy of the diagnostic. However, obtaining scale length measurements on the order of 1 mm as is desired for studying balooning mode stability limits during H-modes, for example, is probably beyond the capabilities of the diagnostic as currently configured. Resolution of that range will require greater care with respect to amplitude to phase modulation, the beam patterns of the launching horns, and the ray tracing of the launched waves.

8.2.3 Cross Calibration Profile

As has been stated before, the other density diagnostics also have serious shortcomings and strengths. The Thomson scattering diagnostic in particular is difficult to keep calibrated between shutdowns. However, TS is the only diagnostic with the potential resolution and dynamic range currently requested. Standard C-Mod operation calls for one or two "fiducial" shots per run day. These have a standard set of control inputs and are intended to monitor the day-to-day condition of the machine walls by monitoring impurity levels, radiated power fraction, and L to H transition thresholds. A similar fiducial for diagnostic cross calibration would also be useful. In particular, a slow ramp in the electron inventory through a central density of 1.5×10^{20} m^{-3}

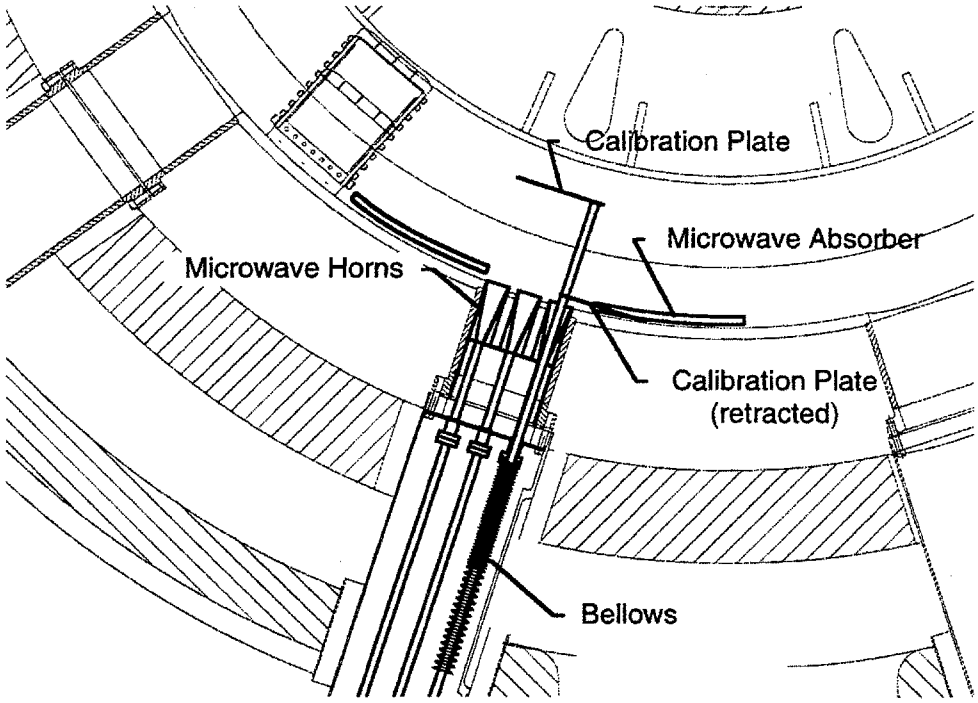

Figure 8-1: Proposed Calibration Paddle

would allow for an accurate cross calibration between the Thomson scattering and the reflectometer. This should be performed in L-mode at low to modest current to ensure that the density profile is peaked on axis and that the sawteeth are small. The ramp in density must be slow enough to allow for sufficient laser pulses to minimize the random error in the Thomson scattering measurement due to photon statistics. It is expected that a diagnostic fiducial can either be incorporated into the current fiducial shot or be performed on a weekly or bi-weekly basis so as not to overburden the run schedule.

In addition, there exists a significant gap in the reflectometer density coverage between 0.95 and 1.5 $\times$ $10^{20}m^{-3}$ (88 and 110 GHz) that compromises the profile inversion of the reflectometer. For this calibration scheme to be accurate to 5%, at least one more frequency is needed. This can be accomplished by adding a complete channel (both millimeter and rf components) at 100 GHz or by applying the technique suggested in § 8.2.5. Either of these will require substantial funds ($\sim$ \$10,000 to \$20,000), however, a robust TS calibration technique is well worth this expense.

8.2.4 X-Mode Polarization

The least expensive option to extend the density range of the reflectometer is to rotate the polarization to X-mode and study the group delay to the LHC. This approach will allow for access central densities of $4.5 \times 10^{20}\mathrm{m}^{-3}$ at 7.9 tesla using the frequencies we currently have available (see Fig. 4-7). This should be particularly interesting for PEP mode studies. For 5.3 tesla H-modes, pedestal heights up to 2.3×10^{20} m^{-3} can be studied (see Fig. 4-5). This is a 50% increase over current capabilities and will allow the diagnostic to see beyond the SGR for some H-mode shots. However, pedestal heights of 3.5×10^{20} m^{-3} have been measured by ECE cutoff, so for many if not most H-modes the problem of only being able to probe to the SGR will probably continue. In addition, there are some complications that need to be addressed. First, along the way to the X-mode cutoff, the beam will have to pass the O-mode cutoff. Because the O-mode cutoff comes first, signal reflected from this cutoff has the potential to corrupt the group delay measurements far more than the X-mode cutoff can corrupt our current O-mode measurements. The current horns do not allow for adjustment of the launch angle to match the field pitch at the plasma boundary. A set of scalar horns would allow for this rotation based on the expected current and toroidal field for the day's experiments. Getting the polarization correct for all shots during a run will probably be impossible. However, it may be possible to estimate the fraction of the power going into each mode by observing the cutoffs during the plasma ramp up and ramp down. Second, the group delay will be considerably more than with the current O-mode system. This will probably necessitate reducing the modulation frequency by as much as a factor of four. Third, there is the issue of what the highest useable frequency is. As shown in Fig. 4-6, even a small electron density behind the limiter can cause significant separation between the upper cutoff and the upper hybrid resonance. This prevents access to the left hand cutoff at 5.3 tesla for frequencies above 90 GHz[c]. Lastly, it should be pointed out that unlike the right hand wave, the left hand wave is more sensitive to hollow profiles than the O-mode. This

[c]Note that toroidal field ripple is significant at the horn location dropping the B-field by 10 percent over a $1/R$ dependance.

can be seen by looking at figure 4-5. (Moving from right to left, the LHC X-mode curves slope up while the RHC X-mode curves slope down.) The location of the cutoff layer is the intersection of the plasma density profile with the curves shown. So while rotating the polarization will improve the dynamic range of the reflectometer, given the flat to hollow profiles it will not change the reflectometer into a core density diagnostic.

8.2.5 More Sophisticated Modulation Techniques

There are many modulation techniques that one can envision. Several groups (????) have been developing pulsed reflectometry techniques. With the millimeter wave hardware in hand at present, such techniques should be simple to implement. Another option that may prove useful is putting multiple modulation signals in the upconvertor as shown in Fig. 8-2. By using two or more upconversion frequencies, multiple group delay measurements can be derived from one set of millimeter wave components. This could be especially useful for an LHC X-mode diagnostic where the separation in critical density between oscillator frequencies is greater than in O-mode. The upconversion frequencies shown are arbitrarily chosen, and again for LHC X-mode the 1 GHz IF should probably be reduced to 250 MHz. The input power to the upconvertor is limited and the upconversion efficiency drops as the power is reduced, so the number of upconversion frequencies will be limited. Multiple data points could be achieved via a swept or multiplexed upconversion signal.

8.2.6 Fluctuation Diagnostics

So far the reflectometer has been used primarily as a density profile diagnostic and studies of fluctuations have been limited to very qualitative ones. For comparisons with reflectometers elsewhere and to measure Doppler shifts due to plasma rotation, a single sideband of a reflectometer channel should be studied independently. Figure 8-3 shows the modifications needed to the current reflectometer to observe one sideband. The rotation of perturbations in the density near the critical layer will Doppler shift

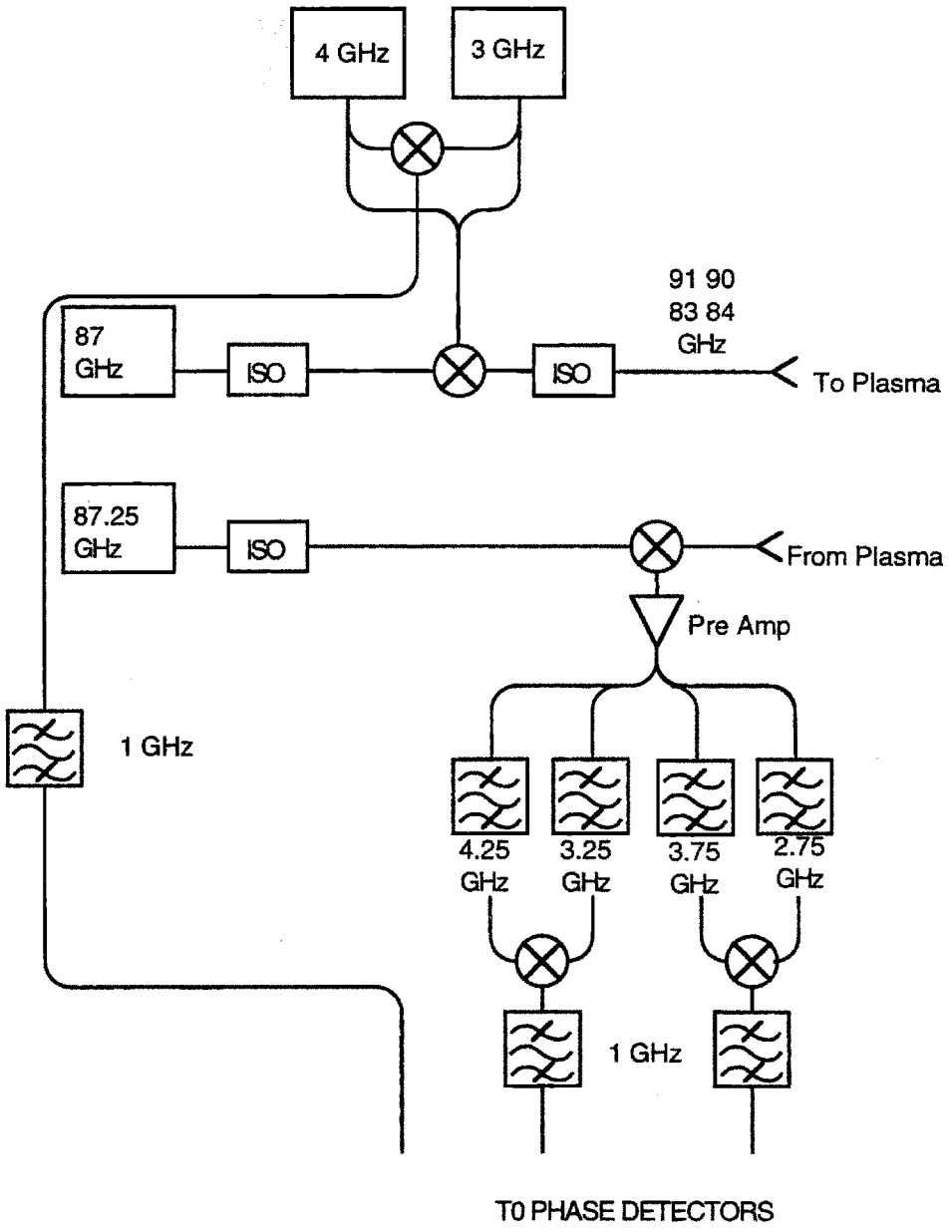

Figure 8-2: Multiple Upconversion Frequency Concept. By using multiple upconversion frequencies, several group delay measurements chan be performed with a single millimeter wave transmitter and receiver.

the returned signal. This will give a crude measure of the plasma rotation velocity. In no way should such a measurement alleviate the need for spectroscopic rotation measurements during H and PEP mode studies. However, the time response for the reflectometer for such measurements can be on the order of tens of microseconds, so such a rotation measurement may provide some insight into the sequence of events during L to H transitions for example. Placing a receiving horn well off the midplane will improve the sensitivity to rotation. PEP mode studies at 7.9 tesla using X-mode polarization should prove particularly interesting as the 110 GHz channel will be able to reach the region where the internal confinement barrier is expected to be.

A key interest of turbulence modelers is the correlation length of the fluctuations that drive turbulence. The multiple upconversion concept sketched in Fig. 8-2 lends itself well to measuring this. By correlating the sidebands from multiple modulation frequencies, the correlation length can be mapped out provided the density gradient is also measured. All of these investigations will require developing an improved raytracing code or application of a two or three dimension full wave code such as the one developed by Irby [79]. Lenses to focus the launched and returned beam may also be needed to improve **k** resolution. The effect of modifying the launching antennas should be investigated using the codes described above.

8.3 More Ambitious Upgrades

8.3.1 ICRF Loading Studies

Another potential application of reflectometry on C-Mod would be the study of the plasma directly in front of the ICRF antennas. In O-mode, frequencies of interest would be 10 to 30 GHz. These frequencies can be transmitted via coaxial cable, so a complicated waveguide run could be avoided and access could be provided via a vertical port. There is enough room to fit a microstrip patch antenna on the wall between the two pairs of two strap antennas. Here reflections from the edges of the ICRF antennas is probably inevitable, however, by eliminating the nonlinear gain

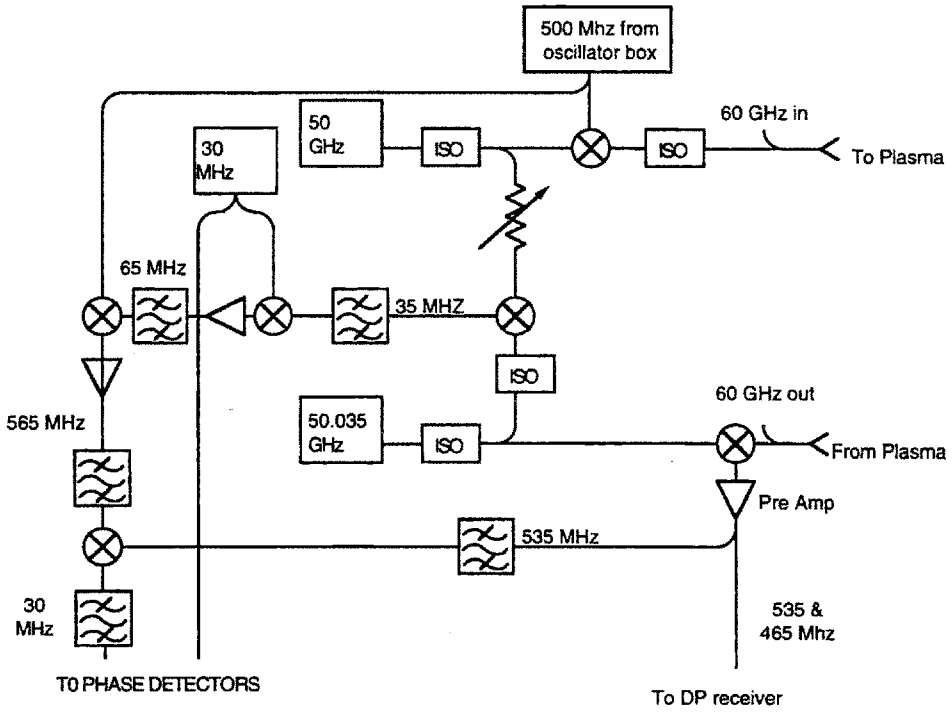

Figure 8-3: Suggested Modifications for Single Sideband Study. This approach eliminates the need to phase lock the launching and receiving sources by referencing the received signal to the 30 MHz oscillator [80]. The 65 MHz filter needs to be sufficiently narrow to eliminate 60 and 70 MHz generated in the mixer. This filter also sets a limit to the bandwidth of the 35 MHz IF between the two Gunn oscillators. Changing the modulation frequency from 500 MHz to something lower would allow for increased bandwidth for the Gunn IF.

amplifiers in the DP receiver, these extra reflections can be zeroed out at the phase detector.

8.3.2 Eliminating Limiter Effects

While the limiter has proven useful for calibration, it greatly modifies the SOL. To eliminate this problem making the reflectometer measurements more useful for divertor modelers, the horns could be positioned off of the midplane either below or above the limiter. This will eliminate the symmetry provided by midplane launch and will necessitate a flux mapping provided by EFIT to interpret the data. On the other hand, moving the launching horns to an off axis location will improve the profile reconstruction accuracy with respect to flux surfaces, as there is considerable flux expansion as one moves away from the midplane.

Moving the limiter is also a possibility. Plans for the tangentially viewing interferometer call for at least part of the limiter to be removed. Moving the horns to another port is extremely unlikely due to the limited diagnostic space available.

8.3.3 Higher Frequencies

A severe limitation to the current diagnostic is operating frequency. The frequencies available limit measurements to $1.5 \times 10^{20}\mathrm{m}^{-3}$ while current high recycling H-Modes now have densities as high as $3.5 \times 10^{20}\mathrm{m}^{-3}$ within a few centimeters of the LCFS.

At 5.3 Tesla, cyclotron absorption greatly limits operation from 115 to 125 GHz. The next window, from 125 to 220 GHz would allow the study of densities from 1.9×10^{20} to 6×10^{20} m^{-3}. Millimeter wave equipment becomes quite expensive over 110 GHz, but the work demonstrated in this thesis and elsewhere [48] provided sufficient confidence that either an O-mode system for frequencies above 125 GHz or an X-mode system from 170 to 230 GHz will work. Such a project may be well suited for collaborations perhaps performed under an SBIR.

The other option is to arrange for high field launch to the LHC. The millimeter wave equipment for such a reflectometer is already available in the current O-mode

system. The thin inner wall protection tiles ($\sim$ 1.5 cm thick) make the threading of transmitting and receiving lines to the midplane on the inner wall a daunting task, not to mention developing antennas.

8.4 Future H-Mode Work

It is not altogether clear what the long range goals for C-Mod should be with respect to H-mode development. C-Mod has already contributed greatly to the scaling of L to H transitions. With the boronization of the vacuum chamber, H factors in excess of 2.5 have been achieved which is comparable to the values achieved elsewhere in ELM-free H-Mode. To continue improving the H-factor, VH-modes will probably be needed. To get VH-modes some method of off axis current drive will be needed. The planned four strap ICRF antenna will provide this capability.

Controlling the density rise during ELM-free H-modes is another issue. Divertor pumping may help in achieving lower density EF H-modes. Currently a prototype divertor cryopump is in place and ready for testing during the spring 1997 run campaign.

From the point of view of understanding H-mode physics, several diagnostics are needed. Currently, the plasma current profile and the edge toroidal and poloidal rotation are not measured. The diagnostic neutral beam should help in determining all of these quantities. In addition, the views for the current UV spectrograph [81] are being modified to look for doppler shifts due to plasma rotation. If these efforts prove successful, Doyle [62, 82] has demonstrated that with good poloidal rotation measurements and high shear in the rotation velocity, quite good spatial resolution can be inferred from collective scattering diagnostics. Stated another way, without good knowledge of the plasma rotation velocity all frequency measurements have an error bar corresponding to $\mathbf{k} \cdot v_\theta$ which can be far in excess of the natural frequency spread in the fluctuations, making the measurement quantitatively useless.

Appendix A

DP Measurement of a Linear Profile

For a linear profile as shown above we can get a simple expression for the phase measured with a differential phase reflectometer.

$$n(r) = \begin{cases} \beta r & \text{for } r \geq 0, \\ 0 & \text{for } r < 0. \end{cases} \qquad n_c(F) = \frac{F^2}{\alpha}$$

For $r \geq 0$ the index of refraction, N, is given by:

$$N(F,r) = \left(1 - \frac{n(r)}{n_c(F)}\right)^{\frac{1}{2}} = \left(1 - \frac{\beta\alpha}{F^2} r\right)^{\frac{1}{2}} \tag{A.1}$$

In the WKB limit we get the following with the $-\pi/2$ correction at reflection:

$$\begin{aligned} \phi(F) &= 2\int_0^{r_c(F)} \frac{2\pi N(F,r)}{\lambda} dx - \frac{\pi}{2} + 2\frac{2\pi}{\lambda} y \\ &= \frac{4\pi F}{c}\left[y + \int_0^{r_c} \left(1 - \frac{\beta\alpha}{F^2} r\right)^{\frac{1}{2}} dr\right] - \frac{\pi}{2} \end{aligned} \tag{A.2}$$

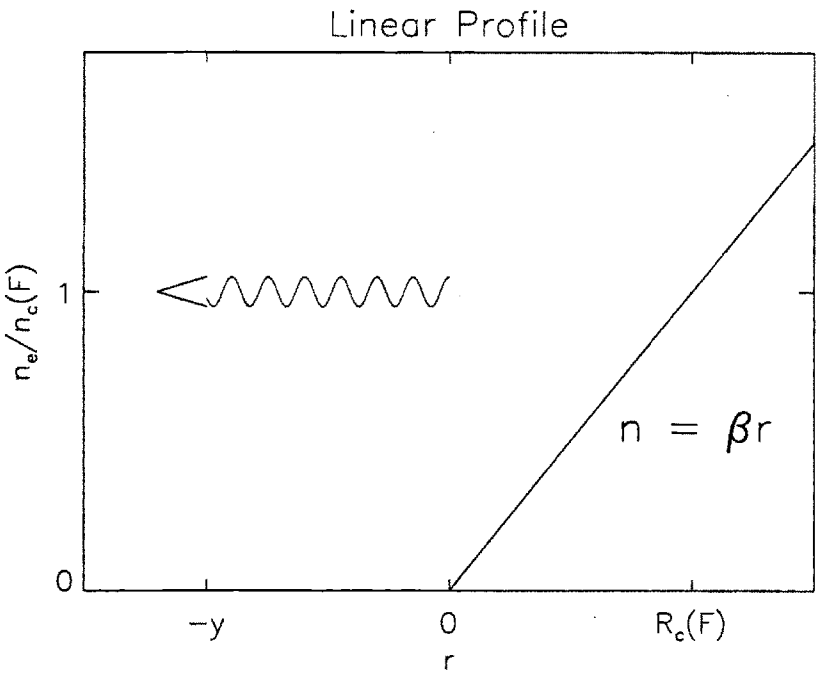

Figure A-1: Linear Profile

Now substitute: $u \equiv 1 - \frac{\beta\alpha}{F^2} r$ and integrate:

$$\phi = \frac{4\pi F}{c}\left[y - \frac{F^2}{\beta\alpha}\int_1^0 u^{\frac{1}{2}}\,du\right] - \frac{\pi}{2} = \frac{4\pi F}{c}\left[y + \frac{2F^2}{3\beta\alpha}\right] - \frac{\pi}{2} \tag{A.3}$$

Now let's look at a two frequency system.

$$F_1 = F_0 + \frac{\Delta F}{2}, \qquad F_2 = F_0 - \frac{\Delta F}{2} \tag{A.4}$$

$$\begin{aligned}
\Delta\phi\,(F,\Delta F) &= \phi\left(F + \frac{\Delta F}{2}\right) - \phi\left(F - \frac{\Delta F}{2}\right) \\
&= \frac{4\pi(F_0 + \frac{\Delta F}{2})}{c}\left[y + \frac{2(F_0 + \frac{\Delta F}{2})^2}{3\beta\alpha}\right] - \frac{4\pi(F_0 - \frac{\Delta F}{2})}{c}\left[y + \frac{2(F_0 - \frac{\Delta F}{2})^2}{3\beta\alpha}\right] \\
&= \frac{4\pi}{c}\Delta F y + \frac{4\pi}{c} 2\frac{\left[(F_0 + \frac{\Delta F}{2})^3 - (F_0 - \frac{\Delta F}{2})^3\right]}{3\beta\alpha}
\end{aligned} \tag{A.5}$$

Now make the approximation $F_0 \gg \Delta F$:

$$\left(F_0 + \frac{\Delta F}{2}\right)^3 - \left(F_0 - \frac{\Delta F}{2}\right)^3 = 3\Delta F {F_0}^2 - \frac{\Delta F^3}{4} \approx 3\Delta F {F_0}^2 \tag{A.6}$$

Substituting in gives the rather simple result:

$$\begin{aligned} \Delta\phi(F_0, \Delta F) &= \frac{4\pi}{c}\Delta F\left[y + 2R_c(F)\right] \\ &= \frac{4\pi}{c}\Delta F\left[y + 2\frac{F^2}{\alpha\beta}\right] \end{aligned} \tag{A.7}$$

A couple of interesting features of this result are: first, the phase measurement is proportional to the modulation frequency. One can unfortunately gain no more information about a linear density profile by changing the modulation frequency. In addition, since the largest contributions to the group delay for most expected profiles are the location of the reflecting layer and the slope in the region near that reflecting layer, under most conditions no great improvement in profile reconstruction can be expected by using multiple modulation frequencies.

Second, the ultimate resolution of a reflectometer will be the absolute error in the phase measurement. The amplitude to phase modulation specifications can be relaxed by increasing the modulation frequency. For example, the phase error over the dynamic range of the limiting amps used in the C-Mod reflectometer is ± 2.5 deg. In order to obtain ± 2 mm resolution one needs a modulation frequency of 1 Ghz.

Third, this simple result points to a second approach to profile inversion. By assuming the profile is piecewise linear and monotonic one can construct a matrix equation relating R as a function of n. This approach has the added advantage of providing a method of including errors, point measurements, and constraints in the inversion. Figure A-3 shows how a profile might be linearized. The following tour de force of LaTex will show what should be obvious, that the group delay measured by each reflectometer channel can be put into a form $\Phi_i = \sum \alpha_{ji} x_j$.

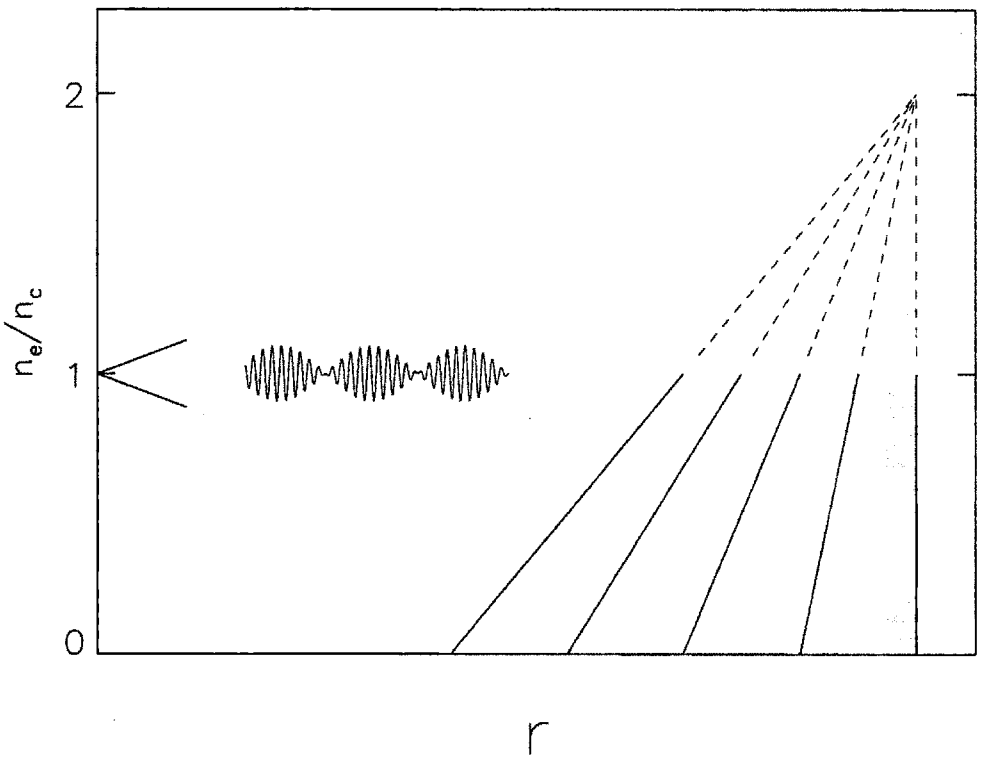

Figure A-2: Indistinguishable Profiles To a single frequency DP reflectometer, all of the profiles shown above give the same returned signal.

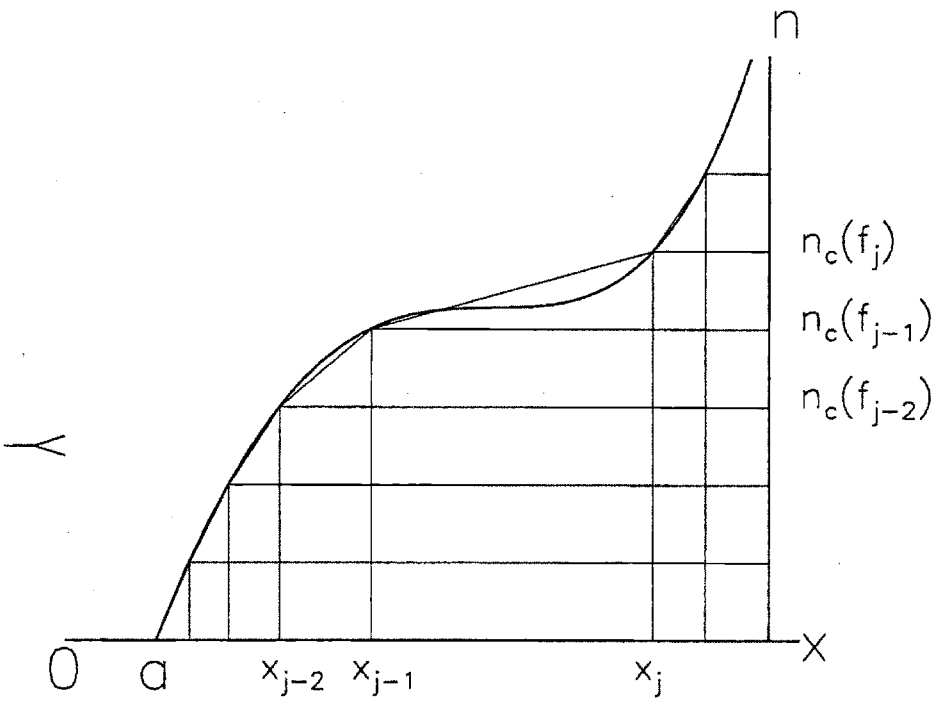

Figure A-3: Linearized Profile

$$\Phi_i = \Delta\phi(f_i, \Delta f) \tag{A.8}$$

$$= \frac{4\pi}{\lambda_{i+}} \int_0^{R_c(f+\frac{\Delta f}{2})} \left(1 - \frac{n(x)}{n_{i+}}\right)^{\frac{1}{2}} dx - \frac{4\pi}{\lambda_{i-}} \int_0^{R_c(f-\frac{\Delta f}{2})} \left(1 - \frac{n(x)}{n_{i-}}\right)^{\frac{1}{2}} dx \tag{A.9}$$

$$= \sum_j \phi_{ji} \tag{A.10}$$

where ϕ_{ji} is the contribution to the phase of the beat wave from each linear section and,

$$\lambda_{i\pm} = \frac{c}{\left(f_i \pm \frac{\Delta f}{2}\right)}. \tag{A.11}$$

Writing ϕ_{ji} explicitly gives:

$$\phi_{ji} = \begin{cases} \frac{4\pi}{\lambda_{i+}} \int_{x_j}^{x_{j+1}} N_{i+}(x)dx - \frac{4\pi}{\lambda_{i-}} \int_{x_j}^{x_{j+1}} N_{i-}(x)dx & \text{if } n_{x+1} \leq n_{c_{i+}} \\ \frac{4\pi}{\lambda_{i+}} \int_{x_j}^{x_{j+1}} N_{i+}(x)dx - \frac{4\pi}{\lambda_{i-}} \int_{x_j}^{R_{c_i-}} N_{i-}(x)dx & \text{if } n_j < n_{c_{i-}} < n_{j+1} < n_{c_{i+}} \\ \frac{4\pi}{\lambda_{i+}} \int_{x_j}^{R_{c_i+}} N_{i+}(x)dx - \frac{4\pi}{\lambda_{i-}} \int_{x_j}^{R_{c_i-}} N_{i-}(x)dx & \text{if } n_j < n_{c_{i-}} < n_{c_{i+}} \leq n_{j+1} \\ \frac{4\pi}{\lambda_{i+}} \int_{x_j}^{R_{c_i+}} N_{i+}(x)dx & \text{if } n_{c_{i-}} < n_j < n_{c_{i+}} < n_{j+1} \\ 0 & \text{if } n_{c_{i+}} \leq n_j \end{cases} \tag{A.12}$$

where,

$$n_{c_{i\pm}} \equiv n_c\left(f_i \pm \frac{\Delta f}{2}\right) \qquad \text{and} \qquad R_{ci\pm} \equiv R_c\left(f_{i\pm}\frac{\Delta f}{2}\right)$$

$$N_{i\pm}(x) = \left(1 - \frac{n(x)}{n_{i\pm}}\right)^{\frac{1}{2}} \qquad \text{and} \qquad N_{i\pm}(n) = \left(1 - \frac{n}{n_{i\pm}}\right)^{\frac{1}{2}}$$

Now change the variables of integration,

$$\frac{dN_{i\pm}}{dn} = -\frac{1}{2n_{i\pm}}\frac{1}{N_{i\pm}} \qquad \text{and} \qquad \frac{dn}{dx} = \frac{n_{j+1} - n_j}{x_{j+1} - x_j}$$

and integrate

$$\int_a^b N_{i\pm}dx = \int_{N_{i\pm}(a)}^{N_{i\pm}(b)} N_{i\pm}\left[\frac{dN_{i\pm}}{dn}\frac{dn}{dx}\right]^{-1} dN_{i\pm} \tag{A.13}$$

$$= -2n_{i\pm}\frac{x_{j+1} - x_j}{n_{j+1} - n_j}\int_{N_{i\pm}(a)}^{N_{i\pm}(b)} N_{i\pm}^2 dN_{i\pm} \tag{A.14}$$

$$= -\frac{2n_{i\pm}}{3}\frac{x_{j+1} - x_j}{n_{j+1} - n_j}\left[N_{i\pm}^3(b) - N_{i\pm}^3(a)\right], \tag{A.15}$$

finally giving

$$\phi_{ji} = (x_{j+1} - x_j)\,\beta_{ji} \tag{A.16}$$

where:

$$\frac{\beta_{ji}}{K_{ji\pm}} = \begin{cases} N^3_{i+}(n_j) - N^3_{i+}(n_{j+1}) - N^3_{i-}(n_j) + N^3_{i-}(n_{j+1}) & \text{if } n_{x+1} \le n_{c_{i+}} \\ N^3_{i+}(n_j) - N^3_{i+}(n_{j+1}) - N^3_{i-}(n_j) + 0 & \text{if } n_j < n_{c_{i-}} < n_{j+1} < n_{c_{i+}} \\ N^3_{i+}(n_j) - 0 - N^3_{i-}(n_j) + 0 & \text{if } n_j < n_{c_{i-}} < n_{c_{i+}} \le n_{j+1} \\ N^3_{i+}(n_j) - 0 - 0 + 0 & \text{if } n_{c_{i-}} < n_j < n_{c_{i+}} < n_{j+1} \\ 0 & \text{if } n_{c_{i+}} \le n_j \end{cases}$$

$$K_{ji\pm} \equiv \frac{2n_{c_{i\pm}}}{3(n_{j+1} - n_j)}$$

$$\Phi_i = -x_0\beta_{0i} + \sum_j \left(-\beta_{ji} + \beta_{(j-1)i}\right) x_j \tag{A.17}$$

$$= \sum_{j=0}^{m} \alpha_{ji} x_j \tag{A.18}$$

$$\text{where,} \qquad \alpha_{ji} = \begin{cases} -\beta_{0i} & \text{for} \quad i = 0 \\ \beta_{(j-1)i} - \beta_{ji} & \text{for} \quad i > 0 \end{cases} \tag{A.19}$$

A point density measurement or constraint, n, at x can be included with:

$$(n - n_j)x_{j+1} + (n_{j+1} - n)x_j = (n_{j+1} - n_j)x. \tag{A.20}$$

Multiple constraints can be represented by a matrix equation:

$$\mathbf{C} \cdot X = Q \tag{A.21}$$

A smoothing constraint can be included with:

$$\mathbf{S} \cdot X = 0. \tag{A.22}$$

$$\text{where } \mathbf{S} = \begin{bmatrix} 1 & -1 & 0 & \cdot & \cdot & \cdot & & 0 \\ -1 & 2 & -1 & & & & & \\ 0 & -1 & 2 & & & & & \cdot \\ & & & \cdot & & & & \cdot \\ \cdot & & & & \cdot & & & \cdot \\ \cdot & & & & & \cdot & & \\ \cdot & & & & & 2 & -1 & 0 \\ & & & & & -1 & 2 & -1 \\ 0 & & \cdot & \cdot & \cdot & 0 & -1 & 1 \end{bmatrix} \tag{A.23}$$

The diagonal weighting matrix, $\mathbf{W}$, includes the weights each equation and corrects for differences in units in the individual equations. The whole system reduces to:

$$\mathbf{W} \cdot \begin{bmatrix} A \\ C \\ S \end{bmatrix} \cdot X = W \cdot \begin{bmatrix} \Phi \\ Q \\ O \end{bmatrix} \tag{A.24}$$

Using singular value decomposition [83], this equation can be inverted to get the matrix $\mathbf{X}$.

Appendix B

List of Acronyms

Acronym	Meaning	First Usage
D-Alpha Emission	Emission from the α line of Deuterium	page 34
DP	Differential Phase	page 76
ECE	Electron Cyclotron Emission	page 48
EDA	Enhanced D_α	page 139
EF	Equilibrium Field (Coils)	page 41
ELM	Edge Localized Mode	page 34
FSR	Fluctuation Suppression Region	page 130
GPC	Grating Polychromator	page 49
H-Mode	High Confinement Mode	page 33
ICRF/ ICRH	Ion Cyclotron Resonance Frequency/Heating	page 50

Table B.1: List of Acronyms

Acronym	Meaning	First Usage
ITER	International Tokamak Experimental Reactor	page 23
L-Mode	Low Confinement Mode	page 32
L-H Transition	Low to High Mode Transition	page 33
LCFS	Last Closed Flux Surface	page 31
LHC	Left hand Cutoff	page 57
O-Mode	Ordinary ($\mathbf{E} \parallel \mathbf{B}$) Mode E&M Wave	page 57
PEP	Pellet Enhanced Performance	page 32
PETS	Princeton Edge Thomson Scattering	page 43
PF	Poloidal Field (Coils)	page 41
PFR	Private Flux Region	page 31
RHC	Right Hand Cutoff	page 57
SGR	Steep Gradient Region (Transport Barrier Region)	page 34
SOL	Scrape Off Layer	page 31
TCI	Two Color Interferometer	page 42
TF	Toroidal Field (coils)	page 40
TS	Thomson Scattering	page 44
VH-mode	Very High (confinement) Mode	page 35
X-Mode	Extraordinary ($\mathbf{E} \perp \mathbf{B}$) Mode EM Wave	page 57
Z	Atomic Number	page 29

Bibliography

[1] S.M. Kaye and R Goldston. *Nuclear Fusion*, 25:65, 1985.

[2] R. D. Stambaugh et al. Enhanced confinement in tokamaks. *Phys. Fluids B*, 2(12):2941, December 1990.

[3] F. Wagner et al. Regime of improved confinement and high beta in neutral-beam-heated divertor discharges of the ASDEX tokamak. *Phys. Rev. Lett.*, 49:1408, 1982.

[4] Francis F. Chen. *Introduction to Plasma Physics and Controlled Fusion*, volume 1. Plenum Press, 2 edition, 1984.

[5] John Wesson. *Tokamaks.* Oxford University Press, 1987.

[6] Martin Schwarzschild. *Structure and Evolution of the Stars.* Dover Publications, Inc., 1958.

[7] J.D. Lawson. Some criteria for a power producing thermonuclear reactor. *Proceedings of the Physical Society B*, 70(6), 1957.

[8] I.H.Hutchinson. Personal Communication, 1996.

[9] Darren Thomas Garnier. *Lithium Pellet Injection Experiments on the Alcator C-Mod Tokamak.* Ph.D. thesis, Massachusetts Institute of Technology, June 1996.

[10] P.N. Yushmanov. Scalings for tokamak energy confinement. *Nucl. Fusion*, 30(10):1999, 1990.

[11] R. J. Groebner. An emerging understanding of H-mode discharges in tokamaks. *Phys. Fluids B*, 5(7):2343–2354, July 1993.

[12] S. M. Kaye (Chairman). Papers from the 5th IAEA technical committee meeting/ US-Japan workshop on H-mode physics. *Plasma Phys. and Control. Fusion*, 38(8):1089–1501, August 1996.

[13] D. J. Ward. LH transition theories and theory of H-mode. *Plasma Phys. Control. Fusion*, 38:1201–1212, 1996.

[14] Ian H. Hutchinson and Miklos Porkolab. Alcator C-Mod fusion research program 1996-2000. Technical report, MIT Plasma Fusion Center, 175 Albany Street, Cambridge, MA 02139, June 1995.

[15] E. S. Marmar. The Alcator C-Mod diagnostic complement. *Rev. Sci.Instrum*, 63:4695, October 1992.

[16] James Reardon et al. Spatial structure of pump wave and parametric decay instability during ICRF injection on Alcator C-Mod. *Bulletin of the American Physical Society*, October 1996.

[17] D. Dimock, B. Grek, D. Johnson, B. LaBombard, B. Lipschultz, and G. McCracken. A compact thomson scattering system. *Rev. Sci. Instrum*, Jan 1997.

[18] J. H. Irby et al. Prototype tangential interferometer for Alcator C-Mod. In *Bulletin of the American Physical Society*, volume 41, page 1551, October 1996.

[19] T. Luke. *Measurement of Particle Transport Coefficients on Alcator C-Mod.* Ph.D. thesis, Massachusetts Institute of Technology, October 1994.

[20] B. Labombard. Scaling and transport analysis of divertor conditions on the Alcator C-Mod tokamak. *Phys. Plasmas 2*, pages 2242–2248, 1995.

[21] L. L. Lao et al. Reconstruction of current profile parameters and plasma shapes in tokamaks. *Nuclear Fusion*, 25, 1985.

[22] R.S. Granetz, I.H. Hutchinson, J. Gerolamo, W. Pina, and C. Tsui. Magnetic diagnostics in Alcator C-Mod. *Rev. Sci. Instrum.*, 61:2967, 1990.

[23] T.S. Hsu. *The Submillimeter Wave Electron Cyclotron Emission Diagnostic for the Alcator C-Mod Tokamak.* Ph.D. thesis, Massachusetts Institute of Technology, 1993.

[24] Amanda Eileen Hubbard. *Measurement of Electron Density on JET by Microwave Reflectometry.* Ph.D. thesis, Imperial Collage of Science and Technology, May 1987.

[25] J.L. Terry et al. The visible, imaging diode arrays on Alcator C-Mod. *Rev. Sci. Instrum.*, 66(1), January 1995.

[26] C. Kurz. Ph.D. thesis, Massachusetts Institute of Technology, 1995.

[27] R. Parker et al. *Nucl. Fus.*, 25:1985, 1985.

[28] M. Greenwald et al. *Phys. Plasmas*, 6(2):2308, 1995.

[29] J. Goetz et al. Comparison of detached and radiative divertor operation in Alcator C-Mod. *Phys. Plasmas*, 3(5):1908–15, May 1996.

[30] M. Greenwald et al. H-mode confinement in Alcator C-Mod. Technical Report PFC/JA-96-29, MIT Plasma Fusion Center, 175 Albany Street, Cambridge, MA 02139, September 1996.

[31] M. Greenwald et al. H-mode confinement in Alcator C-Mod. *Submitted to Nuclear Fusion*, 1996.

[32] *IAEA Technical Committee Meeting on Reflectometry for Fusion Plasma Diagnostics, Abington (United Kingdom).* March 1992.

[33] N.L. Bretz. *Microwave reflectometry for fusion plasma diagnostics. Report on the IAEA Technical Committee Meeting held at Princeton Plasma Physics Laboratory, Princeton University, Princeton, New Jersey, United States.* January 1994.

[34] Nicholas A. Krall and Alvin W. Trivelpiece. *Principles of Plasma Physics.* San Francisco Press, Inc., 1986.

[35] V. L. Ginzburg. *Propagation of Electromagnetic Waves in Plasma.* Gordon and Breach, Science publishers, Inc., 1961.

[36] K. G. Budden. *The Propagation of Radio Waves.* Cambridge University Press, 1985.

[37] Robert H. Dicke and James P. Wittke. *Introduction to Quantum Mechanics.* Addison-Wesley Publishing Company, 1960.

[38] Ian H. Hutchinson. *Principles of Plasma Diagnostics.* Cambridge University Press, 1987.

[39] R. Gandy et al. Observation and analysis of maser activity in a tokamak plasma. *Physical Review Letters*, 54(8):800–803, February 1985.

[40] G. Hanson. Personal Communication, 1994.

[41] R. Grandy. Personal Communication, 1996.

[42] H.Bindslev. Relativistic effects in plasma reflectometry. *Plasma Physics and Controlled Fusion*, 34, 1992.

[43] Thomas Martin Lehecka. *Millimeter-Wave Reflectometry Diagnostics on the DIII-D Tokamak.* Ph.D. thesis, University of California at Los Angeles, September 1989.

[44] A.C.C. Sips. *Reflectometry and Transport in Thermonuclear Plasmas in the Joint European Torus.* Ph.D. thesis, Technische Universiteit Eindhoven, March 1991.

[45] Coenraad Albertus Jacobus Hugenholtz. *Microwave Interferometer and Reflectometer Techniques for Thermonuclear Plasmas.* Ph.D. thesis, Technische Universiteit Eindhoven, 1990.

[46] F. Simionet. *Etude de la reflectometrie hyperfrequence en modes ordinaire et extraordinare pour la mesure du profil radial et des fluctuations locales de la densite electronique dans les tokamaks.* Ph.D. thesis, Universite de Nancy, 1985.

[47] Hervé Bottollier-Curtet. *Réflectométrie hyperfréquence pour la détermination de la densité électronique et de ses fluctuations sur le tokamak Petula-B.* Ph.D. thesis, L'Université de Paris XI, 1986.

[48] C. Laviron et al. Reflectometry techniques for density profile measurements on fusion plasmas. *Plasma Physics and Controlled Fusion*, 38, 1996.

[49] Greg Hanson et al. *Bull. Am. Phys. Soc.*, 39:1560, 1994.

[50] P. Buratti et al. *Rev. Sci. Instrum*, 66:409, 1995.

[51] E. de la Luna et al. *Rev. Sci Instrum*, 66:403, 1995.

[52] V. A. Vershkov et al. *Controlled Fusion and Plasma Physics, Proc. 21st Eur. Conf.*, 18B:1192, 1994.

[53] D. Pinsonneault et al. Edge density profile measurements on TdeV using an AM reflectometer. *Bulletin of the American Physical Society*, 40(11):1712, October 1995.

[54] Paul C. Stek et al. Theoretical and experimental development of a reflectometry experiment for Alcator C-Mod. *Bulletin of the American Physical Society*, 35(9):1997, October 1990.

[55] R. Prentice. Personal Communication, 1989.

[56] John P. Quine. E- and H-plane bends for high-power oversized rectangular waveguides. *IEEE Transactions on Microwave Theory and Techniques*, pages 54–63, January 1965.

[57] David Humphreys and Robert Granetz. Private communication.

[58] Bruce Lipshultz and B. Labombard. Electromagnetic forces on internal hardware in case of in-place disruption. Internal Memorandum, 1988.

[59] R. S. Granetz, I. H. Hutchinson, J.Sorci, J. H. Irby, B. Labombard, and D. Gwinn. *Nuclear Fusion*, 36, May 1996.

[60] G. Mannduchi G. Flor, T.W. Fredian, J.A. Stillerman, and K.A. Klare. MDSPlus:a comprehensive data acquisition and analysis system. In *Proceedings of the 16th Symposium on Fusion Technology*, pages 1272–1276, September 1990.

[61] Thomas Lehecka. Personal Communication, 1989.

[62] Edward Doyle et al. Physics of turbulence control and transport barrier formation in DIII-D. In *16th IAEA Fusion Energy Conference (Montreal)*, number F1-CN-64/AP2-11, October 1996.

[63] P.C. Stangeby and G.C. McCracken. Plasma boundary phenomena in tokamaks. *Nucl. Fus.*, 30(7):1225, 1990.

[64] P.C. Stangeby. The interpretation of plasma probes for fusion experiments. In Orlando Auciello and Daniel L. Flamm, editors, *Plasma Diagnostics*, volume 2. Academic Press, 1989.

[65] B. Labombard. Personal Communication, 1997.

[66] G F Matthews et al. *J. Nucl. Mater.*, 1986.

[67] A.E. Hubbard et al. Local plasma parameters and H-mode threshold in Alcator C-Mod. In *16th IAEA Fusion Energy Conference (Montreal)*, number F1-CN-64/AP2-11, October 1996.

[68] A. Hubbard. Personal Communication, 1997.

[69] S. Wolfe. Effect of edge current on flux reconstruction in Alcator C-Mod. In *Bulletin of the American Physical Society*, volume 41, page 1482, October 1996.

[70] Yuichi Takase. Personal Communication, 1997.

[71] John Rice. Personal Communication, 1997.

[72] D. Veron. *Opt. Comm.*, 10:95, 1974.

[73] E. Mazzucato and R. Nazikian. Radial scale length of turbulent fluctuations in the main core of TFTR plasmas. *Phys. Rev. Lett.*, 71(12):1840–1843, September 1993.

[74] E. S. Marmar et al. Boronization on Alcator C-Mod. In *Bulletin of the American Physical Society*, volume 41, page 1551, October 1996.

[75] C. Reddy et al. The Alcator C-Mod boronization system. In *Bulletin of the American Physical Society*, volume 41, page 1551, October 1996.

[76] J.E. Rice et al. Impurity transport in Alcator C-Mod plasmas. *Physics of Plasmas*, to be published, June 1997.

[77] I.H.Hutchinson et al. Fast edge mode observed during enhanced D_α phase in Alcator C-Mod. In *Bulletin of the European Physical Society*, 1997.

[78] I.H.Hutchinson. Personal Communication, 1997.

[79] J. H. Irby et al. 2D full wave simulation of ordinary mode reflectometry. *Plasma Physics and Controlled Fusion*, 25(5), May 1993.

[80] J.L. Doane. Broadband superheterodyne tracking circuits for millimeterwave measurements. *Review of Scientific Instruments*, 51(3):317, Mar 1980.

[81] B. L. Welch et al. High-resolution visible/ultraviolet measurements from the Alcator C-Mod tokamak. *Bull. Am. Phys. Soc.*, 41, November 1996.

[82] Edward Doyle et al. *Bull. Am. Phys. Soc.*, 1995.

[83] William H. Press et al. *Numerical Recipes in C.* Cambridge University Press, 1988.